ULTRA-LOW-NOISE FREQUENCY SYNTHESIS, COMPARISON AND DISSEMINATION USING FEMTOSECOND OPTICAL FREQUENCY COMBS

Maurice Lessing

A Thesis Submitted for the Degree of DEng
at the
University of St Andrews

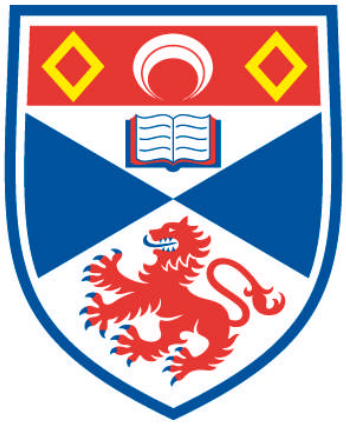

2016

ULTRA-LOW-NOISE FREQUENCY SYNTHESIS, COMPARISON AND DISSEMINATION USING FEMTOSECOND OPTICAL FREQUENCY COMBS

Maurice Lessing

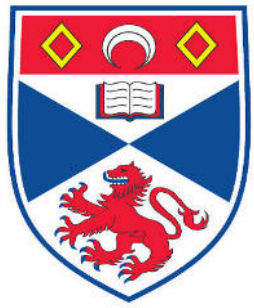

This thesis is submitted in partial fulfilment for the degree of
Doctor of Engineering
at the
University of St Andrews

October 2015

Abstract

This thesis presents research into ultra-low noise photonic microwave synthesis and the development of a novel, frequency comb-based, fibre optic time transfer technique.

The focus in the first area is on reducing the noise introduced in the optical-to-electrical conversion process using balanced optical-microwave phase detectors. Two mainly free-space and two mainly fibre-based devices were built and their performance was characterised. The phase noise of the optical-to-electrical conversion of the free-space device was $-119\,\mathrm{dBc\,Hz^{-1}}$ at 1 Hz and $-143\,\mathrm{dBc\,Hz^{-1}}$ at 20 kHz from an 8 GHz carrier which is the best performance reported for a free-space balanced-optical microwave phase detector. The improved fibre-based set-ups demonstrated a state-of-the-art amplitude-to-phase noise suppression of 60 dB and a phase noise of the optical-to-electrical conversion of $-131\,\mathrm{dBc\,Hz^{-1}}$ at 1 Hz and -148 Hz at 20 kHz from an 8 GHz carrier.

The novel time transfer technique developed in the second part superimposes timing information onto the optical pulse train of an ITU-channel-filtered frequency comb using an intensity modulation scheme. Time transfer over a 50 km long, delay-stabilised fibre spool produced a state-of-the-art time deviation of 300 fs and an accuracy of approximately 0.01 ns which is close to the best performance achieved using amplitude modulated cw lasers. Using this technique on a 159 km long installed fibre link between NPL and Reading, the same time deviation was achieved and an accuracy of approximately 0.08 ns was obtained, limited by uncertainty of the time interval counter. Using the same fibre link, microwave frequency transfer of the ITU-channel-filtered comb was demonstrated with a fractional frequency instability of 2×10^{-17} at 5000 s which is approximately at the same level as the best previously reported results which were obtained with a 30 nm wide optical frequency comb.

Dedicated to my parents.

Acknowledgements

During my doctorate I received support and guidance from several people. I would like to express my deepest gratitude to my supervisors:

My academic supervisor Dr. Tom Brown, for invaluable guidance, support and encouragement.

My industrial supervisor Dr. Helen Margolis, for being incredibly supportive and for sharing her insights with me.

My day-to-day supervisor Dr. Giuseppe Marra, for sharing his insights and enthusiasm with me and for being incredibly supportive.

Furthermore, I would like to thank:

Dr. Jochen Kronjaeger, for very informative discussions and for help in technical questions.

Dr. Luke Johnson, for sharing his knowledge on combs with me.

Peter Whibberley, for very informative discussions and for lending me a PPS generator.

David Gozzard, for designing the oven chamber which I used in my experiments to temperature stabilise a fibre spool.

Dr. Stephen Webster, for sharing his knowledge on vibration isolation platforms with me.

Dr. Simon Hall and Dr. Matt Cashmore, for lending me a digital storage oscilloscope.

The numerous staff at NPL's Time & Frequency group who made NPL a very nice place to work in.

Finally, I would like to thank my family for their encouragement and support throughout my academic studies.

1. Candidate's declarations:

I, Maurice Lessing hereby certify that this thesis, which is approximately 39 000 words in length, has been written by me, and that it is the record of work carried out by me, or principally by myself in collaboration with others as acknowledged, and that it has not been submitted in any previous application for a higher degree.

I was admitted as a research student in October 2011 and as a candidate for the degree of EngD in October 2011; the higher study for which this is a record was carried out in the University of St Andrews between 2011 and 2015.

Date …… signature of candidate ……

2. Supervisor's declaration:

I hereby certify that the candidate has fulfilled the conditions of the Resolution and Regulations appropriate for the degree of EngD in the University of St Andrews and that the candidate is qualified to submit this thesis in application for that degree.

Date …… signature of supervisor ……

3. Permission for publication: (*to be signed by both candidate and supervisor*)

In submitting this thesis to the University of St Andrews I understand that I am giving permission for it to be made available for use in accordance with the regulations of the University Library for the time being in force, subject to any copyright vested in the work not being affected thereby. I also understand that the title and the abstract will be published, and that a copy of the work may be made and supplied to any bona fide library or research worker, that my thesis will be electronically accessible for personal or research use unless exempt by award of an embargo as requested below, and that the library has the right to migrate my thesis into new electronic forms as required to ensure continued access to the thesis. I have obtained any third-party copyright permissions that may be required in order to allow such access and migration, or have requested the appropriate embargo below.

The following is an agreed request by candidate and supervisor regarding the publication of this thesis:

PRINTED COPY
a) No embargo on print copy

ELECTRONIC COPY
a) No embargo on electronic copy

Date …… signature of candidate …… *signature of supervisor ……*

Please note initial embargos can be requested for a maximum of five years. An embargo on a thesis submitted to the Faculty of Science or Medicine is rarely granted for more than two years in the first instance, without good justification. The Library will not lift an embargo before confirming with the student and supervisor that they do not intend to request a continuation. In the absence of an agreed response from both student and supervisor, the Head of School will be consulted. Please note that the total period of an embargo, including any continuation, is not expected to exceed ten years.
Where part of a thesis is to be embargoed, please specify the part and the reason.

Contents

List of Figures

List of Tables

Nomenclature

$\mathscr{L}(f)$	Single-sideband phase noise at offset frequency f
AlN	Aluminium Nitride
AM-PM	Amplitude-to-phase noise
AOM	Acousto-optic modulator
BOM-PD	Balanced optical-microwave phase detector
CEO	Carrier envelope offset
DBM	Double balanced mixer
DVM	Digital voltmeter
EDFA	Erbium-doped fibre amplifier
EOM	Electro-optic modulator
FBA	Fibre Brillouin amplifiers
FFT	Fast Fourier transform
GPS	Global Positioning System
GSM	Global System for Mobile Communications
HVA	High-voltage amplifier
MBW	Measurement bandwidth

MLL	Mode-locked laser
MUTC	Modified uni-traveling carrier
MZIM	Mach-Zehnder intensity modulator
NPL	National Physical Laboratory
PLL	Phase-locked loop
PMD	Polaristion mode dispersion
PPS	Pulse per second
PSD	Power spectral density
rf	Radio frequency
RIN	Relative intensity noise
SI	International System of Units
SLI	Sagnac-loop interferometer
SNR	Signal-to-noise ratio
SSB	Single-sideband
Ti:sapphire	Titanium-sapphire
TIC	Time interval counter
TWSTFT	Two way satellite time and frequency transfer
ULE	Ultra Low Expansion
UTC	Uni-traveling carrier
VOA	Variable optical attenuator

1 Introduction

The accurate measurement of time and frequency is of key importance to many applications underpinning our technological society. Frequency and time are the physical quantities which can be determined with the highest precision. The science of time-keeping was revolutionised by the development of atomic clocks. Their stability and accuracy is orders of magnitude higher than that of mechanical clocks because of their narrow atomic transitions, their high operating frequency and the fact that they can be better isolated from environmental effects. Since their operating frequency is determined by fundamental physical constants, they also offer a superior reproducibility. Any clock based on the same atomic transition exhibits exactly the same frequency. An atomic frequency standard is turned into a clock by counting the cycles of the clock frequency.

The development of atomic microwave clocks has enabled many technical applications such as satellite navigation systems (Global Positioning System) and telecommunications systems (the Internet and mobile phones). In recent years, optical atomic clocks which are based on optical atomic transitions in ions or neutral atoms have outperformed microwave atomic clocks which are currently used to define the second. This development will lead to performance improvements in technical applications and enable scientific applications such as the test of fundamental physical theories. In the following section some of the technical and scientific applications are discussed.

1.1 Applications of atomic clocks

Satellite navigation

The Global Positioning System (GPS) is now routinely used for navigation purposes in everyday life. Key to the working principle of GPS navigation is the time keeping capability of the rubidium vapour cell clocks on-board the satellites. By receiving timing and location information from several satellites, GPS receivers can calculate their exact position on Earth. Future satellite navigation systems could benefit from the higher precision of optical atomic clocks. This could for instance enable satellite-aided aeroplane approaches at airports or devices sensitive enough to detect strain in the Earth's crust in order to predict earthquakes [1].

Relativistic geodesy

One future application of ultra stable optical atomic clocks is relativistic geodesy [2]. According to general relativity, the gravitational redshift causes the frequency of a clock to depend on the gravity potential it experiences. Near the surface of Earth the clock frequency change is approximately 1 part in 10^{16} per meter of height change. With optical clocks now reaching estimated fractional frequency uncertainties of few parts in 10^{18} [3, 4, 5], the comparison of two remotely located clocks would allow their height difference to be determined to within 1 cm [6]. Since this application compares remotely located clocks, more compact and reliable, commercially available ultra-stable optical clocks have to be developed before it can meet its full potential.

Fundamental science

Due to their high precision, optical atomic clocks can be used to test fundamental physical theories. Emerging physical theories aiming at unifying gravitation with the strong and electroweak interactions predict violations of the Einstein equivalence principle such as the time- and space-dependence

of fundamental constants. Comparing optical clocks with different clock frequencies over an extended period of time offers the possibility to search for drifts in the fine structure constant or the proton-to-electron mass ratio for instance. Such measurements have placed an upper limit on a possible drift of the fine structure constant of few parts in 10^{17} per year [7, 8]. Another way of testing the Einstein equivalence principle is to measure the gravitational redshift which causes a dependence of the clock frequency on the gravity potential it experiences. The Einstein Gravity Explorer mission for instance had the aim to search for violations in the Einstein equivalence principle by measuring the redshift of an optical clock deployed in space with an accuracy four orders of magnitude higher than previously achieved [9]. However, for a potential future implementation of such a mission, more progress in the development of space-qualified optical clocks is required.

1.2 Progress in the development of atomic clocks

The separated oscillating fields method, developed in 1949 by Ramsey [10], can be seen as the starting point of the era of modern atomic timekeeping—Ramsey was awarded the Nobel Prize in Physics in 1989 for his work. This technique, which is still employed in atomic clocks today, laid the foundation for the fast improvements in the performance of atomic clocks over the following decades. 60 years ago, the first accurate atomic clock—based on a hyperfine transition in the ground state of caesium 133-atoms—was developed by Essen and Parry at the UK National Physical Laboratory [11]. The time keeping capability of this frequency standard was more accurate than that of any other previously known reference. At the time, the second was defined by a fraction of a mean solar day, which was known to fluctuate over time. The work by Essen and Parry led to the redefinition of the second within the International System of Units (SI) in 1967 as the time period of 9 192 631 770 oscillations of the radiation of the ground state hyperfine transition in caesium 133-atoms. Since then, the accuracy of caesium atomic clocks has improved by approximately an order of magnitude per decade

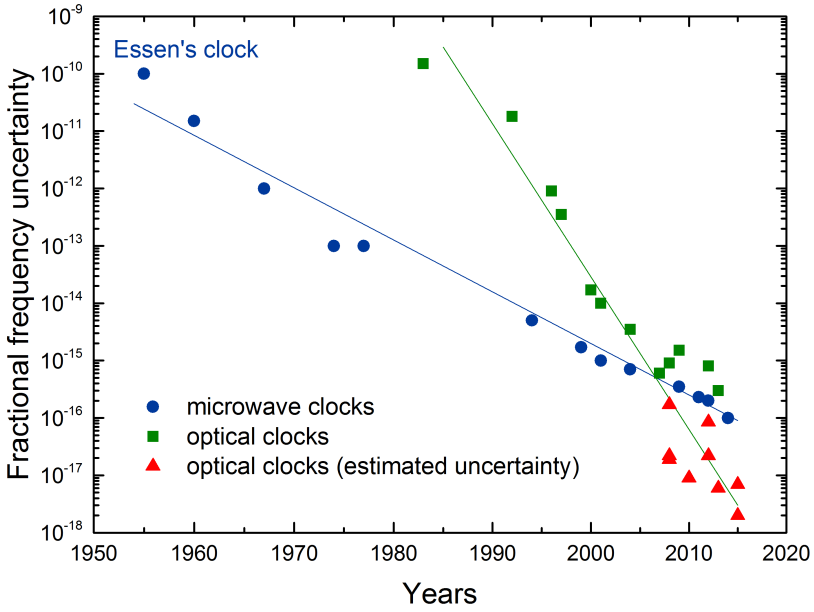

Figure 1.1: Progress in the fractional frequency uncertainties of atomic clocks over time (adapted from [13]). The fractional frequency uncertainties of microwave atomic clocks has improved at a rate of approximately one order of magnitude per decade over the last 60 years. Due to the dramatic improvement of the accuracy of optical atomic clocks by more than 2 orders of magnitude per decade, these clocks now have estimated fractional frequency uncertainties approximately two order of magnitude lower than the best primary frequency standards.

(see blue circles in figure 1.1), and today the best primary frequency standard (Cs-fountain clock) has a fractional frequency inaccuracy of 1.1×10^{-16} [12].

However, enabled by the development of the optical frequency comb (Nobel Prize in Physics 2005 to Hänsch and Hall), advances in atom manipulation (Nobel Prize in Physics 1997 to Chu, Cohen-Tannoudji and Phillips for the development of methods to cool and trap atoms with laser light) and improvements in laser stabilisation techniques, the accuracy of optical atomic clocks has been improving at an even faster rate over the last decade. As can be seen in figure 1.1, optical atomic clocks now have up to two orders of magnitudes higher estimated fractional frequency accuracies than their microwave counterparts. Currently, the best optical clocks are strontium

lattice clocks which have estimated fractional frequency uncertainties of a few parts in 10^{18} [3, 4, 5]. The green squares in figure 1.1 show optical clock uncertainties obtained from comparisons with primary caesium clocks. When the frequency of optical clocks is expressed in the SI-derived unit Hz, optical clocks cannot be more accurate then the best primary frequency standard. However, it has been shown that the estimated fractional frequency uncertainties of optical clocks (red triangles in figure 1.1) are lower than those of their microwave counterparts.

These advances might lead to a future redefinition of the second [14, 15]—this time, as a multiple of an optical oscillation period. However, several challenges have to be addressed before this can happen. Of the many different optical clocks which are currently being investigated as candidates for a redefinition of the second, no candidate clearly stands out from the others. Furthermore, to date only very few direct comparisons between optical clocks have been carried out. Comparing two cryogenic cooled strontium optical lattice clocks, Katori *et al.* [5] reported the best reproducibility to date of 7.5×10^{-18}. However, the comparison of clocks developed in the same laboratory by the same people is not regarded as the ultimate test because they experience the same environmental conditions and systematic errors common to both clocks will not be detected in such experiments. In order to confirm that all systematic effects are correctly accounted for, more thorough tests that compare optical clocks developed in different laboratories have to be carried out. Due to the limitation of absolute frequency measurements by the uncertainty of the primary frequency standard, only direct comparisons between optical clocks are suitable to verify their estimated uncertainties.

1.3 Comparing optical atomic clocks

The comparison of remotely located optical clocks is a challenging task in itself. When state of the art optical atomic clocks are to be compared with the highest possible accuracy, the only future option on an intercontinen-

tal scale is to employ transportable clocks. However, transportable clocks with fractional frequency uncertainties of few parts in 10^{18} do not currently exist. An alternative method with poorer performance is to use advanced variants of the standard microwave two-way satellite time and frequency transfer technique (TWSTFT) [16]. However, the fractional frequency instability of such methods is typically limited to approximately 1 part in 10^{15} (carrier phase TWSTFT [16]) which limits the fractional frequency accuracy of satellite-based clock comparisons to 1 part in 10^{15} [17]. The Atomic Clock Ensemble in Space (ACES) project [18] aims to achieve satellite transfer with a fractional frequency instability of few parts in 10^{17} for an averaging time of a couple of days by increasing the bandwidth of the transmitted signal. On a continental scale, optical fibre-based transfer techniques offer stability and accuracy performance sufficient for the comparison of state of the art optical clocks [19, 20]. Europe is in the unique position of having a relatively high density of state of the art optical clocks in a concentrated area which opens up the opportunity for comprehensive comparisons between different optical clocks. At the time of writing this thesis, the first fibre-based optical clock comparison experiments between various European institutes are under way; these include experiments between the National Physical Laboratory and the French National Measurement Institute (LNE-SYRTE) in Paris, and between institutes in Italy as well as between the German National Measurement Institute (PTB) in Braunschweig and LNE-SYRTE. If successful, these comparisons will form a crucial step towards a future redefinition of the second. Figure 1.2 shows the fractional frequency instability of satellite- and fibre-based transfer techniques and the fractional frequency instability of a state of the art strontium lattice clock.

Another challenge in the comparison of remotely located optical clocks is posed by general relativity. While the dependency of the clock frequency on the gravity potential it experiences could be employed for relativistic geodesy (section 1.1), it also limits the comparison of remotely located clocks. In order to compare optical clocks with a fractional frequency accuracy of few parts in 10^{18} the gravity potential on the Earth's surface has to be known to a level corresponding to a height uncertainty of the clocks of approximately

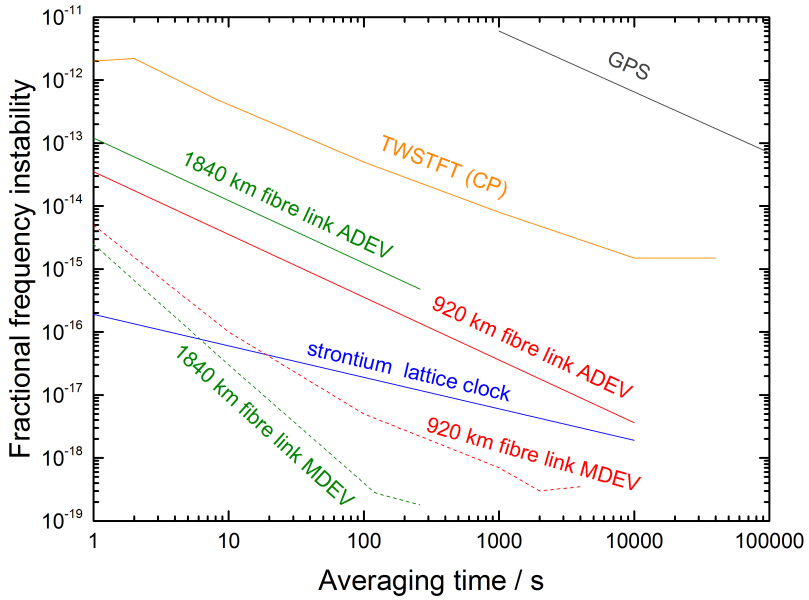

Figure 1.2: Fractional frequency instabilities of different frequency transfer techniques. The grey line shows the typical performance achieved with a standard GPS transfer method (Lombardi *et al.* GPS [21]). More advanced satellite transfer methods such as the carrier phase (CP) version of the standard two-way satellite time and frequency transfer technique (TWSTFST) have improved instabilities (orange line: TWSTFST CP [16]). Optical fibre transfer methods (red lines: Predehl *et al.* [19], green lines: Droste *et al.* [20]) can be employed to characterise the performance of a state of the art optical lattice clock (blue line: Ushijima *et al.* [5]). While the solid green and red lines give the Allan deviation which is the commonly used statistical tool to describe frequency instability, the dashed lines use the modified Allan deviation which is often used to evaluate the noise floor of a transfer method in a shorter averaging time.

1 cm. This cannot currently be achieved due to temporal and spatial fluctuations of the Earth's gravity potential caused by its rotation and its seismic activity [22]. This problem could be overcome in the future by employing an optical clock in a spacecraft on a well-known geostationary-orbit in space. Due to the large altitude, the spatial and temporal variations of the Earth's gravity potential are smoothed out on such an orbit, and knowledge of the altitude to within 40 cm is sufficient in order to determine the gravitational redshift at the 10^{-18} level [22].

1.4 Outline of thesis

The two main research areas covered in this thesis are photonic microwave synthesis and optical fibre-based time and frequency transfer methods (see section 1.3). Photonic microwave synthesis can be used to generate ultra-low noise microwave signals by phase-coherently dividing down an ultra stable optical reference (a Fabry-Pérot cavity or an optical atomic clock) using a femtosecond optical frequency comb. The main focus of this part of the thesis lies within the reduction of excess phase noise in the optical-to-electrical conversion process in the photonic microwave synthesis using a balanced optical-microwave phase detector. In the area of fibre-based time and frequency transfer methods, the thesis focusses on the development of a new time transfer technique using optical frequency combs. The structure of the thesis is as follows:

Chapter 2: Introduction to frequency metrology

This chapter introduces the different measures used to characterise frequency fluctuations, such as phase noise and Allan deviation, which will be used throughout this thesis. Furthermore, a brief description of the working principles of optical atomic clocks, frequency stabilised lasers and optical frequency combs is given.

Chapter 3: Ultra-low noise photonic microwave synthesis

Chapter 3 introduces the concept of ultra-low noise photonic microwave synthesis. The key steps in this process, namely the optical frequency division and the optical-to-electrical conversion, are presented along with a discussion of relevant noise processes and techniques to overcome the limitations associated with these. Finally, an overview of the state of the art performance is given.

Chapter 4: Low noise optical-to-electrical conversion using BOM-PDs

This chapter focusses on using a balanced optical-microwave phase detector (BOM-PD) to overcome the amplitude-to-phase noise conversion which is one of the main challenges in the optical-to-electrical conversion process. The working principle and noise limitations are discussed. This is followed by two experimental sections in which a mainly free-space BOM-PD design and a mainly fibre based BOM-PD design are investigated and their performance is discussed.

Chapter 5: Time and frequency dissemination via fibre

Chapter 5 introduces the main concepts of different time and frequency transfer techniques using optical fibre networks. The round-trip phase noise cancellation technique, which is used in the experimental work carried out in chapter 6 and 7, is described in detail. This is followed by a discussion of the state of the art performance.

Chapter 6: Comb based time and microwave transfer over a 50 km fibre spool

In this chapter a time transfer experiment over a 50 km fibre spool using an ITU-channel-filtered output from a mode-locked laser is presented. Firstly, a preliminary experiment on the round trip phase noise cancellation method which is used to stabilise the fibre link in the time transfer experiment is presented. Secondly, the time transfer experiment is described. Timing information is superimposed onto the optical pulse train from a mode-locked laser using an intensity modulation scheme. A detailed description of the calibration process of the time transfer set up is given along with a discussion of the uncertainty budget. Finally, the stability and the accuracy results of the time transfer experiment are presented.

Chapter 7: Comb-based time and frequency transfer over a 159 km long fibre network

In chapter 7, the time and microwave frequency transfer technique presented in chapter 6 is carried out on a 159 km long fibre link between NPL and Reading. Results of the time transfer and microwave transfer are presented.

Chapter 8: Conclusions and summary

In the final chapter chapter the work carried out in this thesis is summarised and conclusions are drawn. Perspectives for future work are also discussed.

2 Introduction to frequency metrology

This chapter presents the most commonly used measures and statistical tools in frequency metrology for the characterisation of frequency fluctuations. In addition, an introduction into optical atomic clocks, ultra-stable cavity-stabilised lasers and optical frequency combs is given.

2.1 Accuracy and stability

The performance of atomic frequency standards are characterised by their stability, accuracy and reproducibility. The stability—or more correctly instability—of a frequency standard is a measure of how much its frequency fluctuates over time. The reproducibility states the extent to which nominally identical frequency standards can produce the same frequency in practice. The term accuracy is used in two different ways. Usually, accuracy refers to how well the frequency of an atomic standard, such as an optical atomic clock, can be related to the definition of the unit hertz, which is derived from the SI unit second. The term accuracy is also used to specify how well systematic frequency offsets in atomic frequency standards can be quantified. In the field of optical atomic clocks, one import aspect is to determine the independent variables and the boundary conditions which completely describe these systematic offsets with the highest possible accuracy. All three performance measures depend on the sensitivity of the atomic resonance transition to environmental perturbations and how well these can

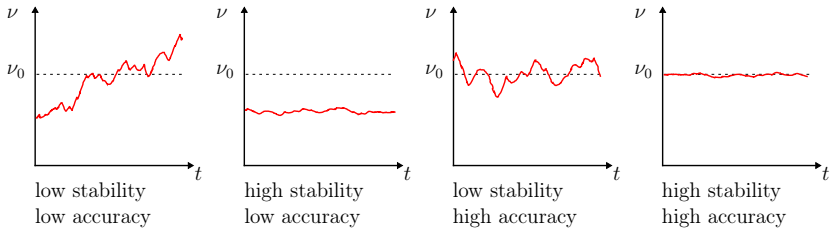

Figure 2.1: Frequency references with different stabilities and accuracies are shown to illustrate the difference between the two measures; adapted from [23].

be controlled or measured.

The instantaneous fractional frequency deviation of a clock transition can be written as

$$\frac{\nu(t) - \nu_0}{\nu_0} = \varepsilon + y(t), \tag{2.1}$$

where ν_0 is the nominal frequency, ε is a systematic frequency offset and $y(t)$ is the random frequency fluctuation which can be described by suitable statistical measures. Figure 2.1 illustrates the difference between stability and accuracy for a frequency standard. For an atomic frequency reference it is desirable to have both high accuracy and high stability because the stability of a clock determines the averaging time required to verify its accuracy or to determine systematic offsets.

2.2 Characterisation of frequency instability

2.2.1 Frequency instability

Ignoring systematic offsets, the signal from an atomic frequency standard can be written as

$$V(t) = V_0[1 + \alpha(t)] \sin[2\pi\nu_0 t + \varphi(t)], \tag{2.2}$$

where V_0 is the carrier amplitude, $\alpha(t)$ are the fractional amplitude fluctuations, ν_0 is the nominal clock frequency and $\varphi(t)$ are the instantaneous phase fluctuations. Frequency fluctuations can be described as frequency instabil-

ity in the time domain or as phase noise in the frequency domain. Assuming that ν_0 is stable enough for $\varphi(t)$ to stay within an interval of $(-\pi, \pi)$ for short time-scales, the frequency fluctuations can be characterised by the phase noise. For longer time-scales, frequency drifts by more than half a cycle of ν_0 leave $\varphi(t)$ ambiguous. In this case, the stability of the reference is characterised by the frequency fluctuations and the clock signal can be written as

$$V(t) = V_0[1 + \alpha(t)] \sin\left[2\pi\nu_0 t + 2\pi \int \Delta\nu(t)dt\right]; \tag{2.3}$$

the instantaneous frequency fluctuation or frequency noise

$$\Delta\nu(t) = \frac{1}{2\pi}\frac{d\varphi(t)}{dt}, \tag{2.4}$$

causes a deviation of the instantaneous frequency $\nu(t)$ from the nominal frequency ν_0:

$$\nu(t) = \nu_0 + \frac{1}{2\pi}\frac{d\varphi(t)}{dt}. \tag{2.5}$$

The random phase fluctuations $\varphi(t)$ can also be converted into time fluctuations, which are referred to as phase-time fluctuations and are given by:

$$x(t) = \frac{\varphi(t)}{2\pi\nu_0}. \tag{2.6}$$

The instability of atomic clocks is usually expressed in fractional terms because this allows direct comparison of oscillators working at different frequencies. The fractional frequency fluctuation $y(t)$ is defined as the normalised frequency deviation; $y(t)$ can be related to the various measures of frequency fluctuations as follows:

$$y(t) = \frac{\nu(t) - \nu_0}{\nu_0} = \frac{\Delta\nu(t)}{\nu_0} = \frac{1}{2\pi\nu_0}\frac{d\varphi(t)}{dt} = \frac{dx(t)}{dt}. \tag{2.7}$$

Figure 2.2 summarises the relationship between phase noise, absolute frequency fluctuations, fractional frequency fluctuations and phase-time fluc-

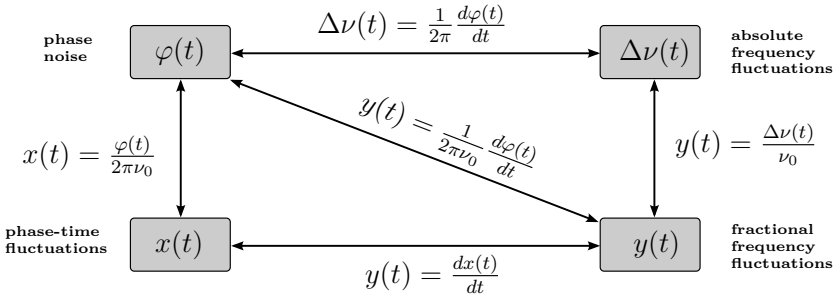

Figure 2.2: Schematic showing the relation between the most common measures used to describe frequency instability; adapted from [24].

tuations.

2.2.2 Phase noise

Phase noise is usually expressed as $S_\varphi(f)$ which is defined as the one-sided power spectral density (PSD) of the random fluctuations of $\varphi(t)$ as a function of the Fourier frequency f. The units of $S_\varphi(f)$ are $\mathrm{rad^2\,Hz^{-1}}$, but usually phase noise is shown in a log-log scale plot and expressed in units of $\mathrm{dBrad^2\,Hz^{-1}}$. Another commonly used representation of phase noise is the single side-band phase (SSB) noise $\mathscr{L}(f)$ which is defined as

$$\mathscr{L}(f) = \frac{1}{2} S_\varphi(f); \tag{2.8}$$

in practice, the quantity

$$\mathscr{L}(f) = 10 \log \left[\frac{1}{2} S_\varphi(f) \right] \tag{2.9}$$

is used which is expressed in units $\mathrm{dBc\,Hz^{-1}}$ where dBc refers to the power relative to the carrier.

The relations between $S_\varphi(f)$ and the one-sided PSDs of $x(t)$, $\Delta\nu(t)$ and $y(t)$, which can also be used to describe the frequency instability of an os-

cillator, are described by the following equations:

$$S_x(f) = \frac{1}{(2\pi\nu_0)^2} S_\varphi(f); \tag{2.10}$$

$$S_{\Delta\nu}(f) = f^2 S_\varphi(f); \tag{2.11}$$

$$S_y(f) = \frac{f^2}{\nu_0^2} S_\varphi(f). \tag{2.12}$$

2.2.3 Allan variance

For some of the most common random noise processes present in atomic clocks, the standard deviation depends on the sample size as well as the averaging time and diverges with increasing number of data points. For the purpose of characterisation and comparison of stable frequency standards the Allan variance and the Allan deviation, which do not diverge for common clock noise processes, are introduced [25]. The Allan variance is defined as the infinite time average of the two-sample, zero dead time variance of the fractional frequency deviation

$$\sigma_y^2(\tau) = \frac{1}{2} \left\langle [\bar{y}(t+\tau) - \bar{y}(t)]^2 \right\rangle, \tag{2.13}$$

where τ is the sample time between measurements and $\bar{y}(t)$ is the average fractional frequency deviation given by:

$$\bar{y}(t) = \frac{x(t+\tau) - x(t)}{\tau}. \tag{2.14}$$

The Allan deviation $\sigma_y(\tau)$ is given by the square root of the Allan variance.

In practice, for a finite data set of M fractional frequency deviation measurements the infinite time average in equation 2.13 can be replaced by the simple mean, and an approximation of the Allan variance can be calculated as:

$$\sigma_y^2(\tau) = \frac{1}{2(M-1)} \sum_{j=1}^{M-1} \left[\bar{y}_{j+1} - \bar{y}_j\right]^2. \tag{2.15}$$

2.2.4 Modified Allan variance

Another commonly used stability measure is the modified Allan variance or the modified Allan deviation [26, 27]. The modified Allan variance includes an additional averaging compared to the normal Allan variance. For a set of M frequency measurements the modified Allan variance for an averaging time of $\tau = m\tau_0$, where m is the averaging factor and τ_0 is the measurement interval, the modified Allan variance can be estimated as:

$$\mathrm{Mod}\,\sigma_y^2(\tau) = \frac{1}{2m^4(M-3m+2)} \sum_{j=1}^{M-3m+2} \left\{ \sum_{i=j}^{j+m-1} \left(\sum_{k=i}^{i+m-1} [\bar{y}_{k+m} - \bar{y}_k] \right) \right\}^2 . \tag{2.16}$$

2.2.5 Conversion between frequency fluctuation spectra and Allan variance

The Allan variance is obtained as a function of the sampling time τ by averaging n adjacent fractional frequency deviations to give a new average fractional frequency deviation with observation time $\tau' = n\tau$ as input into equation 2.13. The statistical analysis of the fractional frequency fluctuations of atomic clocks with the Allan deviation is very useful because it reveals information about the underlying noise processes.

The close-to-the-carrier noise processes of clock signals can be modelled using the following power-law equations:

$$S_\varphi(f) = \sum_{i=-4}^{0} b_i f^i; \tag{2.17}$$

$$S_y(f) = \sum_{i=-2}^{i=2} h_i f^i; \tag{2.18}$$

where the coefficients b_i and h_i characterise the strength of the noise processes that are proportional to f^i. As can be seen in figure 2.3, the different noise types have straight lines in the log-log scale noise spectra with char-

	slope in		
noise process	$S_\varphi(f)$	$\sigma_y(\tau)$	$\mathrm{Mod}\,\sigma_y(\tau)$
white phase	f^0	τ^{-1}	$\tau^{-3/2}$
flicker phase	f^{-1}	τ^{-1}	τ^{-1}
white frequency	f^{-2}	$\tau^{-1/2}$	$\tau^{-1/2}$
flicker frequency	f^{-3}	τ^0	τ^0
random walk of frequency	f^{-4}	$\tau^{1/2}$	$\tau^{1/2}$

Table 2.1: Summary of the slopes of common noise processes in phase noise, Allan deviation and modified Allan deviation log-log plots.

acteristic slopes of $i \times 10\,\mathrm{dB/decade}$.

The relation between the PSDs of the phase fluctuations and the fractional frequency fluctuations of equation 2.12 can be used for an exact conversion in both directions between the two spectra. In contrast, the conversion from the PSDs to the Allan variance is only an approximation, and it is not possible to convert from the Allan variance to the PSDs due to the fact that both white and flicker phase noise have the same slope in the Allan variance. However, as can be seen in figure 2.3, the Allan variance produces different slopes with respect to the integration time for other common noise processes. This is very useful for the characterisation and the reduction of noise processes, at different time-scales, in atomic clocks. The conversion coefficients from $S_y(f)$ to $\sigma_y^2(\tau)$ can be looked up in tables such as the ones provided in [26, 28]. In table 2.1 the slopes of the Allan deviation and the modified Allan deviation for the most common noise processes are summarised. While the Allan deviation generates the same slopes for white phase and flicker phase noise, the modified Allan deviation is able to distinguish between them.

2.2.6 Timing jitter and time deviation

In synchronisation applications, phase fluctuations are commonly described by the integrated timing jitter x_{rms} which is obtained by integrating the phase noise over the bandwidth B of the system and converting it into

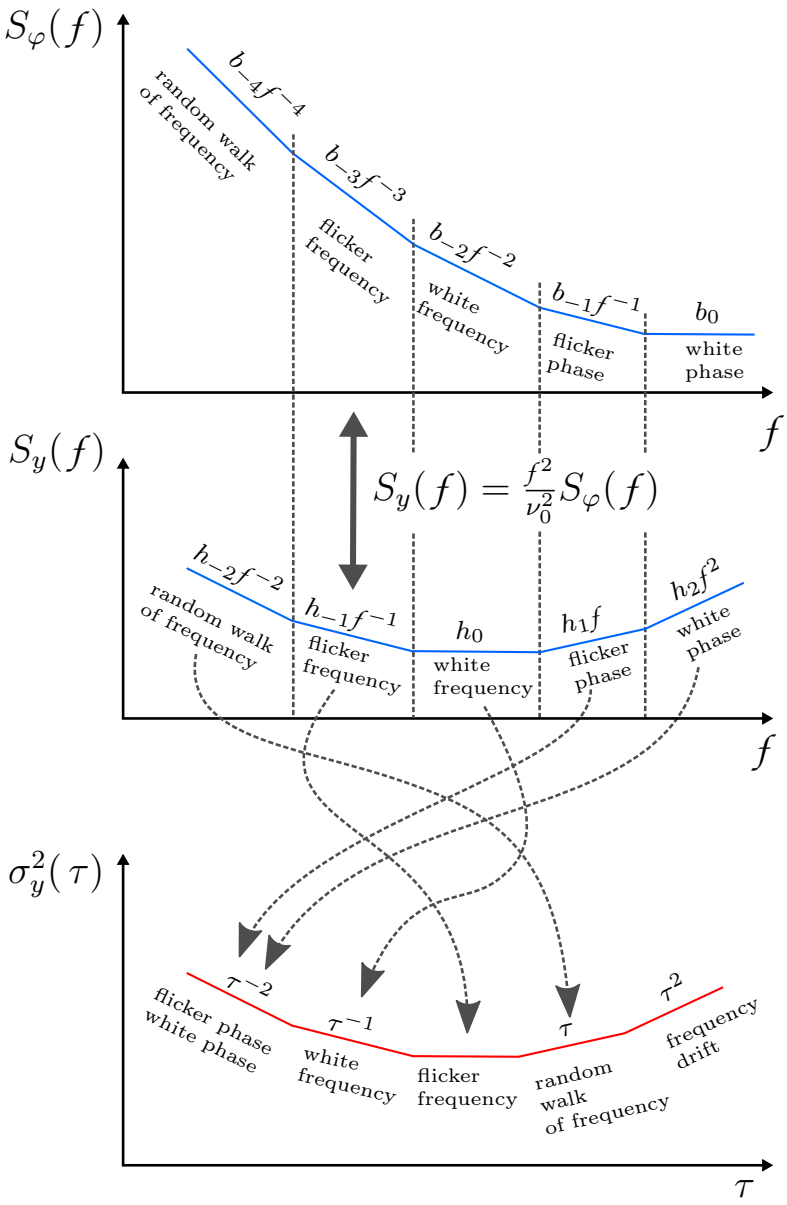

Figure 2.3: Conversion between phase noise, frequency noise and Allan Variance for common noise types; adapted from [24].

phase-time fluctuations:

$$x_{\mathrm{rms}} = \frac{1}{2\pi\nu_0}\sqrt{\int_B S_\varphi(f)df}. \tag{2.19}$$

In timing applications the stability is analysed using the time deviation which is defined as

$$\sigma_x(\tau) = \frac{\tau}{\sqrt{3}}\mathrm{Mod}\,\sigma_y(\tau), \tag{2.20}$$

where $\mathrm{Mod}\,\sigma_y(\tau)$ is the modified Allan deviation. The time deviation gives the rms change in the mean value of the phase-time fluctuations averaged over an interval τ with respect to adjacent phase-time averages. It is particularly useful for characterising the time error of a time transfer system or a time source. The slope of the time deviation in a log-log plot is increased by +1 compared to the modified Allan deviation; white phase noise is proportional to $\tau^{-1/2}$, flicker phase noise produces a slope of zero and white frequency noise is proportional to $\tau^{1/2}$.

2.2.7 Phase noise measurement

One of the most commonly used phase noise measurement techniques is based on mixing the signal under study with a reference signal of the same frequency using a double-balanced mixer (DBM). The mixer multiplies the two input signals and if they are in phase quadrature, i.e. have a phase difference of $\frac{\pi}{2}$, the voltage output of the mixer is proportional to the phase fluctuations. If the sum frequency is filtered out by a low-pass filter and the phase fluctuations between the two signals, $\Delta\varphi(t) = \phi_2(t) - \phi_1(t)$, are small, the output voltage of the mixer can be approximated as:

$$V_{\mathrm{out}}(t) \propto \sin\left[\phi_1(t) - \phi_2(t)\right] \approx V_0\Delta\varphi(t). \tag{2.21}$$

The output signal from the mixer is sent to a fast Fourier transform (FFT) analyser and the phase noise PSD is given by

$$S_\phi(f) = \left[\frac{V_{\mathrm{rms}}(f)}{K_d}\right]^2, \tag{2.22}$$

where K_d is the phase sensitivity of the mixer in units $\mathrm{V\,rad^{-1}}$. In order to reduce the effect of the amplitude fluctuations on the phase noise measurement, the mixer must be saturated.

Since the phase sensitivity of a mixer depends on the input powers and frequencies, calibration is required before every measurement if these parameters are changed. The sensitivity can be measured with a calibrated phase shifter or by producing a slight offset between the two input frequencies and measuring of the slope of the generated beat signal around the zero crossing. For the beat signal method the sensitivity is given by:

$$K_d = \frac{\Delta V}{\Delta \varphi} = \frac{\Delta V}{2\pi \frac{\Delta t}{T}}, \tag{2.23}$$

where T is the period of the beat signal, and ΔV is the voltage change corresponding to the time interval Δt for which the response of the mixer is linear.

2.2.8 Frequency synthesis

In many applications, new frequencies are generated by multiplying or dividing a reference frequency. If these processes are noise free, the fractional frequency instability of the output signal is the same as that of the input signal while the absolute frequency fluctuations and the phase fluctuations are multiplied or divided. Assuming an output frequency ν_{out} is generated from an input frequency ν_{in} with

$$\nu_{\mathrm{out}} = \frac{N}{M}\nu_{\mathrm{in}}, \tag{2.24}$$

where N and M are integer numbers, the phase fluctuations are given by:

$$\varphi_{\text{out}}(t) = \frac{N}{M}\varphi_{\text{in}}(t). \tag{2.25}$$

Therefore, the PSDs of the phase and frequency fluctuations are $(N/M)^2$ times that of the input fluctuations. If a frequency is divided by a factor of 100, for instance, the phase noise PSD is divided by a factor of 10^4; this effect can be used to generate ultra-low noise microwave signals from optical frequency standards using an optical frequency comb as an optical frequency divider (see section 3.2.1).

2.3 Optical atomic clocks

The three key components of an atomic clock are an atomic resonance transition, a local oscillator which can be stabilised to this transition and a suitable counter to turn the atomic frequency standard into a clock. Advantages of atomic clocks compared to their mechanical counterparts are that the quality factors—which are defined as $Q = \nu_0/\Delta\nu$, where $\Delta\nu$ is the linewidth of the clock transition and ν_0 is the transition frequency—are orders of magnitude higher and that they can be better isolated from environmental effects. Furthermore, atomic clocks offer superior reproducibility because their transition frequencies are determined by fundamental physical constants, i.e. different clocks based on the same atom species should exhibit the same resonance frequency.

Optical atomic clocks are based on high-Q optical resonance transitions in laser-cooled single ions or ensembles of neutral atoms trapped in an optical lattice. An interrogation oscillator, which consists of a laser locked to an ultra-stable Fabry Pérot cavity, is locked to the atomic transition and an optical frequency comb phase coherently divides down the clock frequency to the countable microwave or rf domain.

The best ion clocks are based on quantum logic Al^+ ions which are laser cooled using Mg^+ ions. These clocks have an estimated fractional frequency

accuracy of approximately 9×10^{-18} [29]. Strontium optical lattice clocks have recently achieved fractional frequency uncertainties and fractional frequency instabilities at the 10^{-18} level [3, 4, 5]; a performance significantly better than that of the best microwave frequency standards. The advantage of optical clocks compared to microwave clocks is that their operating frequencies are five orders of magnitude higher while most systematic frequency offsets are frequency independent, i.e. by moving to higher frequencies the fractional frequency uncertainty can be decreased. Similarly, the achievable linewidths in optical and microwave clocks are similar but the instability of an atomic clock is inversely proportional to the clock transition frequency:

$$\sigma_y(\tau) \approx \frac{\Delta\nu}{\nu_0\sqrt{N}}\sqrt{\frac{T_c}{\tau}}. \tag{2.26}$$

Equation 2.26 gives the theoretical quantum projection noise limit, where N is the number of atoms detected in a single measurement, T_c is the time of a single measurement cycle and τ is the averaging time. Optical clocks therefore have the potential to offer instabilities orders of magnitude lower than that of microwave clocks. Lattice clocks can achieve higher stabilities than single ion clocks because the instability is proportional to $N^{-1/2}$. For instance, a neutral lattice clock with a quality factor of 10^{15} and 10^4 atoms would exhibit a theoretical quantum noise limited instability of 10^{-17} at 1 s which would be a hundred times lower than that of a single ion clock with the same quality factor.

The instability of a clock is of major practical importance because it determines the statistical resolution of a frequency measurement that can be reached within a certain averaging time. Since the instability of a clock is proportional to $\tau^{-1/2}$, a reduction in the instability by factor of 100 would lead to a reduction in the averaging time by a factor of 10^4 in order to reach a desired uncertainty. Low clock instabilities are therefore crucial for the evaluation of systematic effects in optical clocks; stability improvements usually lead to uncertainty improvements due to reduced measurement times.

2.4 Frequency stabilisation of lasers

Optical clocks require ultra-stable lasers for two reasons. Firstly, optical clock transitions have natural linewidths of a few Hz or less and because the resonance results from light-atom interaction, the interrogation laser linewidth must be similar. Secondly, the stability of state-of-the-art optical clocks is often limited at short averaging times by the Dick effect, which originates from the dead time in each measurement cycle due to the need for atom preparation and readout. During this dead time, the laser frequency cannot be compared to the atom transition and this results in a down-conversion of higher frequency laser noise into low-frequency noise on the clock signal [1]. Therefore, stabilised lasers with narrow linewidths are a critical component of optical clocks; recent improvements in state-of-the-art optical strontium lattice clocks [3, 4] have been directly enabled by the availability of more stable interrogation lasers [30].

The Pound-Drever-Hall method [31] is the most commonly used technique to stabilise the frequency of a laser to a single longitudinal and transverse resonance mode of a high-finesse ultra-stable Fabry-Pérot cavity. When the laser is tightly locked to the cavity, its frequency stability is limited by the length fluctuations of the cavity. Therefore, the design and the environmental isolation of the cavity are crucial for achieving high frequency stability. In order to reduce length fluctuations of the cavity, the cavity mirrors are optically contacted to mechanically rigid spacers. Furthermore, the cavity spacers as well as the mirror substrates are typically made out of low-thermal-expansion material such as Ultra Low Expansion (ULE) glass and the cavity is placed in an evacuated chamber which is temperature stabilised around the zero crossing of the thermal expansion coefficient of the spacer material. In addition, the cavity system is mounted on a vibration-isolation platform and shielded against acoustic noise by a box. The cavity length can also fluctuate due to acceleration-driven deformation of the cavity spacer and mirrors. This effect can be reduced by using a suitable mechanical support and design of the cavity spacer. For instance a spherical cavity design [32]

and a cubic cavity geometry [33] were demonstrated to have low orientation and acceleration sensitivities.

Under such conditions, the frequency stability is fundamentally limited by the mechanical thermal fluctuations (Brownian motion) of the cavity spacer, the mirror substrates and the mirror coatings [34], but special cavity designs can reduce the thermal noise floor. Using a long spacer (29 cm) and mirror substrates made from high mechanical Q material, Jiang *et al.* [30] achieved a thermal-noise-limited fractional frequency instability of 1.4×10^{-16} and a laser linewidth of 250 mHz. Due to their low mechanical loss, crystal materials are also employed in cavity design to reduce the thermal noise floor. For instance, Cole *et al.* [35] reported a tenfold reduction of the thermal noise floor by using crystalline mirror coatings rather than dielectric mirror coatings. Kessler *et al.* [36] demonstrated a cavity design in which the cavity spacer and the mirror substrates are made out of single-crystal silicon; the cavity, which is operated at a temperature of 124 K where the thermal expansion coefficient of silicon is zero and the mechanical loss is small, is capable of supporting a laser with a linewidth of 40 mHz and a fractional frequency instability of 1×10^{-16} at short averaging times. This is the most stable oscillator of any kind so far reported at short time-scales. Their cavity has a predicted thermal-noise-limited fractional frequency instability of 6×10^{-17} which is dominated by the contribution from the mirror coatings; with all-crystalline cavity designs instabilities of 1×10^{-17} and below appear feasible [36].

While laser stabilisation to ultra-stable cavities has so far produced the highest stabilities, several alternative approaches exist. For instance, a laser can be locked to an optical fibre delay line [37]; this technique has recently demonstrated sub-Hz laser linewidths and fractional frequency instabilities of 5×10^{-15} at 1 s [38]. Although not suitable for state-of-the-art optical clocks, this method could be advantageous for less demanding applications due to its simplicity and low-cost. Other promising alternatives which might lead to improved stabilities are spectral hole burning [39] and the superradiant laser [40].

2.5 Optical frequency combs

Since optical frequencies have of the order of 10^{15} oscillations per second, it is not possible to directly count them; hence, for a long time, one of the main questions in the field of frequency metrology was how optical frequencies could be measured. Some laboratories built dedicated frequency chains that linked specific optical frequencies to the microwave domain using a series of phase-locked oscillators; however, these systems were complex and required significant resources [41]. Therefore, a more simple and flexible technique for the measurement of optical frequencies was required.

Almost 40 years ago, it had already been demonstrated that the sharp lines in the frequency domain produced by the pulsed output of a mode-locked-laser could be used to measure frequency intervals in the optical domain [42]. However, due to the lack of octave spanning optical laser sources, it took more than 20 years until the first demonstration of octave spanning optical frequency combs [43, 44]. Since then, optical frequency combs, which can be used to measure optical frequencies with unparalleled precision and link optical frequencies to the microwave domain as well as to other parts of the optical spectrum, have revolutionised the field of frequency metrology. Frequency combs form the clockwork of optical atomic clocks and are used for high-precision spectroscopy, to name just two applications. The significance of the optical frequency comb was reflected in the award of the 2005 Nobel Prize in Physics to Hänsch and Hall for their contributions to its development [45, 46].

A frequency comb is generated from a periodic train of ultra-short optical pulses emitted from a mode-locked laser with repetition rate f_r which is given by

$$f_r = \frac{1}{T} = \frac{v_g}{2L}; \tag{2.27}$$

where T is the cavity round-trip time, L is the cavity length and v_g is the mean group velocity inside the cavity. For a single pulse with a Gaussian envelope in the time domain, the Fourier transform corresponds to a Gaussian distribution in the frequency domain with a width that is inversely propor-

tional to the temporal width of the envelope. The Fourier transform of a train of pulses separated by a fixed time interval T yields a comb of regularly spaced frequencies, where the mode spacing is the repetition rate of the mode-locked laser. The well defined comb lines, which are also referred to as comb teeth, are generated by constructive interference of successive optical pulses which occurs at the inverse of the pulse spacing and harmonics thereof. The Fourier transform relationship between time and frequency resolution ensures that any spectrometer that can distinguish individual comb lines, is not capable of resolving individual pulses [41].

As can be seen in figure 2.4, the carrier and the envelope experience a relative phase difference of $\Delta\varphi_{\mathrm{ceo}}$ after every round trip due to a difference between the group velocity and the phase velocity inside the cavity. Hence, the optical modes of the comb are usually not exact multiples of the repetition rate, but are offset by the carrier envelope offset (CEO) frequency:

$$f_0 = \frac{1}{2\pi}\frac{d\varphi_{\mathrm{ceo}}(t)}{dt} = \frac{\Delta\varphi_{\mathrm{ceo}}(t)}{2\pi T} = \frac{f_r \Delta\varphi_{\mathrm{ceo}}(t)}{2\pi}. \tag{2.28}$$

The frequencies of the comb modes can thus be expressed in terms of the radio frequencies f_r and f_0 and the frequency of the nth mode is given by:

$$\nu_n = n f_r + f_0, \tag{2.29}$$

where n is the mode number which is usually of the order of $\approx 10^5$–10^6.

In most frequency metrology applications, both these rf frequencies have to be stabilised. The repetition rate or a harmonic thereof can be obtained via photodetection of the pulse train. In order to determine f_0, the comb spectrum has to span an octave, or close to that, which necessitates pulse durations at the fs level because of the inverse relation between the spectral width of the comb and the temporal width of the pulse. The advent of the Kerr-lens mode-locked Titanium-sapphire (Ti:sapphire) femtosecond laser [48] and microstructured fibres or photonic crystal fibres, which can further widen the spectrum via four-wave mixing or self-phase modulation, were therefore crucial for the development of octave-spanning combs. Most

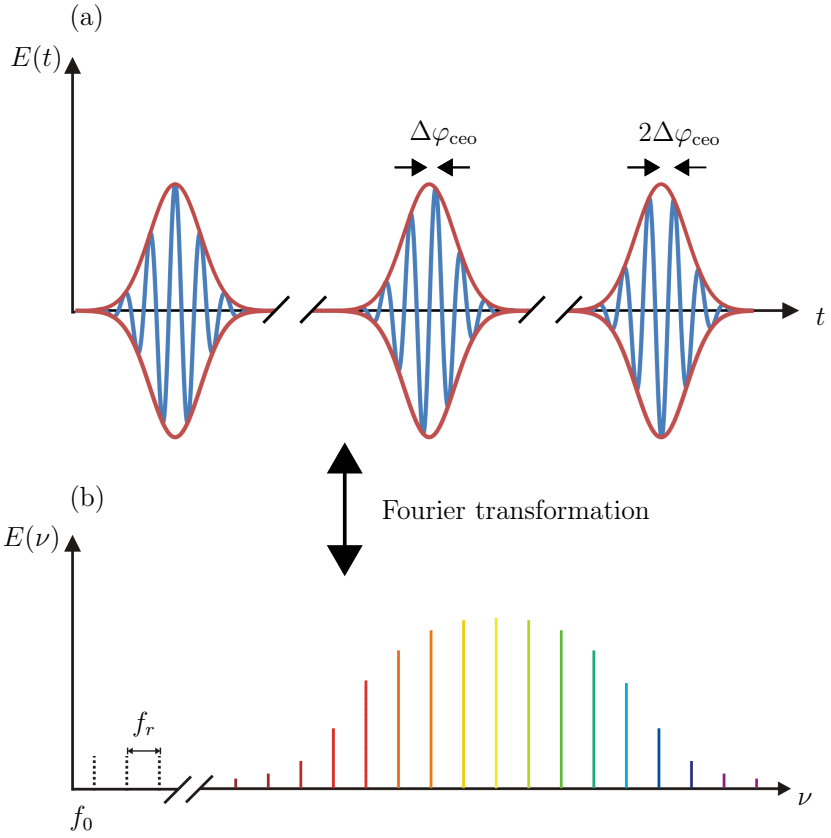

Figure 2.4: Time domain (a) and frequency domain (b) pictures of the output of a mode-locked laser. The Fourier transformation of a periodic optical pulse train from a mode-locked laser with a repetition rate f_r yields a comb of equidistant optical modes which are separated by f_r. A constant phase offset of $\Delta\varphi_{\mathrm{ceo}}$ from pulse to pulse between the carrier and the envelope inside the laser cavity leads to a shift in the frequency comb modes by f_0; adapted from [47].

combs still use these microstructured fibres or highly nonlinear fibres to widen the spectrum to an octave although octave-spanning Ti:sapphire lasers have been demonstrated [49]. The simplest technique to detect f_0 is the f–$2f$ self-referencing scheme which is illustrated in figure 2.5. Comb lines at the lower end of the comb spectrum centred around the line with mode number m are frequency doubled and beat against the comb lines centred around the line with mode number $2m$ which yields the CEO frequency:

$$2(mf_r + f_0) - (2mf_r + f_0) = f_0. \tag{2.30}$$

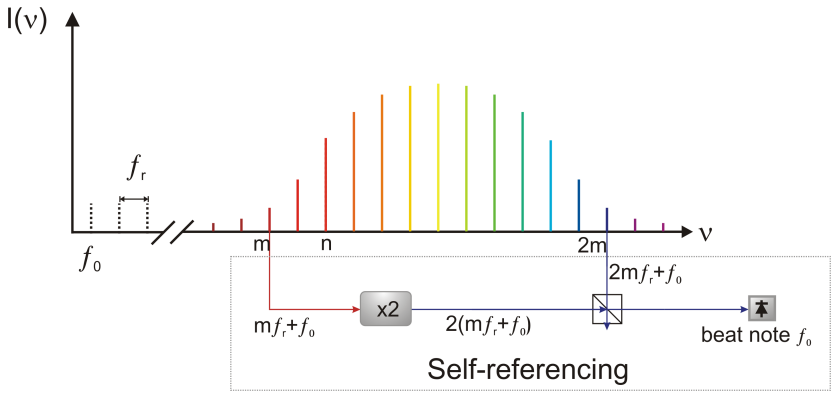

Figure 2.5: This schematic shows the self-referencing method which can be used to measure the carrier-envelope offset frequency by beating frequency doubled optical modes centred around mode number m with optical modes centred around mode number $2m$.

A frequency comb can be stabilised in different ways depending on the application at hand. When both f_0 and f_r are locked to an rf frequency standard, such as a hydrogen maser or a Cs clock, the frequency comb acts as an optical frequency synthesiser which produces up to millions of known frequencies across the visible spectrum [50]. Such an optical frequency synthesiser can be used for absolute frequency measurements by generating an rf beat signal f_{beat} between the frequency under study, e.g. a laser locked to an optical atomic clock transition with frequency ν_{clock}, and the nearest comb tooth with mode number l on a photodiode. The frequency of the clock transition is then given by:

$$\nu_{\text{clock}} = f_0 + l f_r \pm f_{\text{beat}}, \tag{2.31}$$

where the mode number m and the sign of the beat frequency can usually be determined by making a coarse measurement of ν_{clock} using a wavemeter. Such a frequency measurement is called absolute because the optical frequency is measured against the primary Cs standard which is used to define the SI unit second, from which the unit hertz is derived.

In another stabilisation scheme, which will be described in the following chapter, a comb mode is tightly locked to an ultra-stable optical frequency

standard while f_0 is locked to an rf frequency standard. This method can be used to generate ultra-low noise microwave signals.

2.6 Conclusions and summary

This chapter gave an introduction to the field of frequency metrology. The various measures commonly used to characterise frequency instability have been presented. Furthermore, a short introduction to optical atomic clocks, ultra-stable laser and optical frequency combs has been given. The next chapter describes how a frequency comb and an optical frequency reference can be used for ultra-low noise photonic microwave generation.

3 Ultra-low noise photonic microwave synthesis

In this chapter, photonic microwave synthesis will be described, which uses an optical frequency comb as an optical frequency divider to phase coherently divide down an optical reference to the microwave domain (see section 3.2). Photodetection of the pulse train generates microwave signals at harmonics of the repetition rate (see section 3.3). As will be described in this chapter, both these processes can add excess phase noise to the generated microwave signals. These challenges along with techniques to overcome them are discussed. Finally, the state-of-the-art performance in photonic microwave synthesis is presented.

3.1 Motivation

The generation and distribution of low-noise microwave signals is required for many applications such as coherent radar systems [51], communication systems [52], deep-space communication [53], synchronisation at large facilities such as phased-array radio telescopes and free-electron lasers [54, 55], precision spectroscopy and the realisation of atomic time [56, 57]. These applications are limited by the fractional frequency instability of microwave signals generated by commercially available ultra-low-noise quartz oscillators (8×10^{-14} at 1 s [58]). The use of cryogenic sapphire oscillators, which can generate ultra-low-noise microwave signals with fractional frequency stabilities of 5.4×10^{-16} at 1 s [59], is not an option for wider applications due

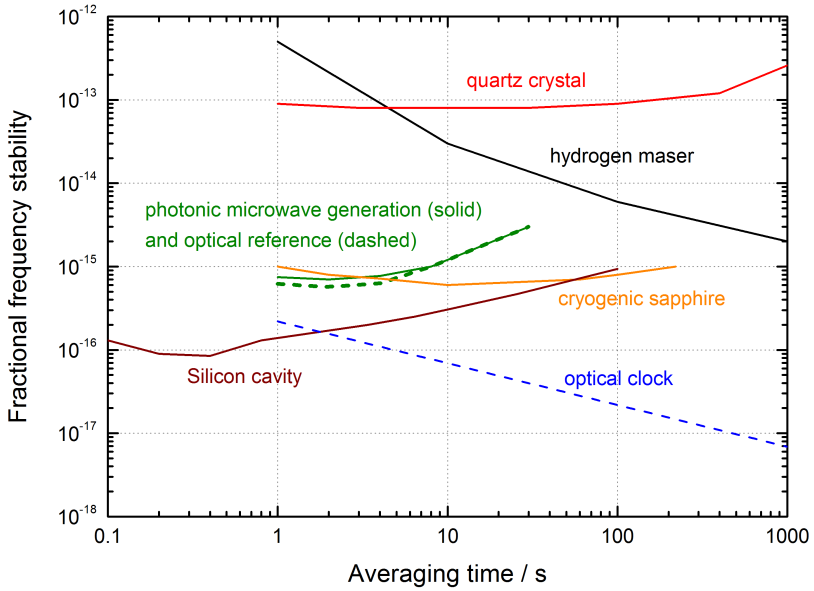

Figure 3.1: Frequency stabilities of different oscillators. Dark: hydrogen maser (CH1-75A, Quartzlock Products [60]); red: ultra-stable quartz oscillator (OCXO 8607, Oscilloquartz [58]); orange: cryogenic sapphire oscillator [59]; blue dashed: state-of-the-art optical lattice clock stability [4]; green: state-of-the-art photonic oscillator (solid) and optical reference cavity (dashed) [61]; brown: state-of-the-art ultra-stable silicon Fabry-Pérot cavity [36].

to their high maintenance costs and difficult operation. An alternative approach is the photonic generation of microwave signals, in which the stability of a laser locked to an ultra-stable Fabry-Pérot cavity is transferred to the repetition rate of an optical frequency comb and subsequently transferred to the electrical domain via photodetection of the pulse train [62]. As discussed in section 2.4, lasers locked to high-finesse Fabry-Pérot cavities made of ultra-low expansion glass are amongst the most stable oscillators available in any region of the electromagnetic spectrum. The phase noise of such photonic oscillators has been shown to be comparable to the best microwave oscillators available [61, 63]. In figure 3.1 the stabilities of several microwave and optical oscillators are shown for comparison.

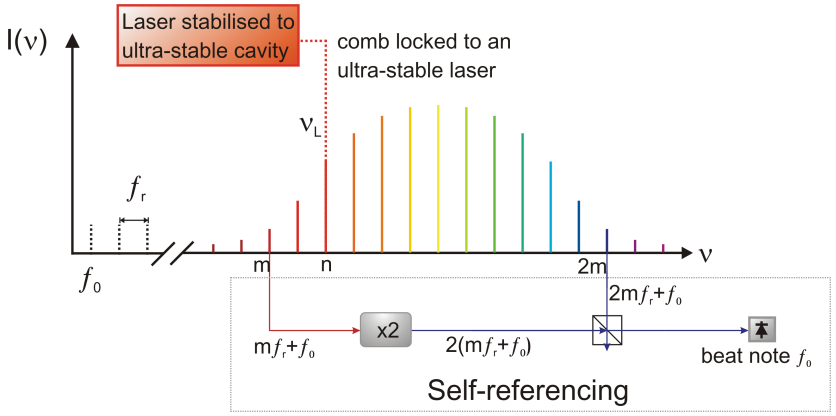

Figure 3.2: A self-referenced optical frequency comb stabilised to an optical frequency standard acts as an optical frequency divider, linking the optical to the rf domain. Here, the nth mode of a comb is locked to a cavity-stabilised laser.

3.2 Optical frequency division

3.2.1 Working principle

When an optical frequency comb is locked to an optical frequency standard, the stability of the optical frequency standard can be transferred to millions of other comb lines [64] and to the microwave domain. This capability of the frequency comb to act as an optical frequency divider, which phase coherently divides down an optical frequency standard to the repetition rate of the mode-locked laser, is used to count the clock oscillations of optical atomic clocks [65] and for ultra-low noise photonic microwave generation [61, 63]. In figure 3.2 the principle of optical frequency division is illustrated. The nth tooth of a self-referenced comb is phase-locked to a cavity stabilised laser of frequency ν_L, which in the case of an optical clock would in turn be stabilised to an optical atomic transition; the repetition rate of the comb is then given by:

$$f_r = \frac{\nu_\mathrm{L} - f_0}{n}. \tag{3.1}$$

Usually the comb would be offset locked to the optical reference, creating an additional beat frequency in the equation above, but to explain the concept,

here it is assumed that the comb is directly locked to the laser.

As described in section 2.2.8, the division process reduces the PSD of the phase fluctuations by the square of the division ratio. Due to the large ratio between optical and microwave frequencies (ν_L/f_r) in equation 3.1, an optical frequency comb locked to an ultra-stable optical reference can be used to generate ultra-low noise microwave signals. For instance, optical frequency division of an optical reference at 200 THz to a microwave signal at 10 GHz is accompanied by a reduction in phase noise of 86 dB. However, it has to be ensured that the phase locking of the frequency comb to the optical reference and the optical-to-electrical conversion do not add excess phase noise in the photonic microwave synthesis. In the next section, the noise contribution of the frequency comb in the optical frequency division will be presented.

3.2.2 Excess phase noise of the frequency comb

The process of transferring the fractional frequency instability of an optical reference to millions of comb lines, by optically phase-locking a frequency comb to the optical reference, is usually accompanied by a degradation of the instability because the noise of the free-running frequency comb is not perfectly suppressed. The fractional frequency instability contribution of the frequency comb in this process is often referred to as the residual fractional frequency instability (or just residual instability) of the frequency comb. For the purpose of low noise photonic microwave synthesis, it is desirable to reduce the residual instability of the frequency comb below that of the optical reference, so that the stability of the generated microwave signal is not degraded by the frequency comb. The residual instability of optical frequency combs locked to cavity-stabilised lasers has been studied extensively [66, 67, 68]. In order to measure the residual instability of frequency combs, usually two combs are locked to the same optical reference and some comb lines are compared via generation of a heterodyne beat on a photodiode. The fluctuations of the optical reference do not contribute in this measurement because they are common to both combs.

The main challenge in locking a frequency comb to an optical reference, is that a very large locking bandwidth is required in order to suppress the noise of the free-running comb below that of the optical reference [68]. The locking of f_r is more demanding than that of f_0 as its instability is multiplied by the mode number n (comb modes: $\nu_n = nf_r + f_0$). For fibre combs, this is even more challenging than for Ti:sapphire combs because they exhibit larger frequency noise at high offset frequencies of f_r. This necessitates locking bandwidths above 100 kHz for the repetition rate phase-locked loop, which is very challenging to achieve with piezo transducers because they exhibit mechanical resonances at tens of kHz.

This technical problem can be overcome by combining a low bandwidth piezo-actuated mirror (large dynamic range) with a high bandwidth intracavity electro-optic modulator (EOM) (small dynamic range). Intracavity EOMs with bandwidths of up to 2 MHz have been demonstrated [69, 70, 71], which can be used for tightly locking f_r to an optical reference.

Although not discussed here, it should be noted that using a frequency comb as a transfer oscillator [72, 73], offers an alternative method for transferring the stability of an optical reference to other parts of the optical spectrum and the microwave domain, without the need for tight locking of the comb to the optical reference.

Since the first demonstration of optical frequency division, significant improvements to the residual stability of optical frequency combs has been achieved. Ma *et al.* achieved a residual fractional frequency instability of Ti:sapphire combs of 2.3×10^{-17} at 1 s [74]. Using fibre combs with intracavity EOMs, Nicolodi *et al.* demonstrated a residual fractional frequency instability of 4×10^{-18} at 1 s, corresponding to the lowest fractional frequency instability of combs reported to date [64]. As can be seen in figure 3.3, such residual fractional frequency instabilities of frequency combs are more than an order of magnitude below the instability of a state-of-the-art optical lattice clock. Thus, frequency combs can support the best optical frequency standards available, and transfer their stability across the comb modes and to the microwave domain. Once this is achieved, the remaining challenge is to maintain this stability in the optical-to-electrical conversion.

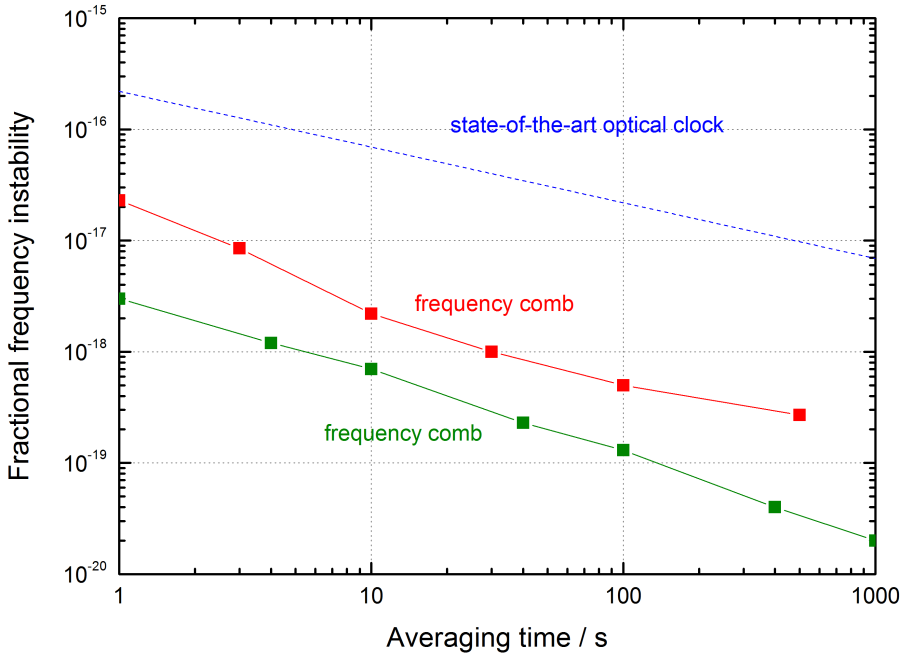

Figure 3.3: Residual fractional frequency instability of frequency combs. Red: Comparing the frequency stability of several Ti:sapphire combs locked to the same optical reference, Ma *et al.* [74]; green: Comparing the frequency stability of two fibre combs locked to the same optical reference, Nicolodi *et al.* [64]; blue dashed: state-of-the-art optical lattice clock, Nicholson *et al.* [4].

This challenge is the topic of the next section.

3.3 Optical-to-electrical conversion

There are several noise processes in the optical-to-electrical conversion which usually degrade the stability of the extracted microwave signal. Overcoming these noise limitations requires more advanced techniques than direct photodetection of the pulse train. In this section, those noise processes, along with the advanced methods to overcome them, are presented. The instability contribution of the optical-to-electrical conversion to the photonic microwave synthesis will be referred to as the residual fractional frequency instability (or just residual instability) of the optical-to-electrical conversion—in the case of phase noise, the noise contribution will be refereed to as the residual phase

noise of the optical-to-electrical conversion. In order to measure the residual contribution of the optical-to-electrical conversion, two identical extraction set-ups are used to generate the same harmonic of the repetition rate from a common frequency comb. When comparing those two set-ups, the noise contribution of the frequency comb is common and does not contribute to the instability.

3.3.1 Thermal and shot noise

In the following, the thermal and shot noise limitation for the photodetection of a harmonic of f_r of a comb is presented (after [75]). Thermal noise (Johnson noise) is an electronic noise that originates from the thermal agitation of the charge carriers inside a resistive element at equilibrium. The single-sided power spectral density (PSD) of the thermal noise in a 1 Hz bandwidth is given by

$$\overline{v_n^2} = 4k_\mathrm{B}TR \qquad [\mathrm{V}^2] \tag{3.2}$$

where k_B is the Boltzmann constant, T is the temperature (300 K) and R (50 Ω) is the resistance. In a typical p-i-n photodetector circuit, the contribution of the thermal noise to the SSB phase noise is given by

$$\mathscr{L}_\mathrm{thermal}(f) = 10\log\frac{k_\mathrm{B}TR}{2P_\mathrm{rf}} \approx -177 - 10\log P_\mathrm{rf} \qquad [\mathrm{dBc\,Hz^{-1}}] \tag{3.3}$$

where P_rf is the rf power of the harmonic of the repetition rate in mW, measured across 50 Ω.

The shot noise in the photodetection process arises from the discreteness of photons and electrons. It is characterised by fluctuations of the photocurrent around its mean value and originates from photon noise and photoelectron noise. Photon noise is caused by the purely random time intervals between photon arrival times in laser light. The number of photons that reach the detector in a given time interval is governed by Poissonian statistics and varies around a mean value. The photoelectronic noise is caused by the randomness of photon absorption in a photodetector with a quantum efficiency less than unity and is thus also governed by Poissonian

statistics. The shot noise in a 1 Hz bandwidth is given by

$$\overline{I_n^2} = 2eI_{\text{avg}} \qquad [\text{A}^2] \tag{3.4}$$

where e is the elementary charge and I_{avg} is the average DC photocurrent. Assuming a 50 Ω termination this shot noise results in a SSB phase noise of the extracted microwave signal of

$$\mathscr{L}_{\text{shot}}(f) = 10\log\frac{eI_{\text{avg}}R}{4P_{\text{rf}}} \approx -177 + 10\log\left(\frac{I_{\text{avg}}}{P_{\text{rf}}}\right) \qquad [\text{dBc}\,\text{Hz}^{-1}] \tag{3.5}$$

where I_{avg} is in units of mA and P_{rf} is in units of mW. Below saturation, thermal noise and shot noise have the following dependence on the optical power:

$$\mathscr{L}_{\text{thermal}}(f) \propto \frac{1}{P_{\text{rf}}} \propto \frac{1}{P_{\text{opt}}^2}, \tag{3.6}$$

$$\mathscr{L}_{\text{shot}}(f) \propto \frac{I_{\text{avg}}}{P_{\text{rf}}} \propto \frac{1}{P_{\text{opt}}}. \tag{3.7}$$

For low optical powers the thermal noise floor improves at a rate of 20 dB per decade while at higher optical powers the limit is given by the shot noise floor which improves at a rate of 10 dB per decade. However, the optical power cannot arbitrarily be increased since the phase noise caused by amplitude-to-phase conversion in saturated photodiodes can be significantly higher than the phase noise due to thermal and shot noise.

3.3.2 Thermal and shot noise floor reduction techniques

Due to their robustness and reliability fibre frequency combs are the preferred choice for microwave synthesis outside the laboratory. However, the repetition rate of commercial fibre combs is typically in the hundreds of MHz range while 1 GHz Ti:sapphire combs are routinely operated and repetition rates of 10 GHz have been achieved [76]. The generation of 10 GHz microwave signals with low-repetition-rate combs results in a more rapid onset of saturation in the photodiodes due to the unnecessary high peak

optical power of the pulses—since the peak optical power is inversely proportional to the repetition rate, it is advantageous to operate at high repetition rates. Saturation in the photodiode leads to a reduction in the SNR of the microwave signal and AM-PM conversion (see section 3.3.3). The rf power available after photodetection from a low repetition rate fibre comb is therefore lower than that available from a high repetition rate Ti:sapphire comb. For 250 MHz fibre combs and commercial high linearity photodiodes, saturation in the photodiodes usually prevents the generation of microwave signals with phase noise floors much better than $-140\,\mathrm{dBc\,Hz^{-1}}$ [77]. Much research has therefore been undertaken in order to overcome this limitation and several techniques and devices, which will be presented in the following, have been developed for this purpose.

Repetition rate multiplication

One such method is repetition rate multiplication, which can be achieved with a mode-filtering Fabry-Pérot cavity [75, 78] or a series of either fibre-based or free-space, cascaded Mach-Zehnder interferometer (MZI) [75, 77, 79]. The MZI approach is the preferred choice since it offers better phase noise performance, is more robust and easier to realise [75]. Haboucha *et al.* [77] demonstrated a repetition rate multiplication of a 250 MHz fibre comb by a factor of 8, using three cascaded MZI consisting of standard 50/50 fibre couplers which were spliced to the required lengths. Each MZI doubles the number of pulses by delaying the pulses in one arm relative to the other arm by half of the period of the pulse train. This resulted in an increase of the rf power of the 12 GHz harmonic of 18 dB, which led to a reduced phase noise floor of $-164\,\mathrm{dBc\,Hz^{-1}}$ at 10 MHz.

Since repetition rate multiplication has proven to be very effective at reducing the phase noise floor at high offset frequencies, most ultra-low noise microwave experiments employ this technique.

Shot noise correlations in the photodetection of ultrashort optical pulses

In 2013, Quinlan *et al.* [80] demonstrated how shot noise correlations in ultrashort pulses can be exploited to generate microwave signals with shot noise below that of the generally accepted, time-invariant shot noise of light. Instead of having a uniform distribution, the shot noise of ultrashort pulses is localised around the pulses. This periodic structure opens up a route to make the shot noise contribution negligible by reducing it below the thermal noise floor level. In order to operate in this regime, the duration of the optical pulses must be of the order of 1 ps or below. For longer optical pulses the normal shot noise formula from equation 3.5 applies. Generating 10 GHz signals from an optical pulse train, Quinlan *et al.* demonstrated a phase noise floor at high offset frequencies of $-179\,\mathrm{dBc\,Hz^{-1}}$, which was 5 dB below the time-invariant shot noise. This is the lowest shot noise floor reported to date for the generation of a 10 GHz harmonic from an optical pulse train. It should be noted that in order to achieve this result, in addition to operating below the normal shot noise regime, high-power modified uni-traveling carrier photodiodes [81]—which produced rf powers of 10 dBm—were employed. These photodiodes will be described in the following section.

High-power, high-linearity modified uni-traveling carrier (MUTC) photodiodes

High-power, high linearity modified uni-traveling carrier photodiodes [81, 82, 83] offer another approach for the noise floor reduction. Uni-traveling-carrier photodiodes (UTC) can cope with higher power and have an improved linearity compared to normal p-i-n photodiodes. The space charge screening effect is mitigated by employing only electrons with higher saturation velocities than holes as charge carriers in the collection region. Further progress has been enabled by modified uni-traveling carrier (MUTC) photodiodes which have a cliff layer that controls the relative electric field strengths in the absorber and collector regions. Due to the cliff layer, higher electric fields in the absorber region are possible. This enables higher currents, and

hence higher rf powers.

It has been shown that when illuminated by cw lasers, MUTC photodiodes can effectively suppress space charge screening effects, limiting their output power by thermal failure rather than by saturation. Thus, the rf power can be increased by thermal management of the photodiodes. Flip-chip bonding of those photodiodes to substrates with high thermal conductivities has shown to offer the best thermal dissipation. Bonding to diamond has provided rf output powers of 33 dBm at 10 GHz from an MUTC photodiode, illuminated by an amplitude modulated cw laser [83]. Rouvalis *et al.* used MUTC photodiodes, flip-chip bonded to AlN, to generate 10 GHz signals with saturation powers of 21 dBm from an optical pulse train [82]. Such high rf power levels would correspond to a thermal noise floor of approximately $-197\,\mathrm{dBc\,Hz^{-1}}$. In order to avoid saturation, a series of 5 free space delay line interferometers was employed for repetition rate multiplication in this experiment. Due to their high power handling capability these MUTC photodiodes can therefore significantly reduce the noise floor in photonic microwave generation.

3.3.3 AM-PM conversion

When a fast p-i-n photodiode is illuminated by an optical pulse train, high pulse energies can cause the photodiode to saturate and generate excess phase noise in the demodulated electronic signals at harmonics of f_r. The main cause of this additional phase noise is the amplitude-to-phase noise (AM-PM) conversion which transfers power fluctuations of the frequency comb into phase fluctuations of the generated microwave signals. This effect, which has been studied extensively [77, 84, 85, 86], is one of the main challenges in low-noise photonic microwave synthesis [87].

The AM-PM conversion in photodiodes is characterised by a reduction in the peak photocurrent, an increase in the pulsetail of the electronic signal and a phase shift between the optical carrier and the generated microwave signal at a harmonic of f_r [88]. These phenomena are caused by space charge screening in the intrinsic part of the p-i-n junction. Since this effect

α (rad)	$20\log(\alpha)$ (dB)
2	+6
0.1	−20

Table 3.1: Typical AM-PM conversion coefficients in commercial photodiodes and the corresponding phase noise contribution from the relative intensity noise (RIN) of the laser.

is intensity dependent, it is of particular concern under pulsed operation as the peak optical power can be 1000 times higher than in cw operation [79]. Such high optical intensities lead to high charge carrier densities in the absorption layer of the photodiode which, combined with the finite carrier mobility in the depletion region, generate a non-negligible electric field. This field is oppositely oriented to the external bias, thus causing a reduction of the carrier velocity and leading to AM-PM conversion [89].

The AM-PM conversion coefficient α gives the phase fluctuation per relative power fluctuation of the laser. It strongly depends on the specific design of the photodetector and varies with the optical energy per pulse, the frequency of the generated harmonic of the repetition rate, the bias voltage and the temperature of the device. For p-i-n photodiodes under typical operating conditions, α lies in the range of 0.1 rad to 2 rad [89, 90, 91]. The contribution of the relative intensity noise (RIN) of a laser to the SSB phase noise of the generated microwave signal due to AM-PM conversion is given by:

$$\mathscr{L}_{\mathrm{RIN}}(f) = \mathrm{RIN}_{\mathrm{SSB}}(f) + 20\log(\alpha). \tag{3.8}$$

In table 3.1 the phase noise contribution below the RIN is calculated for common values of α in p-i-n photodiodes. Such high AM-PM conversion coefficients combined with high RIN from commercial combs can add a significant amount of phase noise in the optical-to-electrical conversion. For instance, in table 3.2, the contribution of the RIN of the commercial Er:fibre comb used in this thesis (see section 4.2 and 4.4.1 for details) for $\alpha = 2$ rad is calculated. In the next section, a technique for the mitigation of the AM-PM conversion will be described.

f	$\mathrm{RIN}(f)(\mathrm{dBc\,Hz^{-1}})$	$\mathscr{L}_{\mathrm{RIN}}(f)(\mathrm{dBc\,Hz^{-1}})$
1 Hz	−106	−100
10 kHz	−124	−118

Table 3.2: The phase noise contribution of the RIN of a commercial fibre comb in the photodetection is calculated using $\alpha = 2\,\mathrm{rad}$.

3.3.4 Operation at a zero crossing of the AM-PM conversion

The dependence of the AM-PM conversion coefficient on the optical power per pulse has been studied extensively [89, 90]. It varies between positive and negative values and exhibits vanishing points which can be used to reduce the AM-PM conversion. Some experiments have used power stabilisation techniques to demonstrate a reduction of the AM-PM conversion by reducing the RIN of the laser without operating at a vanishing point [92, 93, 94]. By stabilising the optical power of their combs via feedback to the pump current controls, Zhang *et al.* [94] demonstrated a residual optical-to-electrical phase noise performance of the 11.55 GHz harmonic of $-120\,\mathrm{dBc\,Hz^{-1}}$ at 1 Hz, and a residual fractional frequency instability of 1.1×10^{-16} at 1 s and 1.5×10^{-19} at 1000 s.

Other experiments have focussed on operating close to a vanishing point of α [89, 90, 91]. Zhang *et al.* have carried out a thorough analysis of α in commercial photodiodes operated at 1550 nm [89]. From their characterisation of α and measurements of the long term power fluctuations of their commercial fibre comb, they calculate values for α. For initial tuning to a vanishing point, they predict an α of 0.003 rad after three days due to drifts in the amplitude of their laser by 0.1 percent. Allowing for up to 1 percent of amplitude drifts they predict an α of 0.03 rad for longer time scales. These values of α would correspond to an AM-PM suppression of 30 dB and 50 dB respectively, which is a significant improvement compared to normal photodetection.

The main drawback of this AM-PM reduction method is that the exact

locations of the zero crossings of α differ from device to device and strongly depend on the optical energy per pulse and the bias voltage as well as the temperature. For some applications such as large-scale experiments it would be impractical to characterise every single photodiode and carefully control the environmental conditions to ensure operation near the vanishing point. However, since operation at a vanishing point of α was shown to significantly reduce the AM-PM conversion, almost all state-of-the-art low-noise photonic microwave synthesisers operate at a vanishing point of α. To avoid degradation of the performance, the optical power of the comb and the temperature of the photodiode are usually stabilised.

3.4 State of the art performance

Photonic microwave synthesis

In 2013, Fortier *et al.* [79] demonstrated state-of-the-art low-noise photonic-microwave synthesis. A combination of several techniques was employed in order to achieve this performance. They compared two individual photonic microwave synthesisers, locked to individual optical references (cavity-stabilised laser), and comprised of individual frequency combs (1 GHz Ti:sapphire) and optical-to-electrical conversion systems (MUTC photodiodes). Since illumination of the MUTC photodiodes with the pulse train resulted in saturation, the repetition rate of the comb was doubled using free-space MZI pulse interleavers in order to increase the available rf power. The two photodiodes were furthermore operated at nulls of α in order to suppress AM-PM conversion. This resulted in a phase noise of the 10 GHz harmonic of $-104\,\mathrm{dBc\,Hz^{-1}}$ at 1 Hz and $-177\,\mathrm{dBc\,Hz^{-1}}$ at 2 MHz. At low offset frequencies the phase noise was limited by the optical cavity, and at high offset frequencies the phase noise was limited by an rf amplifier used in the phase noise measurement system. These are the best results in terms of short term frequency stability and close to carrier phase noise for any room-temperature 10 GHz oscillator, comparable to only the very best cryogenic dielectric oscillators.

Optical-to-electrical conversion

In 2014, Baynes *et al.* [95] demonstrated the lowest residual phase noise for optical-to-electrical conversion reported to date. Two MUTC photodiodes were used to generate 10 GHz signals from a common fibre comb. The photodiodes were operated at a vanishing point of α, and the power of the comb as well as the temperature of the photodiodes were stabilised. For increased linearity, the repetition rate of the fibre comb was multiplied from 208 MHz to 3.3 GHz using cascaded fibre MZIs. They achieved a residual phase noise of $-131\,\mathrm{dBc\,Hz^{-1}}$ at 1 Hz and $-170\,\mathrm{dBc\,Hz^{-1}}$ at 10 kHz and a frequency stability of 1.4×10^{-17} at 1 s and 5.5×10^{-20} at 1000 s. The phase noise at high offset frequencies was limited by uncorrelated noise of an EDFA, and for lower offset frequencies the phase noise was limited by the flicker noise of the photodiodes to $-135\,f^{-1}\,\mathrm{dBc\,Hz^{-1}}$.

3.5 Conclusions and summary

Significant progress has been made over the last decade in the generation of low-noise and high-stability photonic microwave signals. As can be seen in figure 3.4, the residual stability of a frequency comb, acting as an optical frequency divider, is sufficient to support state-of-the-art optical clocks. Furthermore, the optical-to-electrical conversion can also preserve the stability of the best optical clocks. The residual stability of the best optical-to-electrical conversion reported to date by Baynes *et al.* is more than an order of magnitude below the performance of the best optical clocks. This opens up a route for the generation of the most-stable microwave signals generated by any source, with long term stabilities orders of magnitude better than those achieved with the best cryogenic sapphire oscillators.

For shorter time-scales, the highest stability frequency sources are provided by ultra-stable optical Fabry Pérot cavities. The phase noise contribution of thermal noise limited cavities to a 10 GHz signal is shown in figure 3.5. Thermal noise limited cavities exhibit flicker frequency noise which has a slope of f^{-3} in the phase noise PSD. The dashed green lines

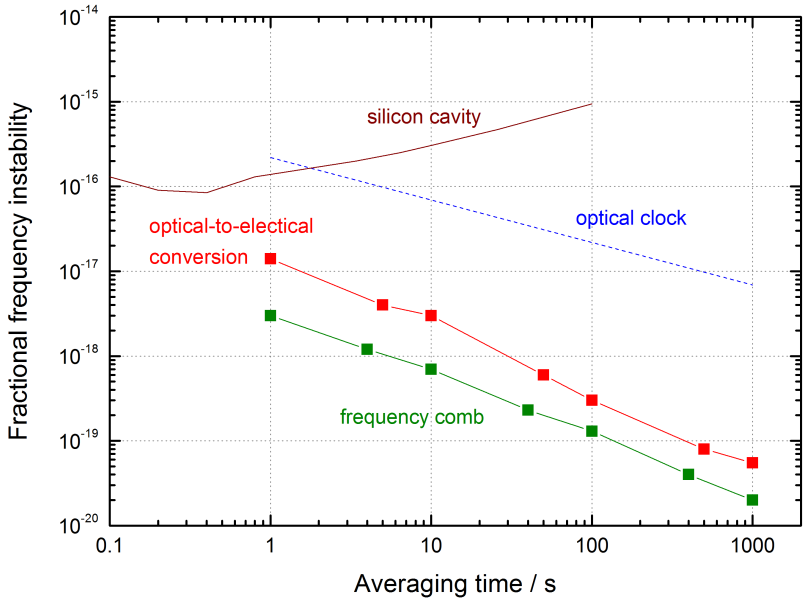

Figure 3.4: Fractional frequency stability contributions of several components of a photonic microwave generator. Green: residual frequency stability of a frequency comb, Nicolodi *et al.* [64]; blue dashed: state-of-the-art optical lattice clock stability; Nicholson *et al.* [4]; brown: state-of-the-art ultra-stable silicon Fabry-Pérot cavity, Kessler *et al.* [36]; red: residual stability of state-of-the-art optical-to-electrical conversion (MBW:10 Hz), Baynes *et al.* [95].

show the phase noise contribution of thermal noise limited cavities with fractional frequency stabilities of 1×10^{-15} and 1×10^{-16}. With state-of-the-art cavities approaching a thermal noise limited fractional frequency stabilities of 1×10^{-16} [30], photonic microwave synthesis with phase noise of $-124\,\mathrm{dBc\,Hz^{-1}}$ at 1 Hz appears feasible.

Advances in photonic microwave generation have already produced microwave signals with one of the lowest phase noise levels available from any source, comparable to only the very best sapphire oscillators. The orange line in figure 3.5 shows the phase noise of state-of-the-art photonic microwave generation which was limited by the optical reference cavity at low offset frequencies [61].

As described in this chapter, the noise contribution of frequency combs and the optical-to-electrical conversion have been significantly reduced. At

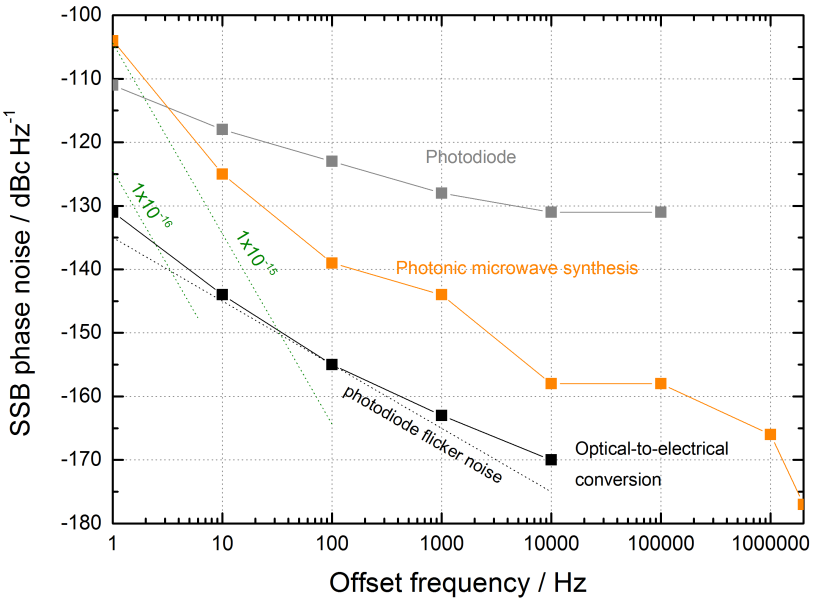

Figure 3.5: SSB phase noise contributions of different components in the photonic microwave generation scaled to 10 GHz. Grey: typical contribution of direct photodetection and rf amplification; orange: State-of-the-art photonic microwave generation, Fortier *et al.* [61]; solid black: state-of-the-art optical-to-electrical conversion, Baynes *et al.* [95]; dashed black: flicker noise of the photodiode used in [95]; dashed green: phase noise of thermal noise limited cavities with fractional stabilities of 1×10^{-15} and 1×10^{-16} at 1 s, assuming perfect optical frequency division.

high offset frequencies, repetition rate multiplication, operation below the normal shot noise limit and high-power MUTC photodiodes have greatly reduced the noise floor up to $-177\,\mathrm{dBc\,Hz^{-1}}$ [61]. At low offset frequencies, the use of photodiodes operated at a zero crossing of α have reduced the phase noise to the flicker noise floor of photodiodes. The best optical-to-electrical conversion reported to date by Baynes *et al.* approaches this flicker noise limit between 1 Hz and 10 kHz [95]. An alternative approach for the reduction of the AM-PM conversion which does not require operation at a zero crossing of α is based on the balanced optical-microwave phase detector (BOM-PD). This method will be described in the following chapter.

The next generation of optical cavities have projected thermal noise limited frequency stabilities below 1×10^{-16} [36], corresponding to a phase noise

contribution of $-124\,f^{-3}\,\mathrm{dBc\,Hz^{-1}}$. As a result, the phase noise contribution of the cavity surpasses that of the flicker noise of the photodiodes at only a few Hz, making it the main limitation in photonic microwave synthesis at low offset frequencies. The reduction of flicker noise in semiconductor devices remains a difficult technical challenge, yet to be overcome.

4 Low noise optical-to-electrical conversion using BOM-PDs

As discussed in the previous chapter (section 3.3.3), the AM-PM conversion in the optical-to-electrical conversion process is one of the key challenges in photonic microwave synthesis. It can be overcome by operating at a zero crossing of the AM-PM conversion coefficient (section 3.3.4). In this chapter, the balanced optical-microwave phase detector (BOM-PD), which offers an alternative approach for the suppression of AM-PM in the optical-to-electrical conversion, will be described. The BOM-PD was originally developed by Kim and Kärtner at MIT [96]. In the first section of this chapter, the working principle of the balanced optical-microwave phase detector is described, and an analysis of noise processes is given. In the second section, results from free-space BOM-PD set-ups are presented. The third section presents results on low-noise optical-to-electrical conversion using improved fibre BOM-PDs. While designed to suppress the AM-PM conversion, the BOM-PD from Kim *et al.* only had an AM-PM conversion coefficient similar to that found in a saturated photodiode [97]. The improved fibre BOM-PD presented here overcomes this limitation by making two key changes to the set-up which resulted in an AM-PM suppression of 60 dB (this work was published in Optics Express [98]).

4.1 Working principle and noise analysis

The main purpose of the BOM-PD is overcome the limitations caused by excess phase noise due to AM-PM conversion and a low SNR in the photodetection of an optical pulse train. In order to achieve this, the timing error between the optical pulses and the extracted harmonic of f_r is transferred into an intensity imbalance in the optical domain, before the photodetection. In the following, this process will be described in detail, and the shot noise limit will be derived.

As described in [99], an intensity imbalance which depends on the timing information in the optical domain can be generated by splitting an optical pulse train into two paths and amplitude modulating the pulse trains with a signal from a voltage-controlled oscillator (VCO) that has a 180° phase difference between the two paths. Photodetection of this intensity imbalance with a balanced detector yields an error signal which can phase-lock the VCO to a harmonic of f_r. When the PLL is closed, the VCO signal is adjusted so that its zero crossings overlap with the optical pulses, and the two arms have balanced intensities.

Such a scheme could be realised with a Mach-Zehnder intensity modulator, i.e. a Mach-Zender interferometer with a phase modulator in one arm. However, Kim points out that such a system would not be suitable for long term stable operation due to non-common noise in the two paths of the interferometer caused by temperature and air fluctuations as well as mirror vibrations. This issue can be alleviated by using a Sagnac interferometer with counterpropagating pulse trains so that both beams experience the same fluctuations. As will be discussed in the following, this approach is adopted in the BOM-PD. In the case of the Mach-Zehnder interferometer, the timing error between the VCO and the optical pulse train is transferred into an intensity imbalance between the two interferometer outputs by phase modulating only one of the two beams. When a Sagnac interferometer is used, both beams pass through the phase modulator and in order to modulate only one of the counterpropagating beams, a unidirectional phase

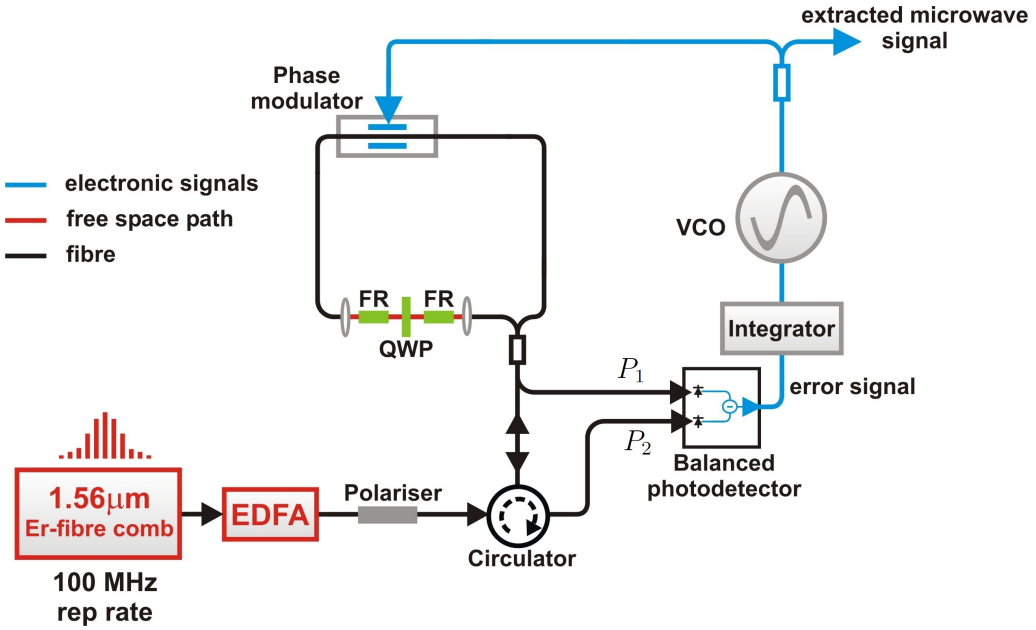

Figure 4.1: Schematic of the BOM-PD set-up. EDFA: erbium-doped fibre amplifier; FR: Faraday rotator; QWP: quarter waveplate; VCO: voltage controlled oscillator. All fibres after the polariser are polarisation maintaining.

modulator is employed. Unidirectional phase modulation can be achieved by using a travelling-wave phase modulator in which a microwave driving signal generates an electromagnetic travelling wave that propagates along the electrodes of the modulator. Only the optical beam travelling in the same direction as the microwave signal experiences phase modulation.

In the following, the operation of the BOM-PD will be explained and the shot noise limit and the phase detection sensitivity will be derived (after [99]). A schematic of the BOM-PD set-up can be seen in figure 4.1. The two outputs from the Sagnac interferometer of the BOM-PD can be written as: $P_1 = P_{\mathrm{avg}} \sin^2\left(\frac{\Delta\phi}{2}\right)$ and $P_2 = P_{\mathrm{avg}} \cos^2\left(\frac{\Delta\phi}{2}\right)$, where $\Delta\phi$ is the phase difference between counterpropagating pulses and P_{avg} is the total average output power of the interferometer. This relation is illustrated in figure 4.2. Taking the pulsed nature of the optical source into consideration, the powers

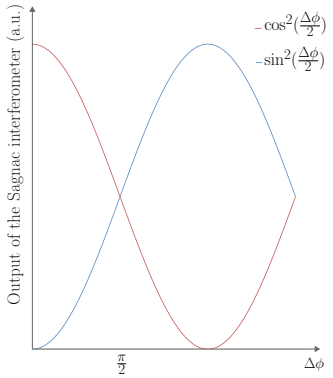

Figure 4.2: Dependence of the power of the two outputs of the Sagnac interferometer on the nonreciprocal phase shift between the counterpropagating beams.

can also be written as:

$$P_1(t) = \frac{P_{\text{avg}}}{m} \sum_{n=0}^{\infty} \delta(t - nT_r) \sin^2\left(\frac{\Delta\phi(t)}{2}\right) \tag{4.1}$$

$$P_2(t) = \frac{P_{\text{avg}}}{m} \sum_{n=0}^{\infty} \delta(t - nT_r) \cos^2\left(\frac{\Delta\phi(t)}{2}\right) \tag{4.2}$$

where T_r is the time between successive pulses, m is the number of pulses per second and $\Delta\phi(t)$ is the phase difference between the counterpropagating pulses.

As can be seen from figure 4.2, a phase difference of $\Delta\phi = \frac{\pi}{2}$ is required in order to operate the BOM-PD in the balanced condition. To obtain a phase difference between the counterpropagating beams, the symmetry of the Sagnac interferometer has to be broken because the phase modulator only supports unidirectional operation in the microwave region—a DC voltage supplied to the modulator would result in the same phase shift for both beams—and can therefore not be used for this purpose. In the BOM-PD the symmetry of the Sagnac interferometer is broken by a section consisting of two oppositely oriented 45° Faraday rotators and a quarter wave plate. While everywhere else in the Sagnac interferometer the counterpropagating beams have the same polarisation, between the two Faraday rotators the polarisations are orthogonal. This is illustrated in figure 4.3. By placing

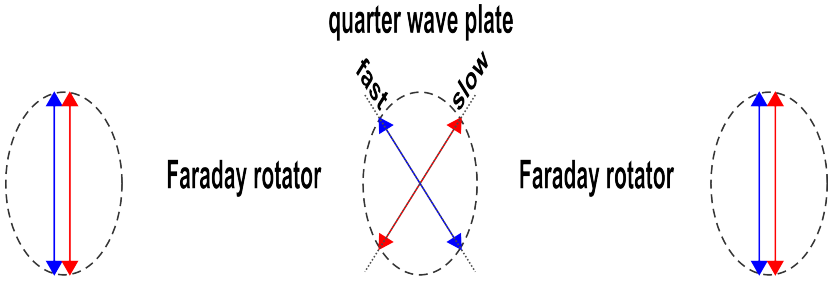

Figure 4.3: Diagram showing how the non-reciprocal phase shift of $\frac{\pi}{2}$ is obtained. The red and the blue arrows illustrate the polarisations of the counterpropagating beams. Due to the Faraday rotators, the polarisations are orthogonal at the quarter wave plate. Aligning the fast and slow wave plate axes with the polarisations of the beams therefore yields a non-reciprocal phase shift of $\frac{\pi}{2}$.

a quarter wave plate between the Faraday rotators, and aligning the slow and the fast axes of the waveplate with the polarisation axes of the counterpropagating beams, the required non-reciprocal phase shift of $\Delta\phi = \frac{\pi}{2}$ is obtained.

This intensity balanced condition of the BOM-PD is key to its working principle because balanced detection of the two outputs of the Sagnac interferometer can be used in order to suppress AM-PM conversion. For the correct operation of the BOM-PD in the balanced condition, the waveplate has to be correctly aligned with respect to the polarisation axes of the counterpropagating beams. In addition to that, different losses in the non-common paths of the two output arms of the interferometer (P_1 enters the balanced detector right after the 50/50 coupler while P_2 passes through the circulator before entering the balanced detector) have to be accounted for. Otherwise the BOM-PD is not operated in the balanced condition and the AM-PM suppression will degrade.

In order to phase lock the VCO to a harmonic of the repetition rate, an error signal is derived from the balanced detector by subtracting the average photocurrents. The time dependent phase difference between the counterpropagating beams can be written as

$$\Delta\phi(t) = \Phi_0 \sin\left(2\pi f_{\mathrm{VCO}} t + \theta_e\right) + \frac{\pi}{2} \tag{4.3}$$

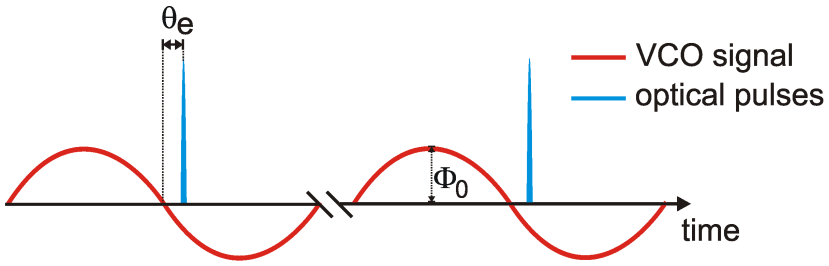

Figure 4.4: Illustration of the phase relation between the optical pulse train and the VCO microwave signal. θ_e is the phase error between the zero crossing of the microwave signal and the optical pulse train. Φ_0 is the amplitude of the phase modulation signal from the VCO.

where f_{VCO} is the frequency of the VCO, Φ_0 is the amplitude of the phase modulation signal from the VCO and θ_e is the phase error between the VCO signal and the optical pulse train as illustrated in figure 4.4. Substituting for $\Delta\phi(t)$ in equation 4.1 and 4.2 yields

$$P_1(t) = \frac{P_{\mathrm{avg}}}{m} \sum_{n=0}^{\infty} \delta(t - nT_r) \sin^2 \left[\frac{1}{2} \left(\Phi_0 \sin\left(2\pi f_{\mathrm{VCO}} t + \theta_e\right) + \frac{\pi}{2} \right) \right], \quad (4.4)$$

$$P_2(t) = \frac{P_{\mathrm{avg}}}{m} \sum_{n=0}^{\infty} \delta(t - nT_r) \cos^2 \left[\frac{1}{2} \left(\Phi_0 \sin\left(2\pi f_{\mathrm{VCO}} t + \theta_e\right) + \frac{\pi}{2} \right) \right]. \quad (4.5)$$

When the PLL is closed, the VCO frequency is given by a harmonic N of the repetition rate, i.e. $f_{\mathrm{VCO}} = N f_r$, and the average photocurrents can be written as

$$\langle I_1 \rangle = R P_{\mathrm{avg}} \sin^2 \left[\frac{1}{2} (\Phi_0 \sin\theta_e + \frac{\pi}{2}) \right], \quad (4.6)$$

$$\langle I_2 \rangle = R P_{\mathrm{avg}} \cos^2 \left[\frac{1}{2} (\Phi_0 \sin\theta_e + \frac{\pi}{2}) \right], \quad (4.7)$$

where R is the responsivity of the photodetector. The output current $\langle I_d \rangle$ from the balanced photodetector is

$$\langle I_d \rangle = \langle I_1 \rangle - \langle I_2 \rangle = -R P_{\mathrm{avg}} \cos\left[\Phi_0 \sin\theta_e + \frac{\pi}{2}\right] = R P_{\mathrm{avg}} \sin\left[\Phi_0 \sin\theta_e\right]. \quad (4.8)$$

For $\theta_e << 1$ this can be approximated as

$$\langle I_d \rangle \approx RP_{\text{avg}}\Phi_0\theta_e, \tag{4.9}$$

The error signal derived from the average photocurrents is therefore proportional to the phase error in the optical domain θ_e. The phase detection sensitivity K_d of the BOM-PD is given by

$$K_d = \frac{\langle I_d \rangle}{\theta_e} = RP_{\text{avg}}\Phi_0. \tag{4.10}$$

Any amplitude noise on the error signal will be converted into phase noise of the VCO signal within the locking bandwidth of the VCO. Sources for amplitude noise can be for example vibrations and acoustic noise in the interferometer and RIN of the comb that is not sufficiently suppressed by the BOM-PD due to operation away from the balanced condition. A fundamental noise limit is caused by shot noise in the photodetection (section 3.3.1). Using the phase detection sensitivity of the BOM, the shot noise induced SSB phase noise is given by

$$\mathscr{L}_{\text{shot}}(f) = \frac{1}{2}S_\phi^{\text{shot}}(f) = 10\log\left(\frac{1}{2}\frac{\overline{I_n^2}}{K_d^2}\right), \tag{4.11}$$

and using equation 3.4 and 4.10 this can be written as

$$\mathscr{L}_{\text{shot}}(f) = 10\log\left(\frac{1}{2}\frac{2eRP_{\text{avg}}}{(RP_{\text{avg}}\Phi_0)^2}\right) = 10\log\left(\frac{e}{RP_{\text{avg}}\Phi_0^2}\right). \tag{4.12}$$

Here the optical pulses are too long to make use of the shot-noise correlation discussed in the previous chapter. As in equation 3.4, the shot noise decreases with increasing optical power. In additional to that, the shot noise also decreases with increasing rf power of the VCO signal that drives the phase modulator:

$$\mathscr{L}_{\text{shot}}(f) \propto \frac{1}{P_{\text{avg}}\Phi_0^2}. \tag{4.13}$$

As a result, the shot noise floor of BOM-PDs can be lower than that achieved

with commercial photodiodes operated in the long-pulse regime.

4.2 Frequency comb used in this thesis

While the first frequency combs were based on Kerr-lens mode-locked femtosecond Ti:sapphire lasers, erbium-doped mode-locked fibre combs are increasingly being used due to their more robust and long term stable operation. In the following the 100 MHz Er:fibre frequency comb (FC1500 MenloSystems GmbH) used throughout this thesis is described. The comb is passively mode-locked using nonlinear polarisation rotation, which rotates the polarisation of intense light due to nonlinear effects such as self-phase modulation and cross-phase modulation, in combination with a polarising element in order to to create a power dependent transmission [100]. By tuning the polarisation of the laser, it is possible to generate conditions in which light with the highest intensity experiences the lowest loss. In this way, an artificial saturable absorber is generated which can be used to mode-lock the laser. For the self-referencing of the comb, the light is amplified by an EDFA and the optical spectrum is broadened by a highly nonlinear fibre to span an octave (1000–2100 nm). By controlling the power of the pump laser, f_0 is locked to a 20 MHz signal derived from a hydrogen maser. This is possible since the group and the phase velocity depend differently on the intensity of the circulating pulse inside the cavity [41]. The repetition rate is locked by comparing its $10th$ harmonic to a 1 GHz signal derived from the hydrogen maser and controlling the cavity length of the laser using a piezo-actuated mirror. The optical pulses directly from the comb are shorter than 150 fs. Due to dispersion in the optical fibres, the pulses are usually broadened to hundreds of ps by the time they reach the experiments carried out in this thesis. Usually the light was further amplified by an EDFA prior to the experiment which restricts the optical bandwidth to approximately 30 nm centred around 1550 nm.

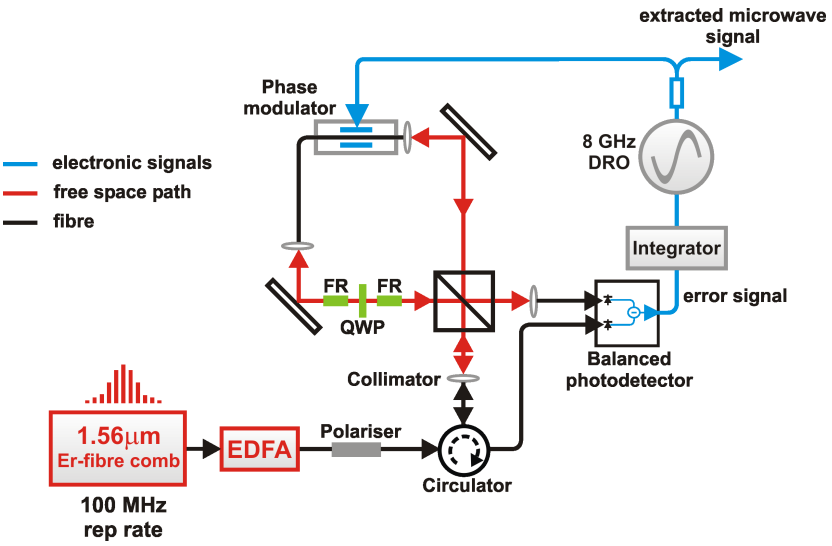

Figure 4.5: Schematic of the mainly free-space BOM-PD set-up. EDFA: erbium-doped fibre amplifier; FR: Faraday rotator; QWP: quarter waveplate; DRO: dielectric-resonator oscillator. All fibres after the polariser are polarisation maintaining.

4.3 Free-space balanced optical-microwave phase detector

4.3.1 Experimental set-up

In this section, low-noise optical-to-electrical conversion is presented using mainly free-space BOM-PDs. The Sagnac interferometer consists of free-space optics but the working principle is the same as described in section 4.1. This free-space approach has the advantage that free-space optic components are significantly cheaper than PM fibre components.

A schematic of the experimental set-up can be seen in figure 4.5. The BOM-PD synchronizes an 8 GHz dielectric-resonator oscillator (DRO) to the $80th$ harmonic of the 100 MHz Er:fibre comb. Light from the comb is amplified by an erbium-doped fibre amplifier (EDFA) and linearly polarised using an in-line fibre polariser before it enters the Sagnac interferometer via a polarisation maintaining (PM) circulator and a collimator. At the input to the interferometer the average power of the pulse train (wavelength

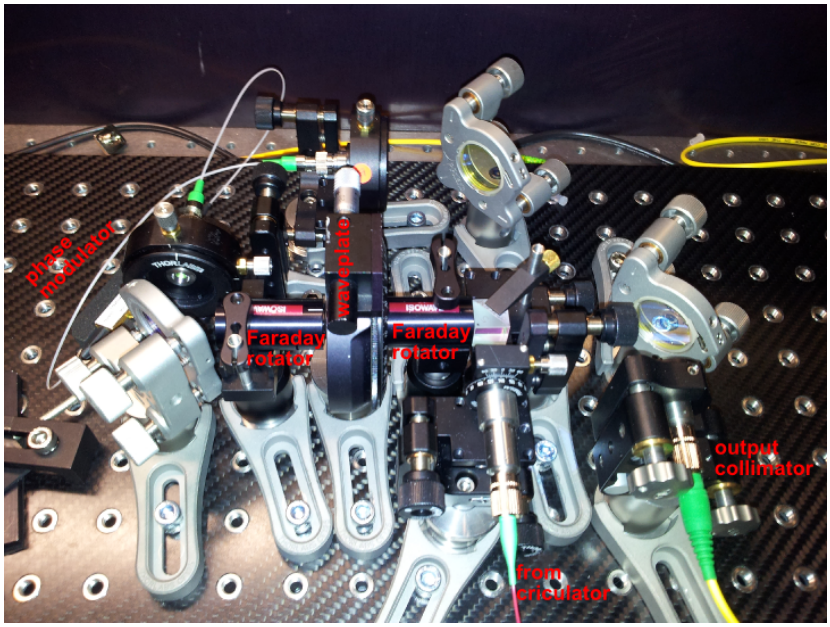

Figure 4.6: Photograph of the free-space Sagnac interferometer of the BOM-PD set-up.

range 1530 nm–1560 nm) is approximately 14 mW. A nonpolarising beam-splitter is used to split the incoming light into two counterpropagating beams with equal intensities. The DRO signal is split into two; one signal is used for the phase noise characterisation and the other drives the unidirectional travelling-wave phase modulator. When the PLL is closed, the DRO frequency is locked to the $80th$ harmonic of f_r and the optical pulses coincide with the zero crossings of the DRO signal. A picture of the free-space Sagnac interferometer of the BOM-PD set-up can be seen in figure 4.6.

4.3.2 Experimental results and discussion

A series of measurements was carried out to determine the residual phase noise of the optical-to-electrical conversion using the free-space BOM-PD. At first, one free-space BOM-PD was compared with a high speed photodiode. Before that measurement was carried out, the residual phase noise of the optical-to-electrical conversion of these photodiodes (DSC40S Discovery Semiconductors Inc.) was determined. For this purpose, two microwave

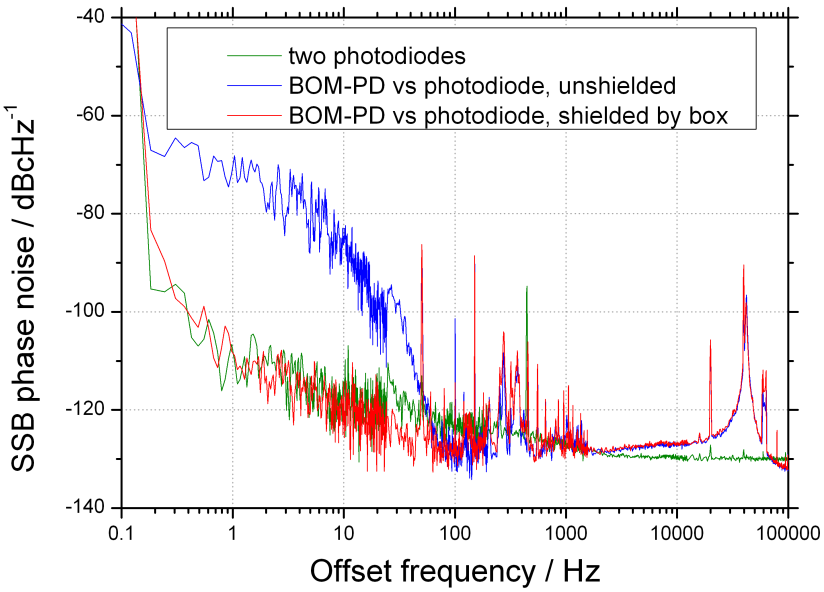

Figure 4.7: Residual SSB phase noise of the extracted microwave signals using a BOM-PD and photodiodes. Green: two photodiodes (DSC40S); blue: Photodiode and BOM-PD, unshielded; red: Photodiode and BOM-PD, shielded by box.

signals at 8 GHz were generated from a common fibre comb using two photodiodes. The phase noise was measured using a saturated double balanced mixer (DBM) (M8-0412, Marki Microwave, Inc.) which was fed by the two microwave signals in quadrature ($\pi/2$ out of phase). The output voltage was analysed by a fast Fourier transform analyser to yield the phase noise. In order to saturate the mixer the 8 GHz signals from the saturated photodiodes had to be amplified by approximately 40 dB by a series of low-noise rf amplifiers. The white and flicker noise contribution of the rf amplifiers limited the phase noise of the 8 GHz signals to approximately $-110\,\mathrm{dBc\,Hz^{-1}}$ at 1 Hz and $-130\,\mathrm{dBc\,Hz^{-1}}$ at 10 kHz. The green line in figure 4.7 shows the phase noise for two systems. The performance of the free-space BOM-PD was then compared with that of the high speed photodiode. Due to the relatively high output power of the DRO (11 dBm) no rf amplification is needed for this system. This is one advantage of the BOM-PD scheme, because it avoids phase noise degradation by rf amplification. The first phase noise measurement can be seen in the blue curve of figure 4.7. The additional

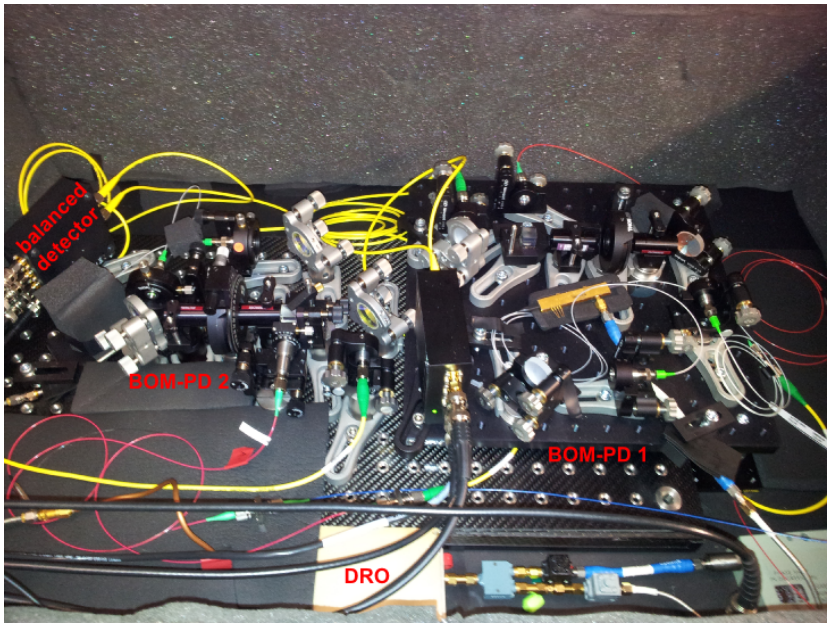

Figure 4.8: Photograph of the two free-space BOM-PD set-ups placed inside an acoustic isolation box.

noise at offset frequencies below 70 Hz is caused by air fluctuations. As a result, the phase noise at 1 Hz is 40 dB higher than that of the photodiode. Between 100 Hz and 1 kHz acoustic noise features are present. The peak in the region of 40 kHz is caused by the locking bandwidth of the PLL. In order to reduce the excess phase noise at low offset frequencies, the free-space Sagnac interferometer was shielded from air fluctuations by a box, made out of thermal insulation styrofoam. As can be seen from the red line in figure 4.7 this successfully eliminated the excess noise, and the phase noise at low offset frequencies was limited by the signal from the photodiode.

To overcome this limitation, a second, nominally identical free-space BOM-PD was built for comparison. The free-space optics of both BOM-PDs were mounted on smaller mounts in order to reduce vibrations and the two set-ups were placed inside an acoustic isolation box (wooden box with acoustic isolation sheets attached to inside walls) in order to reduce vibrations and acoustic noise. The experimental set-up can be seen in figure 4.8. Both BOM-PDs were synchronised to the $80th$ harmonic of the fibre

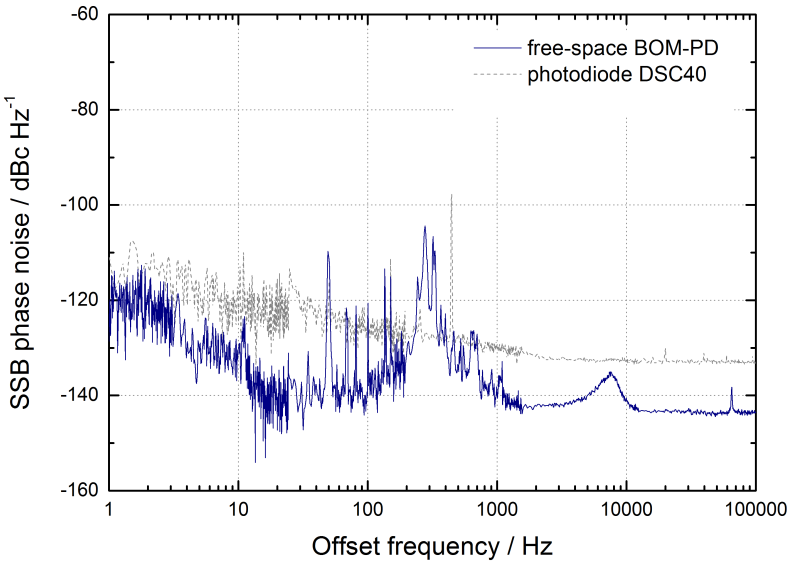

Figure 4.9: Residual single-sideband (SSB) phase noise of the extracted 8 GHz microwave signals using the BOM-PD (solid blue) and direct photodetection (dashed grey). To estimate the contribution from a single system, 3 dB has been subtracted from the measured phase noise.

comb and an out of loop comparison between the two 8 GHz signals was performed using a mixer. In figure 4.9, the residual phase noise of the free-space BOM-PD and, for comparison, that of a single photodiode (DSC40S) are shown. In order to represent the phase noise contribution of a single set-up, 3 dB was subtracted from the measured phase noise, assuming equal noise contributions from the two set-ups. The phase noise of the BOM-PD is better than that of the commercial photodiode and only approximately 10 dB worse than that of a state-of-the-art fibre BOM-PD [101]. At high offset frequencies the improvement compared to the photodiode is 10 dB and at 30 Hz the improvement is 20 dB. This is the first time that such low phase noise levels have been achieved with a free-space BOM-PD and, as can be seen in table 4.1, they represent a significant improvement compared to the free-space BOM-PD results reported by Kim *et al.* [96] which were limited by the AM-PM conversion in the photodiode against which the BOM-PD was compared.

	$\mathscr{L}(f)(\mathrm{dBc\,Hz^{-1}})$	
Device	$f = 1\,\mathrm{Hz}$	$f = 20\,\mathrm{kHz}$
Photodiode (DSC40S)	−110	−133
free-space BOM-PD by Kim [96]	−43	−108
free-space BOM-PD (this work)	−119	−143

Table 4.1: Comparison of free-space BOM-PD set-ups. The results from [96], are up-shifted by 12 dB due to the frequency ratio of 4 between the 2 GHz VCO in their work and the 8 GHz DRO used here. For comparison the phase noise achieved with a photodiode is also shown.

It was not possible to entirely suppress the vibrations and acoustic noise contribution in the region between 0.1 kHz to 1 kHz. Another limitation of the free-space BOM-PD is the limited power that is available at the photodetector due to coupling losses between free-space and fibre paths of the set-up. The optical power available on each photodiode was approximately 200 µW. In order to avoid these limitations, a mainly fibre-based system can be used, which will be referred to as fibre BOM-PD in the following. In the next section, the residual optical-to-electrical conversion of these fibre BOM-PDs will be presented.

The phase noise of the free-space BOM-PD was furthermore also limited by AM-PM conversion. When the DRO signal was disconnected from the phase modulator, the residual AM-fluctuations of the error signal converted into phase fluctuations using K_d, were at the same level as the phase noise measurements. As will be described in the next section, the problem of AM-PM conversion in BOM-PDs was solved by making improvements to the fibre BOM-PD set-up.

4.4 Fibre-based balanced optical-microwave phase detector

This section describes the development of BOM-PDs that consist mainly of fibre components which are used for low-noise optical-to-electrical conver-

Device	α (rad)	$20\log(\alpha)$ (dB)
Photodiode	2	+6
	0.1	−20
BOM-PD	0.3	−11
	0.06	−24

Table 4.2: AM-PM conversion coefficients in commercial photodiodes and BOM-PDs [97] and the corresponding phase noise contribution below the RIN of the laser source (calculated via equation 3.8).

sion. Two key changes to the fibre BOM-PD set-up from Jung [101] are presented which resulted in an improved AM-PM suppression of 60 dB and made it possible to reach close to state-of-the-art residual phase noise despite using a commercial fibre comb with relatively high RIN.

4.4.1 AM-PM conversion and RIN

AM-PM conversion coefficient in BOM-PDs

One key feature of the BOM-PD is the suppression of excess phase noise caused by AM-PM conversion in the photodetection process. As described in section 4.1, this is achieved by detecting the phase error between the VCO signal and the optical pulse train in the optical domain. However, prior to the work presented here, it had not been shown that BOM-PDs could efficiently suppress AM-PM conversion. Jung *et al.* reported an AM-PM conversion coefficient (α) of 0.06 rad to 0.3 rad in their BOM-PD, depending on the offset frequency [97]; this is similar to the α in saturated photodiodes which is typically between 0.1 rad and 2 rad. As can be seen in table 4.2, such AM-PM conversion coefficients correspond to an AM-PM induced phase noise below the SSB RIN of the comb of approximately 11 dB at 3 Hz and 24 dB at 5 kHz. When a commercial frequency comb with a relatively high RIN is used, such a high AM-PM conversion coefficient is not suitable for ultra-low noise microwave generation.

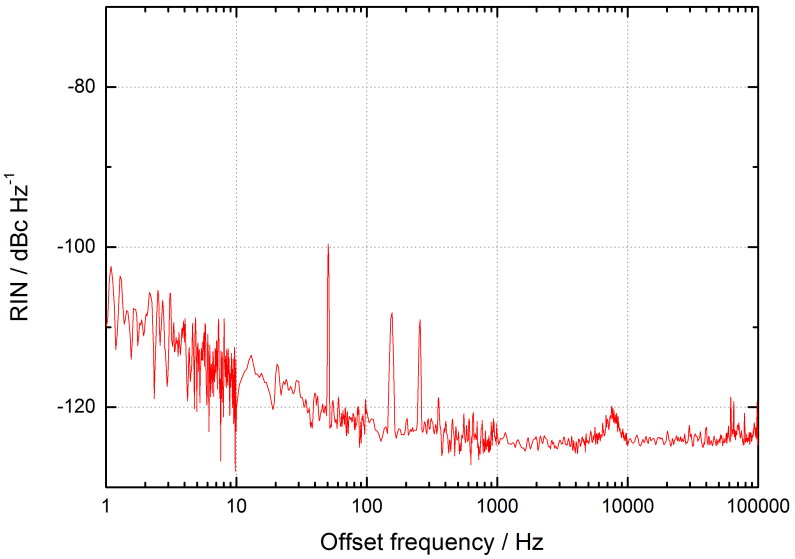

Figure 4.10: Relative intensity noise of the fibre comb (FC 1500, Menlo Systems GmbH) used in this work.

RIN of a commercial fibre comb

In figure 4.10, the RIN of the commercial Er:fibre comb (FC 1500, Menlo Systems GmbH) used in this work is shown. As can be seen in table 4.3, the RIN of the commercial fibre comb combined with the AM-PM coefficients reported by Jung *et al.* would limit the phase noise to approximately $-117\,\mathrm{dBc\,Hz^{-1}}$ at 1 Hz and $-148\,\mathrm{dBc\,Hz^{-1}}$ at 10 kHz. By using a specially designed Er:fibre laser [102] with a RIN approximately 17 dB lower than that of the commercial fibre comb used here [103], Jung *et al.* [101] were able to demonstrate state-of-the-art optical-to-electrical conversion in BOM-PDs of $-133\,\mathrm{dBc\,Hz^{-1}}$ at 1 Hz and $-154\,\mathrm{dBc\,Hz^{-1}}$ at 1 kHz despite the relatively poor AM-PM conversion in their BOM-PD.

It should also be noted that the EDFA used in this work significantly degraded the RIN of the comb when it was not operated in saturation. The power available from the commercial fibre comb for this experiment was approximately 154 µW which made amplification necessary. As can be seen in figure 4.11, depending on the drive current of the EDFA pump diode, this

Offset frequency	RIN(f)(dBc Hz^{-1})	α (rad)	$\mathscr{L}_{\mathrm{RIN}}(f)$(dBc Hz^{-1})
1 Hz	−106	0.3	−117
5 kHz	−123	0.06	−147

Table 4.3: The phase noise contribution of the RIN of the commercial fibre comb is calculated using the AM-PM conversion coefficient from Jung *et al.* [97].

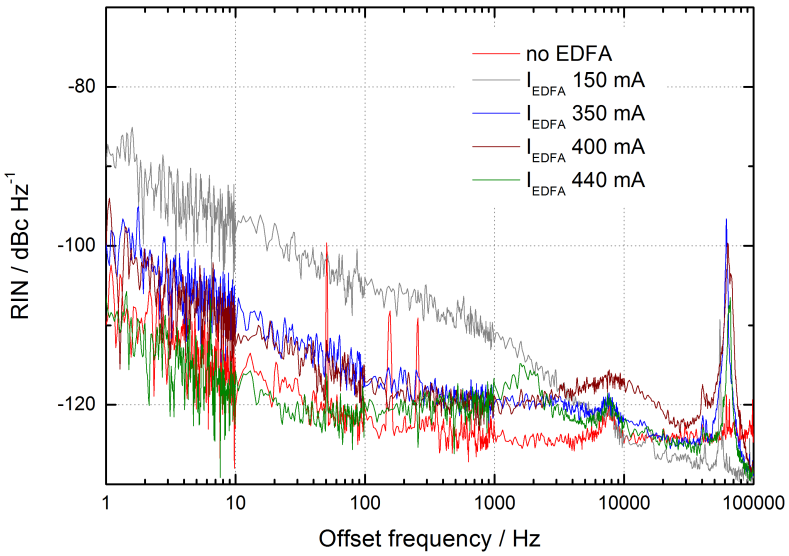

Figure 4.11: RIN contribution of the EDFA for different driving currents.The power incident on the photodiode was 800 µW for all measurements.

significantly degraded the RIN of the comb. The threshold of the EDFA (Keopsys) is at 75 mA. For a current of 150 mA the RIN at low offset frequencies is increased by 18 dB. For higher currents the increase is less; at 400 mA the increase in the RIN is approximately 8 dB. For the maximum driving current of 440 mA the RIN is not degraded by the EDFA for offset frequencies below 100 Hz. However, as the EDFA saturates there are several noise features at high offset frequencies which degrade the RIN. In this work, the EDFA was operated in saturation (440 mA) in order to avoid degradation of the RIN of the comb at low offset frequencies.

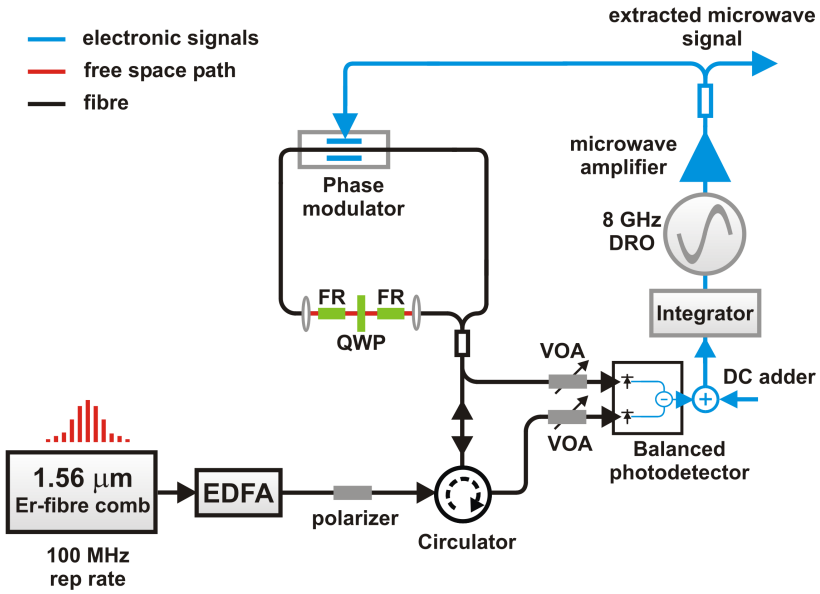

Figure 4.12: Schematic of the improved fibre BOM-PD set-up. EDFA: erbium-doped fibre amplifier; FR: Faraday rotator; QWP: quarter waveplate; DRO: dielectric-resonator oscillator; VOA: variable optical attenuator. All fibres after the polariser are polarisation maintaining. Taken from [98].

4.4.2 Experimental set-up

In the following two sections, a modified BOM-PD design with a significantly improved AM-PM conversion coefficient of 0.001 rad is presented. A schematic of the BOM-PD is shown in figure 4.12. The working principle is the same as described in section 4.1. The BOM-PD synchronises an 8 GHz dielectric-resonator oscillator (DRO) to the $80th$ harmonic of the 100 MHz repetition rate of the Er:fibre comb. In order to achieve a high AM-PM suppression, two key changes to the BOM-PD set-up from Jung and Kim were made. Firstly, variable optical attenuators (VOAs) were introduced at each output of the Sagnac interferometer. These compensate for the loss in the optical circulator and hence ensure that the balanced intensity condition is met, which is crucial for effective suppression of AM-PM conversion. Secondly, a DC voltage is added to the error signal to compensate for unwanted offsets in the loop filter electronics which would also result in operation of the BOM-PD away from the balanced condition. The idea to add the DC

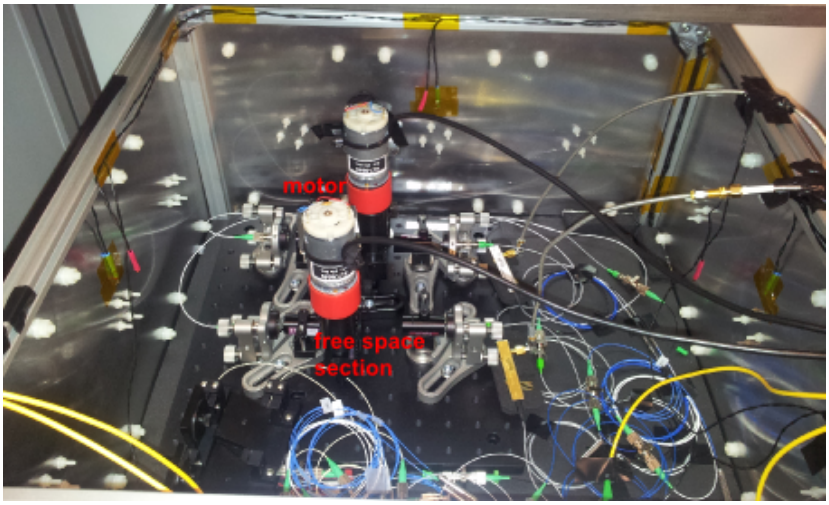

Figure 4.13: Photograph of the experimental set-up. The BOM-PD set-ups are placed inside a thin (2 mm) aluminium box. For the phase noise and AM-PM suppression measurements the temperature was not stabilised. The waveplates were fine-tuned using the motors seen in the photograph.

voltage came from Giuseppe Marra. Since only fairly coarse adjustments could be made using the VOAs, this DC voltage was also used to fine tune the balanced condition. In order to measure the residual phase noise of the extracted microwave signal, two nominally identical BOM-PDs were built. A photograph of the experimental set-up can be seen in figure 4.13. In figure 4.14, a schematic of the measurement set-up is shown. BOM-PD1 is locked to the $80th$ harmonic of the comb repetition rate while BOM-PD2 is used as an ultra-sensitive phase detector fed with the 8 GHz signal from BOM-PD1. The phase sensitivity of BOM-PD2 is measured using a calibrated phase shifter.

4.4.3 Experimental results and discussion

Optical-to-electrical conversion

As can be seen in figure 4.15, the residual phase noise of the BOM-PD is $-131\,\mathrm{dBc\,Hz^{-1}}$ at 1 Hz and $-148\,\mathrm{dBc\,Hz^{-1}}$ at 1 kHz. This is only slightly worse (by 2 dB at 1 Hz and 6 dB at 5 kHz) than the state-of-the-art BOM-PD

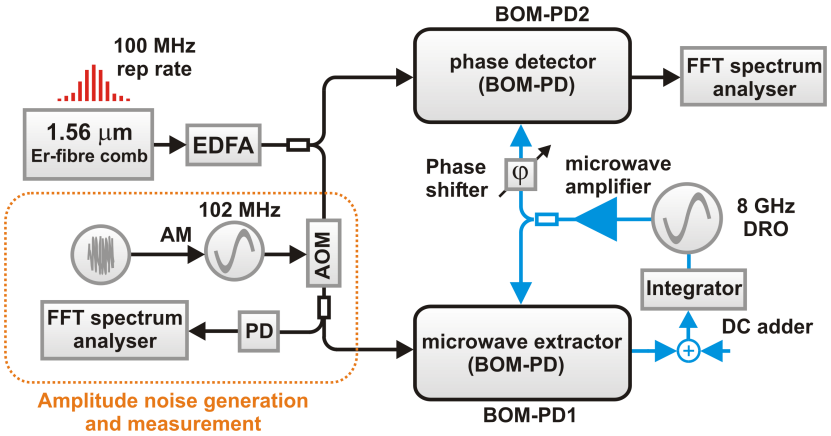

Figure 4.14: Schematic of phase noise and AM-PM conversion measurement set-up. EDFA: erbium-doped fibre amplifier; AOM: acousto-optic modulator; PD: photodiode; DRO: dielectric-resonator oscillator, BOM-PD: balanced optical-microwave phase detector. Taken from [98].

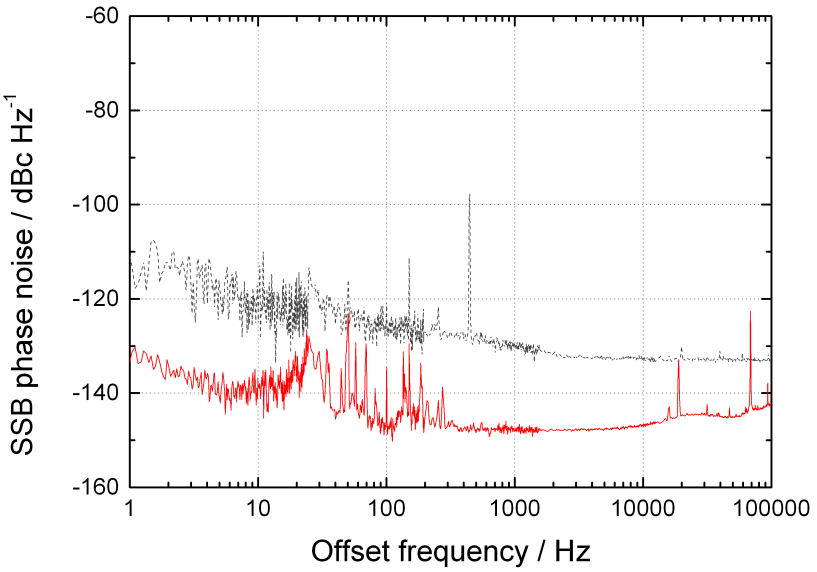

Figure 4.15: Residual phase noise results. Solid red: BOM-PD. Dashed grey: typical photodiode performance, shown for comparison. To estimate the contribution from a single system, 3 dB has been subtracted from the measured phase noise. Taken from [98].

	$\mathscr{L}(f)(\mathrm{dBc\,Hz^{-1}})$	
Device	$f = 1\,\mathrm{Hz}$	$f = 5\,\mathrm{kHz}$
fibre BOM-PD by Kim [101]	−133	−154
improved fibre BOM-PD (this work)	−131	−148

Table 4.4: Comparison with state-of-the-art BOM-PD set-up [101].

performance [101], even though the RIN of the comb used here was approximately 17 dB [103] higher than the specially designed Er-fibre laser [102] used in [101]. Furthermore, the optical power incident on each photodiode is 400 µW, which is an increase of a factor of two compared to the free-space BOM-PD, but almost an order of magnitude below the BOM-PD used by Jung *et al.* [97]. The rf power applied to each phase modulator is approximately 16 dBm, which yields a phase-to-voltage conversion coefficient of $K_d = 30\,\mathrm{rad\,V^{-1}}$ and a shot noise level of $-154\,\mathrm{dBc\,Hz^{-1}}$. The excess noise in the region between 10 Hz and 300 Hz is attributed to vibrations of the waveplate mount, whilst below 10 Hz it is attributed to the flicker noise of the balanced photodiodes [104]. The locking bandwidth of the PLL was limited to several hundred kHz due to the loop filter available at the time of the experiment. With an improved loop filter design the phase noise at high offset frequencies is expected to approach the shot noise limit, which in turn could be further reduced by increasing the optical power. By re-designing the loop filter with a modified transfer function so that the frequency roll-off of the DRO control voltage can be partially compensated and by using higher bandwidth operational amplifiers, an increased locking bandwidth could be achieved. However, the main purpose of this experiment was to demonstrate the highest possible level of AM-to-PM suppression. Since the phase detector BOMPD2 was unlocked in these measurements, it was not possible to fine-tune the AM-PM suppression in this system using the DC adder, and there was still some residual AM-PM conversion present. This issue could be resolved in future experiments either by locking both BOM-PDs and comparing them using a carrier suppression phase noise measurement system [105] or by using a fully optimized opto-mechanical design for the

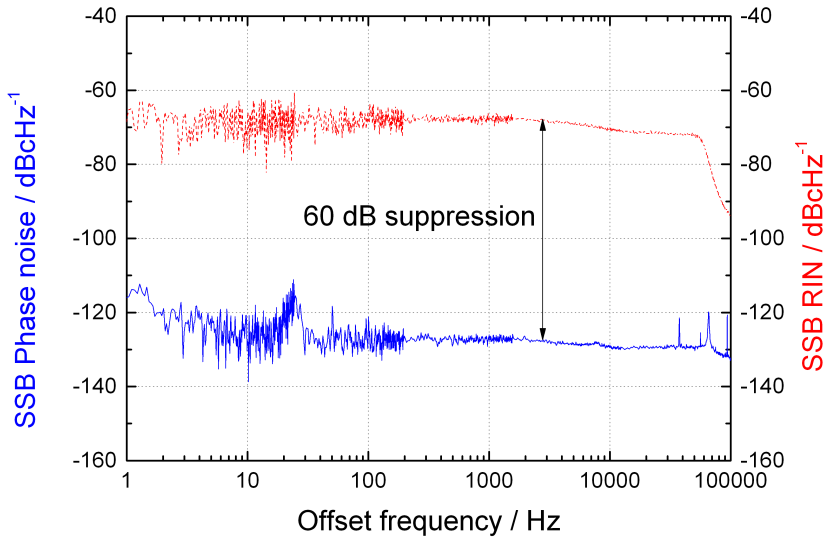

Figure 4.16: AM-PM suppression results. Dashed red: RIN of modulated laser signal; solid blue: phase noise measured by phase detector BOM-PD2. Taken from [98].

VOA mounts.

Improved AM-PM suppression

The set-up for the AM-PM conversion measurement is shown in figure 4.14. The light that enters BOMPD1 is amplitude modulated with white noise up to a frequency of 50 kHz by an AOM. The RIN of the modulated laser signal is measured with a photodiode and then compared with its contribution to the phase noise of the generated 8 GHz microwave signal which is measured by BOM-PD2. As can be seen in figure 4.16, an AM-PM suppression of 60 dB is achieved. Of this, around 37 dB is achieved using the VOAs, whilst the remaining 23 dB is obtained from the fine-tuning of the DC voltage. The level of suppression was measured for a range of input optical powers up to the maximum available and no degradation was observed. At lower offset frequencies and at offset frequencies above 50 kHz the suppression is limited by the residual noise of BOM-PD2 which is used to measure the phase noise of BOM-PD1. From these results, α can be calculated using equation 3.8. As illustrated in figure 4.17, an AM-PM conversion coefficient

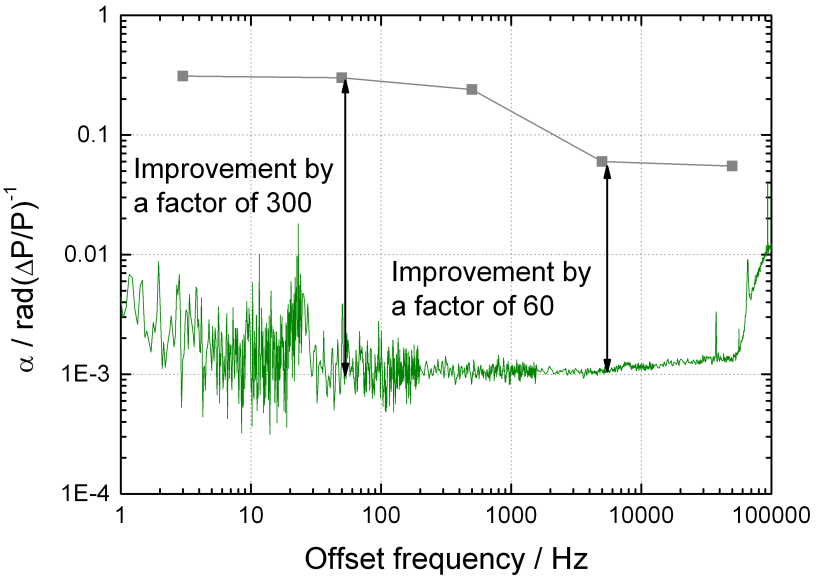

Figure 4.17: AM-PM conversion coefficient. Solid green: calculated AM-PM conversion coefficient; grey squares: AM-PM conversion coefficient from Jung and Kim [97]. Taken from [98].

of $\alpha = 0.001\,\mathrm{rad}$ is achieved which corresponds to an improvement by a factor of approximately 60–300 compared to the results from Jung *et al.* [97]. As expected, α is constant over the range of offset frequencies for which the measurement is not limited by the background noise of the phase noise measurement system. This is in contrast to the frequency-dependent α reported in [97].

Figure 4.18 shows a series of measurements of the long term stability of the AM-PM suppression level. The red dashed line is the RIN of the AOM-amplitude modulated comb, the dashed blue line shows the phase noise floor of BOM-PD2 and the black line shows the initial phase noise measurement after the balanced condition was optimised by fine-tuning of the DC voltage. The green, dark yellow and grey line are phase noise measurements after 6, 46 and 91 hours respectively. The corresponding AM-PM suppression for these measurements and some additional measurements, not shown in figure 4.18, can be seen in table 4.5. After initial optimisation of the balanced condition, the highest suppression is 68 dB; a suppression of more than 60 dB

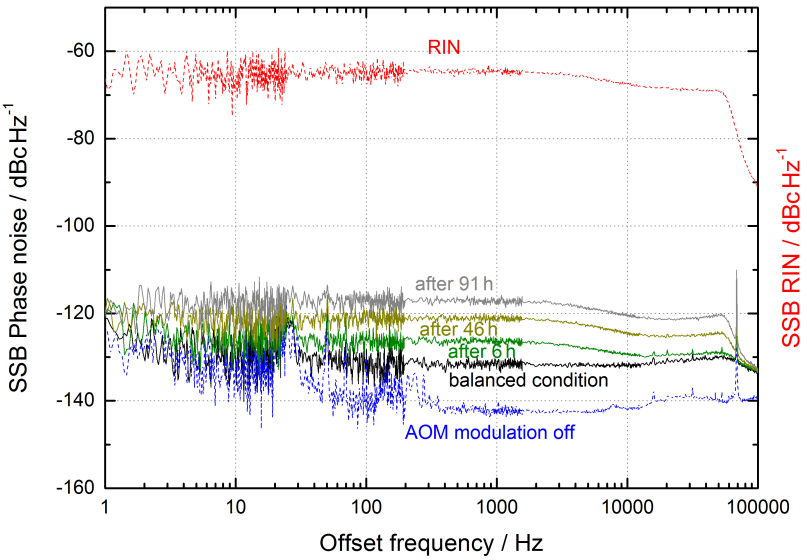

Figure 4.18: Long term stability of the AM-PM suppression. Dashed red: RIN of modulated laser signal; dashed blue: Noise floor of BOM-PD2 (AOM modulation off); black: Phase noise after initial balancing; green: Phase noise after 6 h; dark yellow: Phase noise after 46 h; grey: Phase noise after 91 h.

Elapsed time (h)	AM-PM suppression (dB)
0	68
6	66
20	62
27	61
46	57
91	53

Table 4.5: Long term stability of the AM-PM suppression.

is achieved for up to 27 h and after more than 3.5 days the suppression is still 53 dB. This level of suppression is achieved without any retuning or active stabilisation.

A measurement of the sensitivity of the AM-PM suppression with respect to the applied DC voltage can be seen in figure 4.19. A change of 3 mV in the bias voltage resulted in a reduction of the suppression by 6 dB and a change of 23 mV resulted in a reduction of 13 dB respectively. For even higher bias

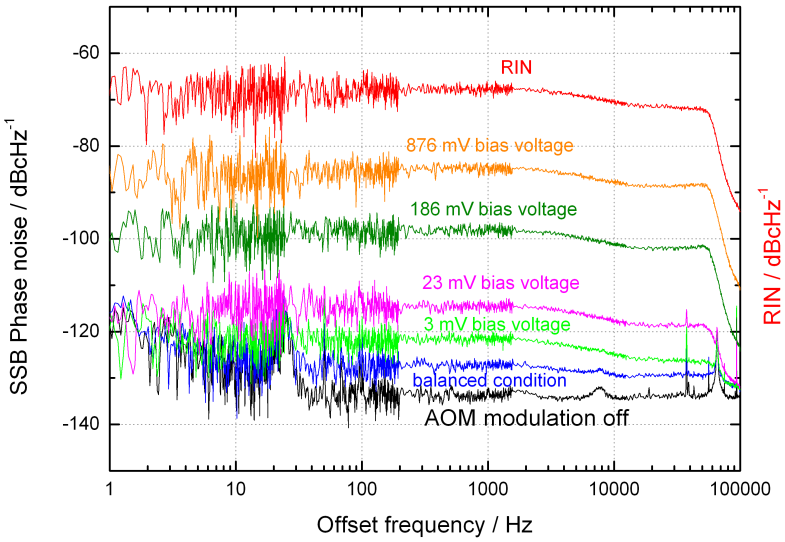

Figure 4.19: Dependence of the AM-PM suppression on the DC voltage. Red: RIN of modulated laser signal; black: Noise floor of BOM-PD2 (AOM modulation off); blue: Phase noise for DC voltage of 0 mV; green: Phase noise for DC voltage of 3 mV; magenta: Phase noise for DC voltage of 23 mV; olive: Phase noise for DC voltage of 186 mV; orange: Phase noise for DC voltage of 876 mV.

voltages the suppression is further reduced.

4.5 Conclusions and summary

In this chapter, the phase noise of the optical-to-electrical conversion using both free-space BOM-PDs and fibre BOM-PDs has been presented. The residual phase noise of the free-space BOM-PD was $-119\,\mathrm{dBc\,Hz^{-1}}$ at 1 Hz and $-143\,\mathrm{dBc\,Hz^{-1}}$ at 20 kHz from an 8 GHz carrier, which is the lowest phase noise ever reported for a free-space BOM-PD.

An improved fibre BOM-PD with an AM-PM conversion coefficient of 0.001 rad has been presented. This corresponds to an AM-PM induced phase noise 60 dB below the SSB RIN of a frequency comb. By using frequency combs with optimized RIN, this opens up the route to make the phase noise contribution of the RIN in the photonic microwave generation negligible. For

example, for the laser used by Zhang et al. [89], the contribution would be below $-190\,\mathrm{dBc\,Hz^{-1}}$ between 1 Hz and 1 MHz which is significantly lower than other major noise contributions such as flicker noise from the photodiode and thermal and shot noise contributions. This work was published in Optics Express [98].

Despite using a commercial fibre comb with a relatively high RIN, this high AM-PM suppression enabled close to state-of-the-art optical-to-electrical conversion in fibre BOM-PDs with a residual phase noise of $-131\,\mathrm{dBc\,Hz^{-1}}$ at 1 Hz and -148 Hz at 20 kHz from an 8 GHz carrier. This performance is up to 20 dB better than that achieved by direct photodetection (DSC40) and subsequent amplification of the microwave signal. At low offset frequencies the performance is comparable to the best optical-to-electrical conversion reported to date (see figure 3.4).

5 Time and frequency dissemination via fibre links

The use of fibre-based time and frequency transfer techniques is attractive for a number of reasons. Firstly, in many countries there is an existing infrastructure of fibre networks used for telecommunication which could also be used for clock-comparisons. Secondly, due to the low loss in fibre, which is approximately $0.2\,\mathrm{dB\,km^{-1}}$ at 1550 nm, and the availability of optical amplifiers, time and frequency transfer over thousands of km is possible. Finally, optical frequency combs provide the means for transferring the stability of optical frequency standards to the spectral region used in fibre communications.

As described in section 1.3, the only way to compare state-of-the-art optical clocks with estimated fractional frequency inaccuracies of a few parts in 10^{18} [3, 4, 5] is to use optical fibre-based frequency transfer techniques on a continental scale. As shown in figure 1.2, optical carrier frequency transfer experiments over 920 km and 1840 km long fibre link have produced noise floors below a fractional frequency instability of 10^{-18} [19, 20]. In this chapter several different frequency transfer methods will be discussed.

While normal GPS satellite receivers can be used for time transfer with an uncertainty of approximately 5 ns [106], two-way satellite time and frequency transfer techniques offer a time transfer accuracy at the 1 ns level [107]. However, optical fibre-based time transfer techniques, which will be discussed in this chapter, have accuracies of tens of ps over longer fibre links [108, 109]. Many applications such as radio telescopes (e.g. the Square Kilometer Array)

or the International Atomic Time scale, which is realised from a weighted average over 400 individual atomic clocks, could benefit from their superior performance.

5.1 Round-trip phase noise cancellation technique

The aim of time and frequency fibre transfer techniques is to reproduce a local timing or frequency reference at a remote site and minimise the degradation of the reference due to environmental perturbations. In the following, the concept of the round-trip phase noise cancellation method, which is used in most time and frequency transfer systems, will be presented. Optical path length fluctuations caused by mechanical perturbations and temperature variations in the fibre can perturb the phase of the transmitted signal. A bidirectional fibre link is employed in order to monitor and compensate for the fluctuations. In time transfer, optical path length fluctuations lead to timing errors while in frequency transfer they lead to Doppler shifts of the transmitted frequency.

Figure 5.1 illustrates the working principle of this method. A frequency reference is transmitted to the user end by an intensity modulated cw laser, the optical carrier itself or an optical frequency comb. Due to mechanical noise and temperature fluctuations, the phase of the signal at the user end is perturbed by $\Delta\varphi_\mathrm{f}$. A partial reflector sends some light back to the transmitter end, where interference between the local and the returned light yields the total phase error $\Delta\varphi_\mathrm{f} + \Delta\varphi_\mathrm{b}$, accumulated during the forward and the backward propagation through the fibre. As discussed in [110], three assumptions are necessary for the phase noise cancellation of the fibre. Firstly, the noise processes in the fibre are assumed stationary between the forward and the backward transmission through the fibre, and it is also assumed that the light samples the same polarisation modes along the fibre in both directions. Under this assumption, the fibre link is reciprocal for Fourier frequencies below $\frac{1}{T_\mathrm{rt}}$, where T_rt is the round-trip delay of the fibre. Therefore,

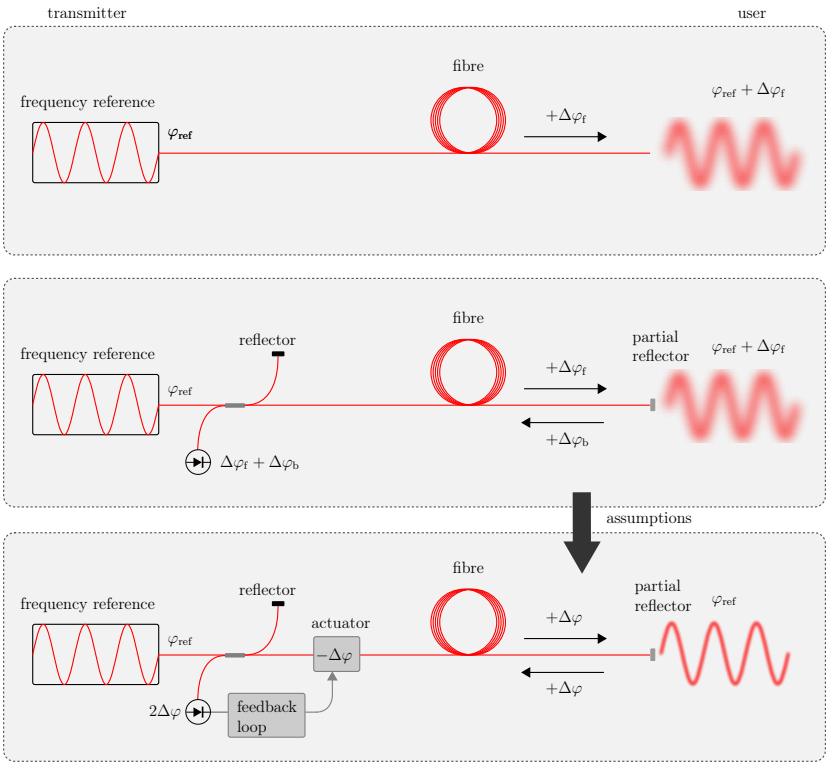

Figure 5.1: This schematic illustrates the round-trip phase noise cancellation technique. The transmitted frequency reference can be either an intensity modulated cw laser, an optical carrier or an optical frequency comb. Under the assumptions described in the text, the phase noise of the forward and backward directions are equal: $\Delta\varphi_f = \Delta\varphi_b$ and they can be written as $\Delta\varphi$; an actuator can be used to pre-compensate for the noise of the link, reproducing the reference signal at the user end.

the light experiences the same phase fluctuations in both directions through the fibre, which can be written as $\Delta\varphi_f = \Delta\varphi_b = \Delta\varphi$. In a real system, polarisation mode dispersion will cause the light to experience slightly different polarisation modes on the two directions through the fibre which can pose a limit to the transfer performance. Secondly, the bandwidth of the actuator that is used to pre-compensate for the fluctuations of the fibre must be lower than $\frac{1}{T_{rt}}$, because noise processes which occur at shorter time-scales than the round-trip delay cannot be cancelled. Finally, the coherence time of the transmitted frequency standard is assumed to be larger than T_{rt}, so that comparing the local reference with the delayed return signal does not

produce self-heterodyne noise. If all these assumptions are met, an actuator can be used to pre-compensate for the fibre noise, up to the round-trip limited frequency $\frac{1}{T_{\mathrm{rt}}}$,reproducing the reference at the user end.

The choice of actuator and its dynamic range depends on the transfer technique at hand and the length of the fibre link. In time transfer, frequency comb transfer and group velocity dependent rf or microwave frequency transfer, it is necessary to stabilise the optical path length of the link. Actuators that control the group delay include piezo-actuated fibre stretchers (small dynamic range), optical delay-lines and temperature-controlled fibre spools (larger dynamic range). The temperature-induced mechanical length variation of fibre is negligible compared to temperature-induced changes in the refractive index; hence optical path length fluctuations can be approximated as

$$\frac{\mathrm{d}\,(nL)}{\mathrm{d}T} \approx L\frac{\mathrm{d}\,n}{\mathrm{d}T}, \tag{5.1}$$

where nL is the optical path in the fibre and T is the temperature. In standard single-mode optical fibre, e.g. SMF-28, the temperature sensitivity of the refractive index is approximately $1 \times 10^{-5}\,\mathrm{K}^{-1}$, which corresponds to a time delay temperature coefficient of approximately $37\,\mathrm{ps\,km^{-1}\,K^{-1}}$. For long fibre links, temperature changes can therefore lead to significant path length fluctuations; for example, a temperature change of 1 K on a 1000 km fibre link leads to an optical path length change of 10 m, which corresponds to a time delay change of 37 ns. While for shorter fibre links fibre-stretchers, delay lines and temperature-controlled fibre spools are employed to compensate for temperature-induced path length variations, on longer links, seasonal temperature changes usually require path-length adjustment using fibre patchcords. In contrast, the absolute delay of the fibre link is not relevant in optical carrier frequency transfer, and the optical path length of the fibre is not directly stabilised. It is more convenient to compensate for path length variation induced Doppler shifts by adjusting the frequency of the transmitted laser signal using an AOM. Since the AOM acts on the optical frequency, rather than the phase, it offers extremely large dynamic

range for phase compensation. The Doppler shifts are given by

$$\Delta\nu_D = \frac{1}{c}\frac{\mathrm{d}\,(nL)}{\mathrm{d}t}\nu_0, \tag{5.2}$$

where c is the speed of light in vacuum, ν_0 is the optical frequency which is transmitted through the fibre and nL is the optical path length. Doppler shifts can be caused either by mechanical perturbations or by temperature fluctuations. For example, a temperature drift of $1\,\mathrm{mK\,s^{-1}}$ on a 1000 km fibre link, on which a 200 THz optical carrier is transmitted, combined with a temperature sensitivity of the refractive index of approximately $1 \times 10^{-5}\,\mathrm{K^{-1}}$ would lead to a Doppler shift of approximately 10 kHz.

Since the round-trip phase noise cancellation method requires a bidirectional optical fibre link and standard telecoms fibre networks use unidirectional amplifiers with integrated isolators, most experiments carried out to date have used dark fibre links, which are fibres that do not carry any other optical signals. However, dark fibre links are very expensive to rent, and a permanent optical fibre network for the comparison of optical clocks will therefore most likely use ITU channels in existing fibre telecoms networks. In order to make a telecoms fibre network compatible with the round-trip phase noise cancellation method, the unidirectional EDFAs have to be bypassed using add-drop modules and bidirectional amplifiers. Lopez *et al.* [111] used this method on a 540 km long internet-traffic-carrying telecoms fibre networks for time and optical carrier frequency transfer. Their transfer results showed no degradation compared to dark fibre links, paving the way towards a fibre network for the comparison of remotely located clocks. Although this method requires more effort to implement because all unidirectional EDFAs along the fibre link have to be bypassed, the lower renting cost makes it attractive.

An alternative to the round-trip phase noise cancellation is two-way time and frequency transfer, which does not require optical path length stabilisation. This method, which will not be described in detail here, is only suitable when two clocks or frequency standards are to be compared; it is not suitable for the case where time or frequency signals are transmitted to

a remote user who does not maintain time and frequency standards. In this two-way method, the time and frequency signals are sent in opposite directions through a common fibre; this makes cancellation redundant because both signals experience the same phase fluctuations, assuming the fluctuations occur on time-scales much longer than the time it takes for the signals to travel through the fibre.

In order to measure the performance of time and frequency transfer methods, it is convenient initially to colocate the transmitter and user ends in the same laboratory so that they can be directly compared. In a deployed system, where it is not possible to perform an out-of-loop measurement, an upper limit for the one-way-performance can be obtained by sending the reference signal back to the transmitter end through a separate stabilised fibre link and comparing the round-trip signal to the transmitted signal.

5.2 Frequency transfer techniques

5.2.1 Microwave transfer via intensity modulation of an optical carrier

An ultra-stable rf or microwave signal derived from an atomic frequency standard can be transmitted via fibre by intensity modulation of a free-running cw laser. At the user end the rf or microwave modulation signal is recovered with a photodiode. Two different approaches to cancel the environmentally induced fluctuations of the fibre link exist. The first one is the round-trip phase noise cancellation method described above; the round-trip delay fluctuations are detected at the transmitter end and the link is stabilised via feedback to a fibre-stretcher, a delay line or a temperature-controlled fibre spool or a combination thereof. Using this technique, Lopez *et al.* [112] demonstrated the transfer of a 9.15 GHz microwave signal over an 86 km long fibre network; they achieved a fractional frequency instability for the frequency transfer of 1.3×10^{-15} at 1 s and 4×10^{-19} at 7×10^{4} s. In order to achieve this performance, a polarisation scrambler was used to overcome

the limitation caused by polarisation mode dispersion which causes the polarisation of the light to vary randomly along the fibre link, violating the reciprocity condition.

In the second approach, the round-trip noise is also measured at the transmitter end, but rather than actively stabilising the optical path length, the correction is directly applied to the microwave signal which is transmitted through the fibre. This technique, which is referred to as phase conjugation, has the advantage that it is not limited by the dynamic range of the actuator. Using this technique in combination with a polarisation scrambler, Wang *et al.* [113] demonstrated frequency transfer of a 9.1 GHz signal over a 91 km long fibre link with a fractional frequency instability of 7×10^{-15} at 1 s and 5×10^{-19} at 1×10^{5} s.

5.2.2 Optical carrier transfer

Direct optical carrier transfer can offer much higher stabilities compared to microwave transfer because the higher operating frequency enables a much higher resolution for measuring the phase fluctuations of the fibre link. This is the same concept which allows optical clocks to be more stable than their microwave counterparts. In this technique, a cw laser which is locked to the frequency standard of interest using a frequency comb is directly transferred to the user, where it can be compared to another frequency standard (optical or microwave) employing another frequency comb. The round-trip phase noise cancellation technique with feedback to an AOM cancels the Doppler shifts while the optical path length is not directly stabilised. Table 5.1 summarises the results obtained from some of the optical carrier transfer experiments on fibre links. Since the amount of noise that contributes to the fractional frequency instability depends on the measurement bandwidth (MBW), the MBW should always be stated in order to allow for comparison between different results. One technical challenge in long-distance frequency transfer is the degradation of the SNR due to unwanted back-reflections and Brillouin and Rayleigh scattering along the fibre link. This problem can be overcome by placing an AOM at the user end which makes it possible to dis-

Reference	L (km)	fractional frequency instability at 1 s	fractional frequency instability at 1000 s	MBW (Hz)
Jiang *et al.* [114]	86	2×10^{-16}	5×10^{-19}	10
Jiang *et al.* [114]	172	4×10^{-16}	2×10^{-18}	10
Williams *et al.* [115]	76	1×10^{-16}	3×10^{-19}	–
Predehl *et al.* [19]	920	4×10^{-14}	4×10^{-17}	–
Lopez *et al.* [111]	540	3×10^{-14}	3×10^{-17}	–
Droste *et al.* [20]	1840	1×10^{-13}	–	–
Calonico *et al.* [116]	1248	1×10^{-14}	1×10^{-17}	1
Raupach *et al.* [117]	660	5×10^{-14}	–	–
Raupach *et al.* [118]	1400	2×10^{-13}	2×10^{-16}	–

Table 5.1: Results of different direct carrier frequency transfer experiments over fibre links ranging from 76 km–1840 km; the transfer in [111] was carried out on an internet-carrying fibre network. Here, the fractional frequency instability is characterised by the Allan deviation. L: fibre link length; MBW: measurement bandwidth.

tinguish between unwanted back-reflections or back-scattered light and the return signal; in that case, the error signal is derived from the heterodyne beat between the local and the returned light. Another technical challenge is that the gain of bidirectional EDFAs is usually limited to around 20 dB because at higher gains the amplifier can start lasing due to back-reflections or Rayleigh back-scattering; such gain levels require a bidirectional EDFA approximately every 100 km along a fibre link. Fibre Brillouin amplifiers (FBA) only amplify light travelling in one direction which allows them to avoid spontaneous lasing and achieve small-signal gains in excess of 40 dB. FBAs have recently been used for frequency transfer on fibre links longer than 600 km [117, 118], where the average spacing between FBAs was approximately 200 km. On longer fibre links, FBAs therefore clearly offer an advantage compared to bidirectional EDFAs, but they are not yet commercially available. Other challenges include limitations due to polarisation mode dispersion and interferometer noise [110] which arises from any fibre components that are only passed by either the forward or the backward travelling light; however these contributions are usually small compared to the

total noise on longer fibre links.

When these technical noise sources are sufficiently reduced, a fundamental noise limit can be reached. This theoretical limit originates from a violation of the reciprocity of the bidirectional fibre link caused by time-dependent noise processes for which the free running fibre noise at the user end cannot be entirely suppressed, even if the round-trip noise is perfectly cancelled. This limit is well understood [115] and routinely achieved [20, 116]; it is given by

$$S_{\varphi}^{\text{user}}(f) = \frac{4\pi^2}{3}(f\tau)^2 S_{\varphi}^{\text{fibre}}(f), \tag{5.3}$$

where $S_{\varphi}^{\text{user}}(f)$ is the phase noise at the user end when the link is stabilised, τ is the one-way propagation delay and $S_{\varphi}^{\text{fibre}}(f)$ is the phase noise of the free-running fibre link. Due to this limit, the modified Allan deviation is proportional to $L^{3/2}$; this increase in phase noise with increasing fibre length explains why the fractional frequency instability results shown in table 5.1 are in general higher for longer fibre links. Since the free-running phase noise of fibre links cannot be perfectly cancelled, good passive stability is important; fibre links buried underground exhibit excellent passive stabilities corresponding to fractional frequency instabilities at the 10^{-14}–10^{-15} level (see [19] for example).

Recently, Calosso *et al.* [119] demonstrated a post-processing approach which enabled them to overcome the limit from equation 5.3. By implementing an algorithm, based on the phase of the returned signal and the signal at the user end, they were able to improve the phase noise by 6 dB compared to the delay-unsuppressed noise limit by applying a correction to the transmitted signal without actively cancelling the round-trip phase noise. Their method should also in principle be suitable for the comparison of the local signal with the returned signal, similar to the phase noise cancellation method.

In order to increase the phase noise cancellation locking bandwidth, longer fibre links can be divided into several subsections using regenerator stations which lock a laser to the incoming signal and stabilise the link up

to the next repeater station [120]. If the fibre link is divided into N Doppler cancelled subsections with uncorrelated noise, the locking bandwidth can be increased by a factor of N and the Allan deviation is reduced by a factor of N; this increase in stability comes at the cost of a more complex and expensive set-up.

5.2.3 Microwave and optical frequency transfer using a frequency comb

An optical frequency comb, locked to an optical reference, can be used to simultaneously transfer both optical and microwave frequencies through fibre links. The user has access to a large number of ultra-stable optical carriers and, after photodetection, access to rf and microwave frequencies at harmonics of the repetition rate. The round-trip phase noise cancellation technique with feedback to actuators that control the group delay can be used to stabilise the optical path length. The error signal can be derived either from a harmonic of the repetition rate [121] or from an optical beat between the optical comb modes [110]; the latter method offers orders of magnitude higher phase sensitivity. By transferring a 30 nm wide optical frequency comb through a dispersion compensated 86 km long stabilised dark fibre link, Marra *et al.* [122] demonstrated microwave frequency transfer with an instability of 5×10^{-15} at 1 s and 7×10^{-17} at 1000 s. The optical carrier frequency transfer capability of a frequency comb was demonstrated by Marra *et al.* [123] on a 8 km optically-stabilised fibre spool; the fractional frequency instability of the frequency transfer was 3×10^{-17} at 1 s and 4.5×10^{-18} at 1000 s for a 7 Hz measurement bandwidth. However, the optical carrier transfer capability of a frequency comb has yet to be demonstrated on an installed fibre link.

An alternative approach controls the repetition rate of the frequency comb rather than stabilising the optical path length, similar to the phase-conjugation method used for intensity modulated cw microwave transfer. Using this technique, Zhang *et al.* [124] demonstrated microwave frequency transfer over a 10 km fibre spool with a fractional frequency instability of

Reference	Technique	L (km)	Time deviation	Accuracy
Rost *et al.* [125]	TWTT	73	3 ps	74 ps
Lopez *et al.* [111]	TWTT	540	20 ps	250 ps
Krehlik *et al.* [108]	OWTT, on spools	69	0.3 ps	11 ps
Śliwczyński *et al.* [109]	OWTT	420	20 ps	112 ps
Śliwczyński *et al.* [109]	OWTT, on spools	480	0.7 ps	40 ps

Table 5.2: Results of different time transfer experiments over fibre links ranging from 73 km–420 km and fibre spools as indicated. TWTT: Two-way time transfer; OWTT: One-way time transfer; L: fibre link length.

3×10^{-14} at 1 s and 1.2×10^{-16} at 1000 s in a 3 Hz measurement bandwidth.

5.3 Time transfer

Fibre time transfer methods make use of either the one-way technique or the two-way-time-transfer configuration in which two remotely located time standards send their timing signals in opposite directions through a common, unstabilised fibre. In the one-way method, time transfer is performed on a fibre link that is stabilised by the round-trip phase noise cancellation technique used for frequency transfer, i.e. time and frequency signals are transferred simultaneously. One important difference between one-way time and frequency transfer is that while in frequency transfer the absolute delay of the fibre link is unknown, in time transfer the absolute delay introduced by the fibre link and electrical components has to be known. This makes calibration of the time transfer set-up necessary; this process is described in more detail in section 6.2.2.

Table 5.2 summarises the performance of one-way and two-way time transfer experiments over longer fibre networks; in all set-ups, time is transferred via amplitude modulated cw lasers, but different equipment is employed for the embedding of the timing information. A time reference is usually a 1 PPS (pulse per second) generator locked to a frequency stan-

dard. It produces one square wave per second and the fast rising edge is used as a timing reference. One common technique for the embedding of the timing information makes use of advanced satellite equipment, such as Satellite Time and Ranging Equipment (SATRE) modems, usually employed in two-way satellite time and frequency transfer. These modems exchange pseudorandom noise modulated carrier signals which are synchronised to the local 1 PPS generator. The modems are able to reconstitute the 1 PPS signal from the modulated carrier. This technique is used in [111, 125] in a two-way time transfer experiment. While in [125] the transfer was performed on a dark fibre network, in [111] the transfer was carried out on an internet-data-carrying telecoms fibre network, which was simultaneously used for Doppler-cancelled optical carrier transfer.

Krehlik *et al.* [108] and Śliwczyński *et al.* [109] developed an approach for time and rf frequency transfer in which cw lasers are modulated with square waves. A dedicated embedder incorporates a 1 PPS timing reference onto the square wave by time shifting the falling edge of the square wave while leaving the rising edge unchanged. This violation rule is used by the de-embedder to generate the 1 PPS timing signal at the user end. The rf frequency transfer is used to stabilise the delay of the fibre link by feeding back to application-specific integrated circuit electrical delay lines which exhibit a dynamic range of 100 ns, corresponding to a delay introduced by 20 m of fibre. This dynamic range is much larger than those achieved by optical delay lines or temperature-controlled fibre spools. Operating these electrical delay lines in combination with a set of fibre patch cords with specific optical delays which are selected by an optical switch, Krehlik *et al.* [126] have recently demonstrated a system capable of continually compensating for more than 1 µs of delay fluctuations. By overcoming the limited dynamic range of fibre-stretchers and temperature-controlled fibre spools, this technique paves the way for maintenance-free, long-term operation of time transfer and group-delay dependent frequency transfer over fibre links longer than 1000 km. This time transfer technique by Krehlik *et al.* has so far produced the highest stabilities and accuracies over longer distances. While the accuracy from the results on a 420 km long fibre network [109] were limited to 112 ps by the

uncertainty contribution of the time interval counter (TIC) available in this experiment, accuracies at the tens of ps-level have been achieved on fibre spools when a fast digital storage oscilloscope with a higher accuracy was used instead.

Since one-way time transfer methods make use of frequency transfer techniques to stabilise the optical path length, they face the same challenges present in group-dependent frequency transfer experiments. Furthermore, one technical challenge, which will be discussed in detail in the following chapter, is that special electrical equipment and testing devices have to be employed in order to calibrate and measure time delays with accuracies of tens of ps.

For applications such as large accelerator facilities or free-electron lasers, which require timing synchronisation at the fs-level over relatively short distances, fs pulses emitted by a mode-locked laser can be distributed via optical-path-length-stabilised fibre links for timing synchronisation. Since photodetection of optical pulse trains introduces timing jitter at the ps-level, fast photodiodes are not suitable for delay stabilisation at the fs-level. Hence, it is necessary to detect the delay in the optical domain using balanced optical cross-correlation [127] or linear optical sampling [128]. Timing synchronisation via distribution of fs-pulses on polarisation-maintaining fibre links of lengths up to a few km with fs-level timing drifts were demonstrated [55, 129].

5.4 Conclusions and summary

All three frequency transfer methods described in this chapter are capable of transferring the stability of state-of-the-art optical clocks to remote users. Out of the three techniques, optical carrier transfer has been studied most extensively, and has been used over fibre links of almost 2000 km length. The advantages of the optical carrier transfer are its high phase noise sensitivity, due to the high operating frequency, and the extremely large dynamic range of the Doppler-cancellation scheme. This technique has also produced the

highest stabilities and is therefore the preferred choice for long-distance clock comparison.

Frequency comb transfer provides an alternative to simultaneously transfer both optical and microwave signals. However, the optical carrier transfer capability has yet to be demonstrated on a real fibre network and the large bandwidths of optical frequency combs are not suitable for data-carrying telecoms networks. In the following chapter, a new technique for simultaneous time and microwave frequency transfer using a frequency comb is presented. Timing information is superimposed onto the pulse train using an intensity modulation scheme. Furthermore, the optical bandwidth is limited to a single ITU channel which paves the way for future frequency comb transfer over internet-carrying telecoms fibre networks.

One-way and two-way time transfer methods have been described. The one-way time transfer by Krehlik *et al.* offers sub-ps-level stability and accuracies of tens of ps over longer fibre links; this performance is significantly better than that of the other two-way time transfer methods based on advanced satellite equipment. For shorter distances, fibre synchronisation using optical fs-pulses can provide fs timing stabilities. However, achieving such high stability levels is technically demanding. Advanced optical detection methods have to be employed and careful dispersion control is required in order to avoid excessive pulse broadening.

6 Comb-based time and microwave transfer over a 50 km long fibre spool

This chapter describes a new comb-based time transfer technique and presents results obtained on a 50 km long fibre spool. Timing information is superimposed onto the pulse train from a mode-locked laser using an intensity modulator, and the time delay of the fibre is stabilised using the round-trip phase noise cancellation method. Since the bandwidth of the mode-locked laser used in this experiment is restricted to a single ITU channel, this technique could be employed on telecoms fibre networks. Filtering of the optical bandwidth to a single ITU channel has the additional advantage that the dispersion compensation becomes less difficult. In the first section of this chapter the microwave transfer technique that is used to stabilise the fibre link is described. In the second section, the time transfer experiment is presented.

6.1 Preliminary microwave frequency transfer experiment

This microwave frequency transfer experiment uses the same round-trip phase noise cancellation concept as in the experiments by Marra *et al.* on a 50 km long fibre spool [130] and on a 86 km long, dark fibre network [122].

While in those experiments the optical bandwidth of the frequency comb was approximately 90 nm (11 THz) and 30 nm (3.8 THz) respectively, here the bandwidth of the mode-locked laser is restricted to a single ITU channel, i.e. a bandwidth of 100 GHz (0.8 nm). The motivation for limiting the optical bandwidth is that it opens up the opportunity of using telecoms fibre networks for long-distance frequency comb transfer experiments.

6.1.1 Experimental set-up

Round-trip phase noise cancellation technique

The experimental set-up can be seen in figure 6.1. The phase noise of the fibre spool is measured and suppressed using the round-trip phase noise cancellation method described in section 5.1. The error signal is derived by comparing the 8 GHz harmonic signals of the repetition rate before and after the round-trip through the 50 km fibre spool. The error signal is sent to a home-built integrator, and the output of the integrator is sent to a home-built high-voltage amplifier (HVA) which drives the fibre stretcher with a voltage range of approximately 800 V. For the commercial fibre stretcher (Opti-Phase) this results in a delay compensation range of approximately 50 ps. In order to be able to lock the fibre link for a couple of minutes, the phase fluctuations of the fibre link were reduced by placing the 50 km long fibre spool in a wooden box and the fibre stretcher in an aluminium box, both shielded with thermal insulation foam. In the time transfer experiment (section 6.2) four fibre stretchers were employed in order to increase the dynamic range.

Optical side of the experiment

The frequency comb used in this experiment is the one described in section 4.2. Most of the light from the frequency comb was used for other experiments which meant that the light available for this experiment was only approximately 170 µW over the full bandwidth. Therefore, an EDFA was used to amplify the light. As can be seen in figure 6.2, this reduces the optical

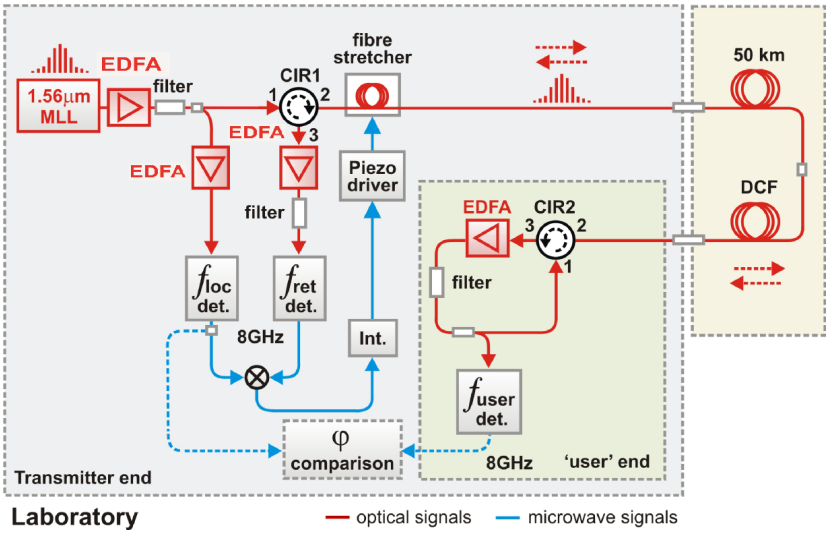

Figure 6.1: Schematic of the microwave transfer over a 50 km long fibre spool. The round-trip phase noise cancellation technique with feed back to a fibre-stretcher is used to compensate for the phase fluctuations of the fibre spool. The performance of the frequency transfer, in terms of phase noise and the fractional frequency fluctuations, is characterised by measuring the phase fluctuations between the 8 GHz harmonic at the transmitter and user ends using a microwave mixer. EDFA: Erbium-doped fibre amplifier; CIR: circulator; det.: photodetector; MLL: mode-locked laser; DCF: dispersion compensating fibre.

bandwidth from approximately 100 nm to approximately 30 nm. The spectrum is then filtered by the ITU channel 43 (centred around 1542.94 nm), and a 50/50 coupler splits the light into two paths (both have an optical power of 23 µW or −16.4 dBm). One portion of the light is again amplified by another EDFA in order to reach an optical power of approximately 300 µW on the local photodetector; the other portion is sent through the fibre link consisting of a fibre stretcher, a 50 km long standard single mode (SMF-28) fibre spool and a matched dispersion compensating fibre (DCF) module. When the light reaches the user end, it has a power of approximately 700 nW (−31 dBm). After amplification by another EDFA and filtering (channel 43) to reject the spontaneous emission of the EDFA, a 50/50 coupler splits the light and one portion is sent to the user photodiode while the other portion is sent back to the transmitter end via a circulator (CIR2). At the transmitter end the returned light is separated from the forward travelling

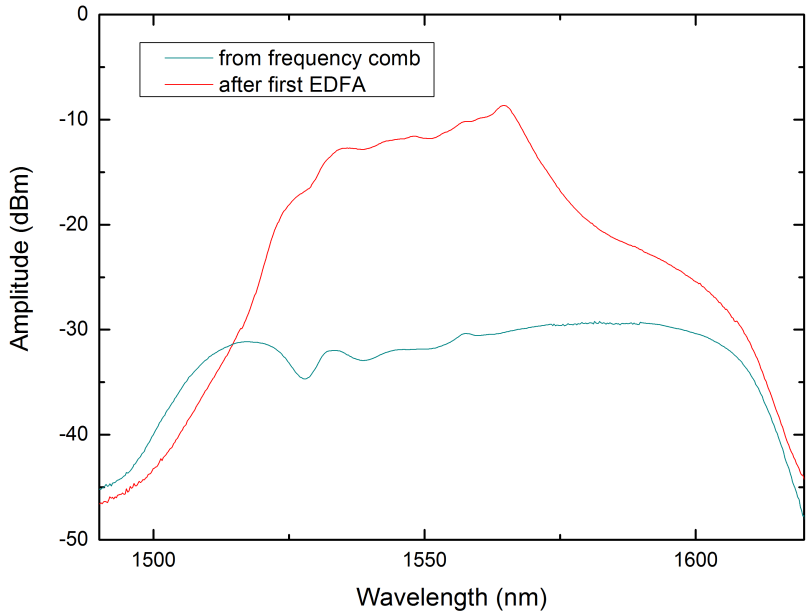

Figure 6.2: Optical spectra directly from the frequency comb (dark cyan) and after the first Erbium-doped fibre amplifier (red).

light by another circulator (CIR1) and again amplified and filtered before it is sent to the return photodiode. The light at the return photodiode is filtered by a wider bandpass filter (19 nm) because not enough channel 43 filters were available at the time when the experiment was carried out. The optical spectra recorded at all three photodiodes and the light which enters the fibre link can be seen in figure 6.3. The one-way loss of the fibre link was approximately 15 dB. By controlling the gain level of the EDFAs and using variable optical attenuators, the optical power on each photodiode (DSC40 Discovery Semiconductor) was adjusted to around 300 µW.

Dispersion management

One advantage of using an ITU-channel-filtered comb is that the pulse broadening caused by the dispersion of the fibre is smaller than that experienced by a broad frequency comb. This results in less stringent requirements for the dispersion management. The dispersion in SMF-28 is approximately $17\,\mathrm{ps\,nm^{-1}\,km^{-1}}$ at 1550 nm. Hence, while a comb with an optical bandwidth

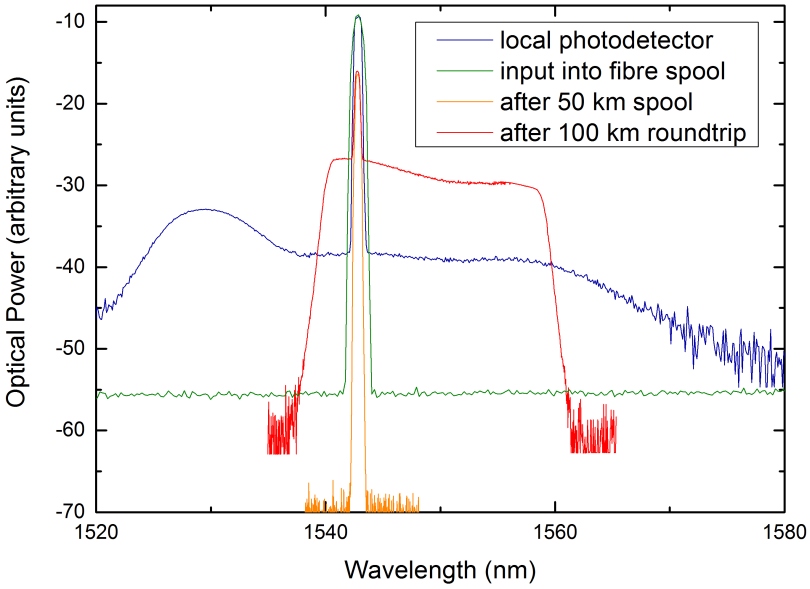

Figure 6.3: Filtered optical spectra measured at different points in the set-up. Blue: at local photodiode; green: at the input into the fibre link; orange: at the photodiode at the user end; red: at the return photodiode.

of 100 nm experiences a pulse broadening of approximately 1.7 ns km^{-1}, an ITU-channel-filtered comb (optical bandwidth of 0.8 nm) experiences a pulse broadening of less than 17 ps km^{-1} which is negligible compared to the case when a broad comb is used.

The DCF module compensates for a dispersion of 824 ps nm^{-1} and the dispersion at 1543 nm is approximately 16.6 ps nm^{-1} km^{-1} which gives a dispersion of 830 ps nm^{-1} over a length of 50 km of SMF-28 fibre. Therefore the pulse broadening contribution due to a mismatch between the fibre spool and the DCF module at the user end is approximately 5 ps.

Rf side of the experiment and phase noise measurement set-up

The 8 GHz signals were filtered with narrow rf bandpass filters (suppression of adjacent harmonic signals by more than 30 dB) and amplified with four low noise amplifiers (HMC606 Hittite) to approximately 9 dBm in order to saturate the microwave mixer (Marki microwave). The SNRs of the 8 GHz

signals after single and double pass of the fibre link were both in excess of 80 dB, measured 50 kHz from the carrier with a resolution bandwidth of 300 Hz. The microwave mixer and the other microwave components are mounted onto the optical table in order to reduce temperature-induced phase changes of the error signal.

The performance of the frequency transfer is evaluated by comparing the transmitted 8 GHz signal with the 8 GHz at the user end using a double balanced mixer as phase detector. This is possible because the user end and the transmitter end of the experiment are located in the same laboratory. The phase noise is measured by feeding the signal from the mixer to an FFT spectrum analyser, and the fractional frequency instability is obtained by recording the signal from the mixer with a digital voltmeter (DVM) with a measurement bandwidth of 7 Hz.

Problem of phase noise degradation by unwanted reflections

One problem of this set-up is that unwanted back-reflections (of the light which is sent back to the transmitter end) cause a degradation of the phase noise of the signal received at the user end. This reflected light can interfere with the real signal and the smaller the difference between the power of the reflected light and the real signal, the more significant the degradation of the phase noise. Reflections from FC/APC, angled physical contact optical fibre interconnections can be as low as 60 dB below the power of the signal. However, in practice such reflections are typically approximately 40 dB below the transmitted signal due to degradations of the polished surfaces. Furthermore backscattered light can increase the power of the reflected light. By measuring the optical power at port 3 of CIR2 when the comb was fed into port 1 of the circulator, the reflected light was measured to be only approximately 33 dB below the power of the transmitted light. The optical power that is sent from the transmitter end into the fibre link is approximately −16 dBm, which is attenuated to −31 dBm by the time it reaches port 3 of CIR2. The optical power available to send back to the transmitter end after the EDFA and the 50/50 coupler at the user end is approximately

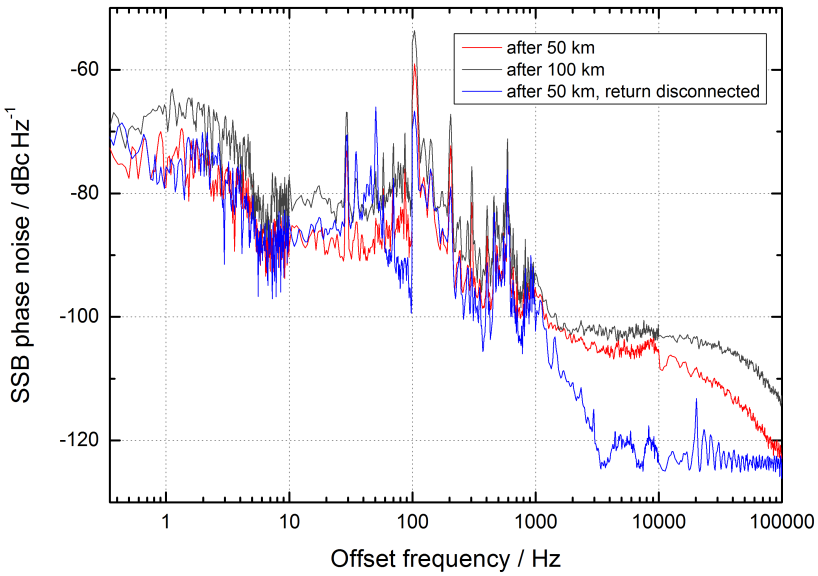

Figure 6.4: Phase noise of the 8 GHz harmonic signals at the user end and the return end. Blue: at the user end when the return signal is not connected to CIR2; red: at the user end when the return signal is connected to port 1 of CIR2; grey: at the return end. The phase noise degradation of the signal at the user end due to reflected and backscattered light can be seen. In the case of the red and grey curve the return signal was connected to CIR2 after being attenuated to −20 dBm. The fibre link was not stabilised in these measurements.

−7 dBm. When all the available power is sent back through the fibre, the reflected power is only approximately 10 dB below the power of the real signal. When a return power of −7 dBm was connected to port 1 of CIR2 this resulted in a drop of the rf power of the 8 GHz signal at the user end photodetector by 15 dB and significant amplitude fluctuations compared to the case where the return signal was not connected to the port 1 of CIR2. In order to solve this problem, an optical variable attenuator was added to the set-up to reduce the power of the return signal connected to port 1 of CIR2. While the phase noise at the user end improves with reducing return power, there is a trade-off between achieving a good noise performance at the user end and achieving a high enough SNR at the return photodiode in order to lock the delay of the fibre spool. For a return power of −20 dBm the SNRs of the 8 GHz signals at the user end and the return end were both in excess

of 80 dB (measured 50 kHz from the carrier with a resolution bandwidth of 300 Hz). For this case, the phase noise of the 8 GHz signals at the user and return ends are shown in figure 6.4. The phase noise at the user end in the case where the return signal is not connected to the circulator is also shown for comparison. The phase noise in that case is significantly lower compared to the case when the return signal is connected. The most pronounced difference can be seen at high offset frequencies, where it is possible to see self-heterodyne noise in the former case, which exhibits dips at multiples of 3.5 kHz (the inverse the round-trip time of the link). This reflection problem could in the future be further mitigated by fusion splicing critical fibre connections, as done in [130].

6.1.2 Results

The performance of the microwave transfer is characterised by comparing the 8 GHz signal at the user end and the transmitter end. In figure 6.5 the phase noise of the microwave transfer is shown when the fibre link is free running and when the fibre link is stabilised. Within the locking bandwidth of the feedback loop, which is limited to around 10 Hz by the bandwidth of the high-voltage amplifier, the phase noise of the free-running link is suppressed by up to 10 dB when the link is stabilised. The phase noise of the microwave transfer is approximately $-83\,\mathrm{dBc\,Hz^{-1}}$ at 1 Hz.

The overlapping Allan deviation was calculated from the voltage fluctuations of the mixer output which were recorded using a digital volt-meter with a measurement bandwidth of 7 Hz. As can be seen in figure 6.6, the fractional frequency instability is reduced by up to a factor of 2 when the link is stabilised and reaches values of approximately 8×10^{-15} at 1 s and 2×10^{-16} at 100 s.

6.1.3 Conclusions and summary

Frequency transfer using an ITU-channel-filtered frequency comb has been demonstrated for the first time. The phase noise of the 8 GHz microwave

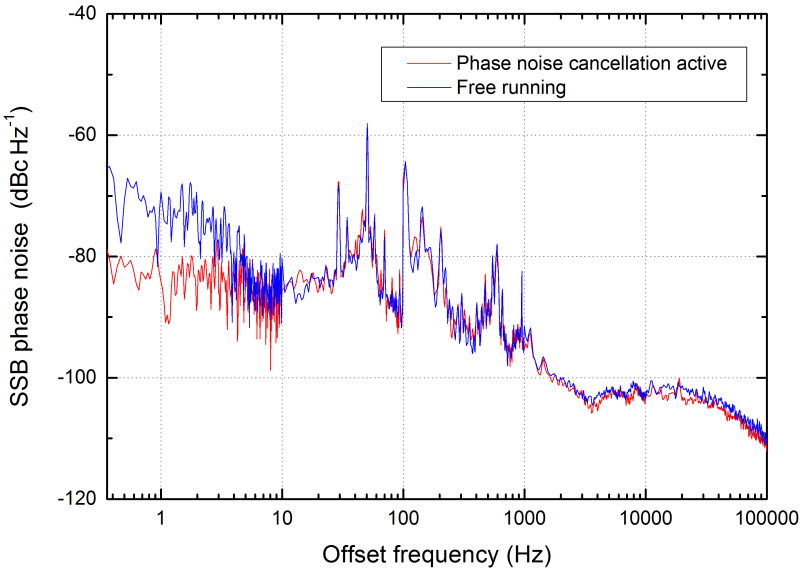

Figure 6.5: Phase noise of the 8 GHz microwave transfer when the fibre link is free-running (blue) and when the fibre link is stabilised(red); the measurements are obtained by comparing the 8 GHz signal at the user end with the local 8 GHz signal.

transfer over a 50 km fibre spool was $-83\,\mathrm{dBc\,Hz^{-1}}$ at 1 Hz and the fractional frequency instability was approximately 7×10^{-16} at 30 s. This experiment paves the way for longer distance fibre transfer experiments on telecommunication networks using ITU-channel-filtered frequency combs. The filtering of the frequency comb has the additional benefit that the reduced bandwidth places less stringent requirements on the dispersion management compared to the case where a broad optical comb is transmitted.

It should be noted that the purpose of this experiment was not to reach the lowest possible transfer stabilities; the main aim of this experiment was to show that frequency transfer is also possible with an ITU-channel-filtered comb. Therefore, no attempt was made to reach the lowest possible fractional frequency instability and the results were slightly worse (approximately by a factor of two in fractional frequency instability) than those achieved by Marra *et al.* [130] for transferring a 90 nm-wide comb over a 50 km fibre spool.

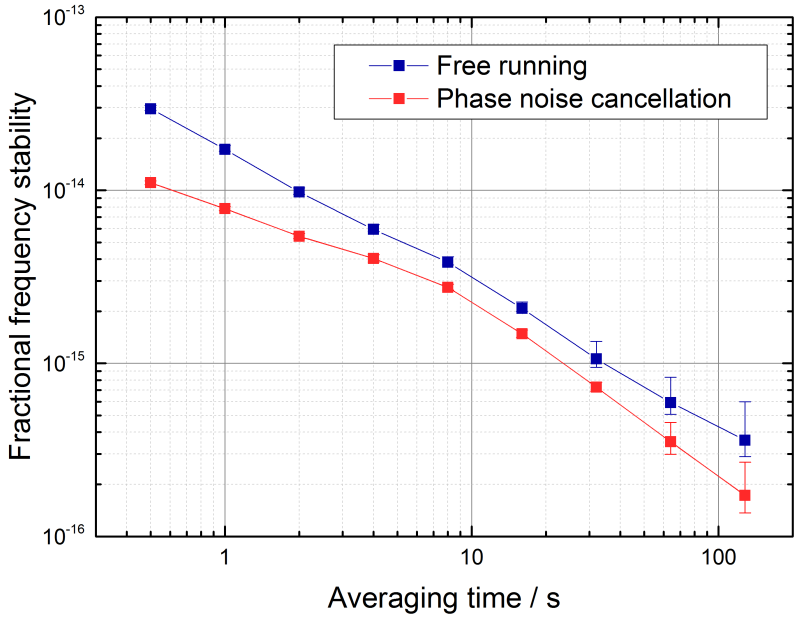

Figure 6.6: Fractional frequency stability of the microwave transfer when the fibre link is free-running (blue) and when the fibre link is stabilised(red); the overlapping Allan deviation is calculated from the phase fluctuations between 8 GHz signals at the user end and the transmitter end.

6.2 Time transfer experiment

In this section a new comb-based time transfer technique is described and results obtained on a 50 km fibre spool are presented. In order to stabilise the delay of the fibre, the round-trip-phase noise cancellation technique described in section 6.1.1 is employed. As will be described in section 6.2.1, timing information is superimposed onto the optical pulse train using an intensity modulator. While for frequency transfer the absolute delay introduced by the stabilised fibre link does not have to be known because it does not affect the frequency of the transmitted signal, for time transfer the knowledge of the absolute delay between the local clock signal and the signal that reaches the user is essential. In order to determine the absolute delay of the fibre link, the set-up must be calibrated before the experiment is carried out; a detailed description of the calibration process is provided in

section 6.2.2. Once the set-up is calibrated, the one-way delay can be predicted as half of the round-trip delay plus the calibration constant. Since in this experiment the transmitter and user ends of the time transfer set-up are co-located in the same laboratory, the characterisation of the time transfer stability and accuracy is obtained by directly comparing the timing signals at the transmitter and user ends. As will be described in section 6.2.3, in order to reach a time transfer accuracy of tens of ps, special measurement equipment is required and standard time interval counters are not suitable. In section 6.2.4 the time transfer stability and accuracy results are presented.

6.2.1 Experimental set-up

The schematic of the experimental set-up for the time transfer experiment over a 50 km fibre spool can be seen in figure 6.7. The fibre spool and DCF module are the same as in the previous experiment. Here, the $5th$ harmonic rather than the $80th$ is used for the round-trip phase noise cancellation of the fibre because the fast photodiodes which were used in the previous experiment were no longer available. Instead of using a frequency comb, here a mode-locked laser (M-Comb, Menlo Systems) with a repetition rate of 100 MHz is used. While the offset frequency is not stabilised, the repetition rate of the MLL is locked to a signal derived from a hydrogen maser. The ITU channel used in this experiment to filter the optical spectrum is channel 32, centred around 1551.72 nm. Three ITU channel filters were employed; one after the MLL, and one after each EDFA. Before the light from the MLL enters the set-up the optical bandwidth is filtered by an ITU channel filter (100 GHz), which reduces the number of optical modes to around 500. For Fourier limited pulses this would correspond to a pulse width of 3 ps.

A 1 pulse per second (PPS) generator (PPS-2, SpectraDynamics), locked to the hydrogen maser, is used as the time reference. Time intervals are either measured with a standard time interval counter (SR620, Stanford Research Systems) or a digital storage oscilloscope (TDS7404B, Tektronix). At the reference and return photodiodes, the rf signal is split into two. One portion is filtered by a 500 MHz bandpass filter and subsequently amplified

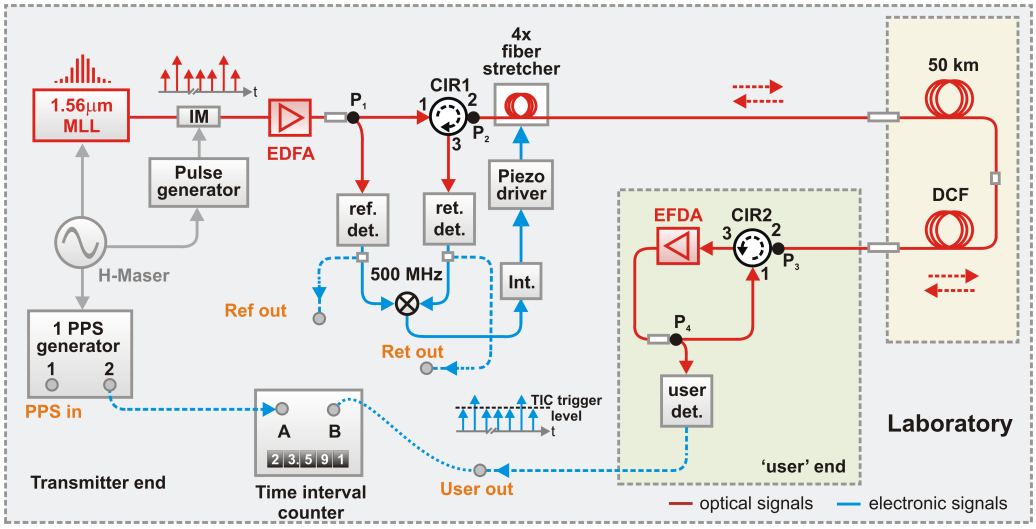

Figure 6.7: Schematic of the time transfer set-up. The fibre link is stabilised using the phase noise cancellation technique described in the previous section with the difference that, here, the error signal is derived from the $5th$ harmonic of the mode-locked laser. Via intensity modulation of the optical pulse train, the timing information of the local timing reference, a 1 pulse per second (PPS) generator locked to the hydrogen maser, is transmitted to the user end. Optical pulses with a higher amplitude act as time markers. Measurement of the round-trip delay of the fibre link together with the calibration of the set-up enables the prediction of the delay between the local 1 PPS reference signal and the remote time marker pulse. MLL: mode-locked laser; IM: intensity modulator; EDFA: erbium-doped fibre amplifier; CIR: circulator; ref.: reference; ret.: return; det.: detector; DCF: dispersion compensating fibre module; TIC: time interval counter.

(ZFL-500 HLN, Mini-Circuits) to generate an error signal using a double balanced mixer. The other portion is amplified (ZFL-500 HLN) and used for the time interval measurements. At the user output the electrical pulse train is also amplified (ZFL-500 HLN) but no 500 MHz signal is required. In order to be able to stabilise the fibre spool over a longer period than that achieved in the experiment from section 6.1, here four commercial fibre stretchers (Opti-phase) are driven by the HVA used in the previous experiment. This gives a total delay range of approximately 200 ps. In order to minimise temperature-induced delay drifts in non-common paths of the set-up the circulator and other fibre components are placed in a plastic box filled with temperature insulation foam. The EDFA at the user end contains

approximately 50 m of fibre. This is the largest contribution to non-common fibre paths. With a thermal coefficient of propagation delay in SMF-28 of $38\,\mathrm{ps\,km^{-1}\,K^{-1}}$, a fibre length of 50 m gives a delay change of $2\,\mathrm{ps\,K^{-1}}$ which means the temperature in the EDFA would have to change by 5 K in order to induce a delay change of 10 ps. Since it can be assumed that the temperature fluctuations in the EDFA are much smaller than that, temperature-induced path length changes are negligible compared to the several tens of ps uncertainty introduced by the time interval measurement equipment.

Superimposing timing information onto the pulse train

In order to superimpose timing information onto the optical pulse train, an amplitude modulation scheme is used in which time marker pulses have a higher amplitude compared to the other pulses. The time marker pulses are used to measure the time delay of the fibre link, while the pulses with smaller amplitude are employed in the frequency transfer technique that is used to cancel the phase fluctuations of the fibre link. In order to achieve the amplitude modulation, a 10 GHz Mach-Zehnder intensity modulator (MZIM) (LN81S-FC, Thorlabs) is driven by a commercial pulse generator (Agilent 81101A) with a bandwidth of 50 MHz, locked to the hydrogen maser. The MZIM is operated at the positive quadrature position with the result that the amplitude of the pulses is halved when no signal is applied to the rf port of the modulator. To generate time marker pulses, the pulse generator produces pulses of approximately 10 ns length (rising and falling edges are approximately 2.5 ns long) with an amplitude of 2 V and a period that can be controlled by the pulse generator. In between the electrical pulses the signal of the pulse generator drops back to 0 V. The phase of these electrical pulses is controlled with respect to the phase of the optical pulses so that the time marker pulses coincide approximately with the middle of the electrical pulses which increases their amplitude with respect to that of the other pulses. This can be seen in figure 6.8. Since the optical pulses (pulse spacing is 10 ns) coincide with the middle of the electrical pulses (duration of 10 ns), the optical pulses adjacent to a time marker pulse are not increased

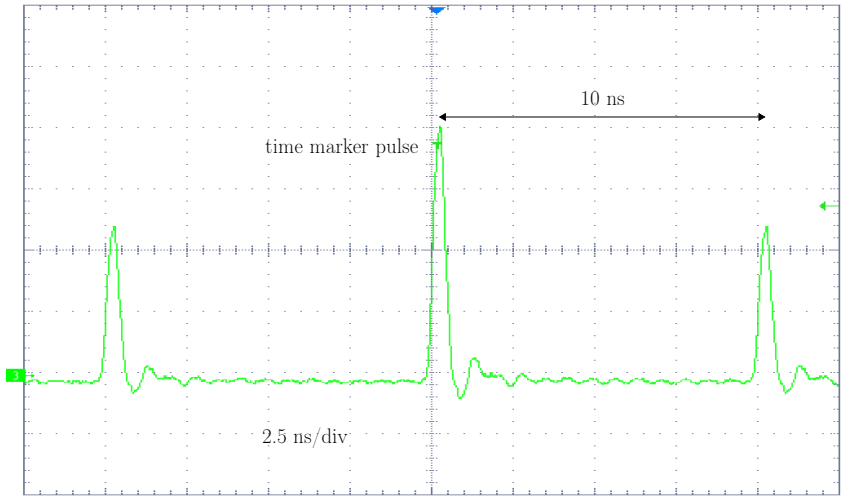

Figure 6.8: Oscilloscope measurement of the optical pulses after photodetection and rf amplification. The rise time of the pulses is limited to approximately 200 ps by the bandwidth of the photodiode which is 1.5 GHz. The time marker pulse amplitude is approximately 1.7 times larger than the amplitude of the other pulses.

in amplitude because the modulation voltage has dropped back to zero when they reach the MZIM.

The timing jitter of the pulse generator is proportional to the pulse period, and the maximum period that can be used before adjacent optical pulses are also modulated due to the jitter is approximately 800 µs. The period of the time marker pulses can also be chosen to be much smaller than that. The oscilloscope trace in figure 6.9 shows a time marker period of 400 ns for instance. For the time delay measurements of the fibre link the period of the time marker pulses has to be taken into account. In the simplest case, there is only one time marker pulse in the fibre link per round-trip delay. Therefore, the same time marker pulse starts and stops the time interval counter and the delay corresponds to the reading on the counter. As described in section 6.2.3, when a digital storage oscilloscope is used to measure the time delays, it is necessary to choose a small time marker period because the accuracy of the oscilloscope is proportional to the duration of the measured delay. In that case, there are many time marker pulses in the fibre link at any one time which means it becomes more complicated to

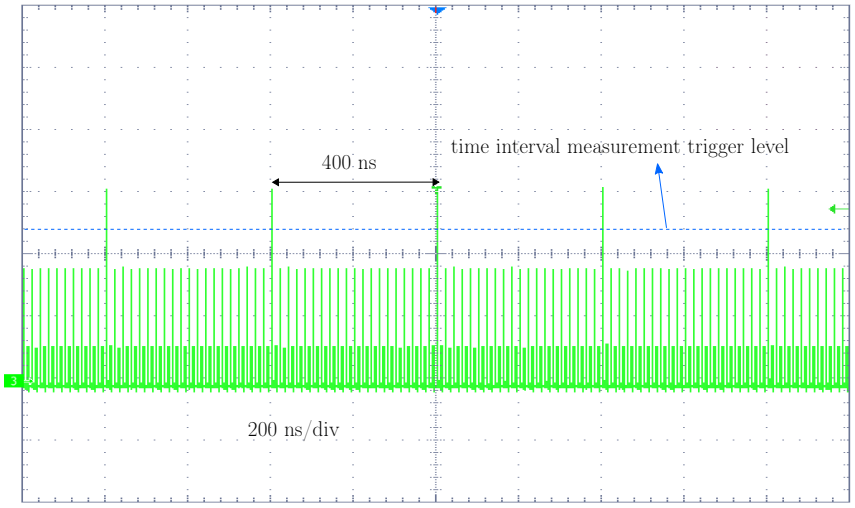

Figure 6.9: Oscilloscope measurement of the optical pulses after photodetection and rf amplification. Here the time marker period is 400 ns. The dashed blue line indicates the trigger level for the time interval measurements. By choosing a trigger level above the amplitude of the smaller pulses, only the time marker pulses are used in the time delay measurements.

obtain the fibre link delay from the value measured by the oscilloscope. The specially devised measurement technique presented in section 6.2.4 can be used for this purpose.

It is necessary to lock the MZIM to the positive quadrature position, because temperature drifts otherwise change the amplitude of the optical pulses and the ratio between the time marker pulses and the other pulses. When left unstabilised, this drift was significant over longer periods. Therefore, a PI control loop was implemented to lock the MZIM to the positive quadrature position. The MZIM was furthermore clamped to an aluminium board, with thermal conducting paste at the intersections, and the aluminium board was clamped to an optical breadboard.

6.2.2 Calibration of the time transfer

The procedure used to calibrate the time transfer is based on the same concept as in [108]. The time delay between the local time reference (1 PPS generator) and the corresponding time marker pulse at the user end is

calculated as half of the measured round-trip delay, which can be monitored in the transmitter laboratory even when the signal is sent to a remote user, plus a constant calibration factor which takes account of any delays which are non-common to the forward and backward directions of the fibre link. The reference output and the return output of the set-up are used to measure the round-trip delay. The calibration factor has to be determined before the time transfer experiment is carried out. In the following the concept for the time transfer calibration will be described.

The 1 PPS generator (PPS-2 SpectraDynamics) emits pulses with a rise-time of 3 ns and a duration of 50 µs. Since the pulse generator superimposes timing information onto the optical pulse train rather than the PPS generator, there is a time interval $\Delta T_{\mathrm{In,Ref}}$ between the release of the 1 PPS signal and the arrival of the corresponding optical time marker pulse at the reference output which has to be determined. This time interval can be measured at the transmitter end by comparing the delay between the PPS signal and the time marker pulse at the reference output, and it will be constant during the operation as the MLL, the pulse generator and the PPS generator are all locked to the hydrogen maser. The time interval $T_{\mathrm{In,Ref}}$ can be expressed as the sum of the following time delays experienced by the time marker pulse: t_{x}, which is the unknown delay it takes the time marker pulse to travel from the unknown point where it is when the PPS signal is released to the output of the first 50/50 coupler (denoted as P_1 in figure 6.7), and t_2, which includes all delays due to fibre pigtails and rf components between P_1 and the reference output. The other delays in the schematic are as follows: t_3 is the delay of the fibre pigtails between P_1 and P_2, t_4 includes all delays due to fibre pigtails between P_3 and P_4, t_{EDFA} is the delay of the EDFA at the user end, t_5 includes all delays due to fibre pigtails and rf components between P_4 and the user output, t_6 includes the delay of fibre pigtails between P_4 and P_3, t_7 includes the delay of fibre pigtails and rf components between P_2 and the return output, and $\tau_{\mathrm{Fib\_F}}$ and $\tau_{\mathrm{Fib\_B}}$ are the delays of the forward and the backward directions of the fibre link.

The time intervals of interest (dashed blue lines in figure 6.10) can be

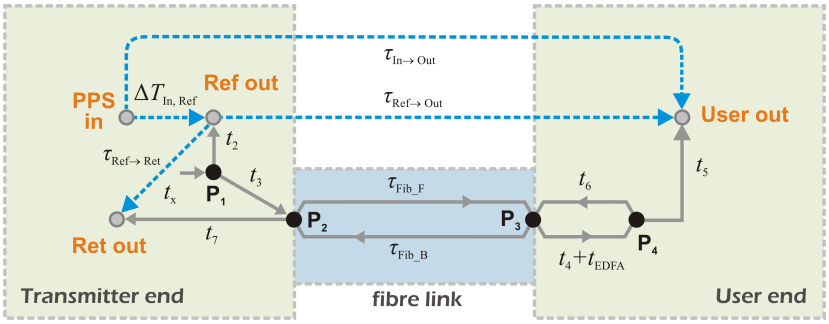

Figure 6.10: Schematic of the timing model of the time transfer set-up. The time intervals between the 1 PPS signal and the user output as well as the return output can be directly measured (dashed blue lines) in the laboratory using a time interval counter or a digital storage oscilloscope. The calibration constant takes into account all non-common fibre and rf delays (t_2, t_3, t_4, t_5, t_6, t_7 and t_{EDFA}) from components which are not passed twice on the round-trip. It is not necessary to determine those delays individually. Instead, as described in this section, there is a convenient method to obtain the sum of the delays of all the non-common paths by making only two measurements. Although $\Delta T_{\mathrm{In,Ref}} = t_x + t_2$, t_{x} does not originate from PPS in because t_x and t_2 are the time delays experienced by the time marker pulse rather than the PPS signal. When the PPS pulse is released, the corresponding time marker pulse is at the origin of the time interval vector labelled t_x.

expressed using the time delays defined above as:

$$\Delta T_{\mathrm{In,Ref}} = t_x + t_2, \tag{6.1}$$

$$\tau_{\mathrm{In\rightarrow Out}} = t_x + t_3 + \tau_{\mathrm{Fib\_F}} + t_4 + t_{\mathrm{EDFA}} + t_5, \tag{6.2}$$

$$\tau_{\mathrm{Ref\rightarrow Out}} = -t_2 + t_3 + \tau_{\mathrm{Fib\_F}} + t_4 + t_{\mathrm{EDFA}} + t_5, \tag{6.3}$$

$$\tau_{\mathrm{Ref\rightarrow Ret}} = -t_2 + t_3 + \tau_{\mathrm{Fib\_F}} + t_4 + t_{\mathrm{EDFA}} + t_6 + \tau_{\mathrm{Fib\_B}} + t_7. \tag{6.4}$$

Using equations 6.1–6.4, the delay between the local time reference signal (PPS generator) and the user timing signal (time marker pulse) can be expressed as:

$$\tau_{\mathrm{In\rightarrow Out}} = \Delta T_{\mathrm{In,Ref}} + \frac{1}{2}\tau_{\mathrm{Ref\rightarrow Ret}} + \frac{1}{2}(\tau_{\mathrm{Fib\_F}} - \tau_{\mathrm{Fib\_B}}) + \frac{1}{2}\tau_{\mathrm{c}}, \tag{6.5}$$

where τ_{c} is a calibration factor that takes account of the non-common paths

between the forward and the backward directions of the path of the pulse train:

$$\tau_c = -t_2 + t_3 + t_4 + t_{EDFA} + 2t_5 - t_6 - t_7. \tag{6.6}$$

There is a convenient method to determine τ_c, when the local and the remote modules are placed in the same laboratory. In the case of time transfer to a remote user, τ_c has to be determined before the user module is installed. In order to determine τ_c, the fibre link (including the fibre spool, the FSs and the DCF modules) is replaced by a variable fibre attenuator which is tuned to give the same attenuation as the fibre link. As a consequence, the difference between τ_{Fib_F} and τ_{Fib_B} is negligible, and by inserting equations 6.1, 6.2 and 6.4 into equation 6.5, the calibration factor can be expressed as:

$$\tau_c = 2\tau'_{Ref\to Out} - \tau'_{Ref\to Ret}, \tag{6.7}$$

where the primes indicate that this is the calibration measurement in which the fibre link is replaced by an attenuator. Hence, τ_c can be determined by making only two measurements. Once the calibration factor is known, the absolute delay $\tau_{In\to Out}$ of any delay-stabilised fibre link can be determined via equation 6.5 by measuring $\Delta T_{In,Ref}$ and $\tau_{Ref\to Ret}$ in the transmitter laboratory.

6.2.3 Uncertainty budget of the time transfer

The term $\tau_{Fib\_F} - \tau_{Fib\_B}$ in equation 6.5 is the delay difference between the forward and the backward directions of the fibre link. In this experiment, a small difference between the forward and backward delays may arise due to polarisation mode dispersion (PMD). An upper limit for the PMD coefficient in SMF-28 is $0.04\,\mathrm{ps\,km^{-1/2}}$ [131] and the value for the DCF fibre is similar [132]. Therefore the uncertainty due to PMD for the 50 km long fibre spool and the approximately 7 km long DCF module can be estimated as approximately 0.3 ps which is negligible compared to the uncertainty introduced by the time interval measurement equipment.

In the case where time is transferred to a remote user, $\tau_{Fib\_F} - \tau_{Fib\_B}$ also

contains a term due to the Sagnac effect which takes into account the effect of the earth rotation on the propagation of electromagnetic waves [133]. For instance in [109], the propagation delay difference between the forward and backward directions through a 420 km fibre link due to the Sagnac effect was approximately 1.7 ns, however Śliwczyński *et al.* were able to predict this difference with an uncertainty of 5 ps due to their knowledge of the route of the fibre link. Here, this term cancels out because the user and the transmitter ends are located in the same laboratory.

It should be noted that when two cw lasers with different wavelengths are used for the different propagation directions through a fibre link without dispersion compensation, $\tau_{\mathrm{Fib\_F}} - \tau_{\mathrm{Fib\_B}}$ contains the contribution:

$$(\lambda_{\mathrm{F}} - \lambda_{\mathrm{B}}) \times 17\,\mathrm{ps\,km^{-1}\,nm^{-1}} \times L, \tag{6.8}$$

where λ_{F} and λ_{B} are the wavelengths of the lasers propagating in the forward and backward direction, $17\,\mathrm{ps\,km^{-1}\,nm^{-1}}$ is the dispersion coefficient of SMF-28 fibre and L is the length of the fibre link. It is therefore necessary to take the different propagation delays into account and estimate their contribution to the overall uncertainty. In the time transfer method by Krehlik *et al.* [108], discussed in section 5.3, the uncertainty associated with determining the wavelengths of the two different lasers due to the resolution of the optical spectrum analyser in combination with the chromatic dispersion of the fibre is the largest uncertainty contribution in their time transfer experiment. In addition, this uncertainty contribution increases for longer fibre links. For instance, Krehlik *et al.* reported a time transfer uncertainty of 9 ps for a 98 km long fibre link (fibre spools), and an increased uncertainty of 24 ps for a 490 km long fibre link (fibre spools) [126].

Here, the dispersion of the 50 km fibre spool is compensated for by a DCF module which compensates for a dispersion of $824\,\mathrm{ps\,nm^{-1}}$. The dispersion of the SMF-28 fibre at the wavelength of channel 32 (1551.72 nm) is approximately $17\,\mathrm{ps\,nm^{-1}\,km^{-1}}$ which gives a dispersion of $850\,\mathrm{ps\,nm^{-1}}$ for the 50 km fibre spool. Therefore the mismatch between the DCF module and the fibre spool results in a pulse broadening after a single-pass of ap-

proximately 15 ps for an optical bandwidth of 0.8 nm. However, the pulses experience the same dispersion in both directions through the fibre link, and because only the delay mismatch between the forward and the backward delays matters ($\tau_{\mathrm{Fib\_F}} - \tau_{\mathrm{Fib\_B}}$), the pulse broadening effect due to a dispersion mismatch will cancel out in the time transfer experiment. The method presented here therefore clearly offers an advantage compared to the technique by Krehlik *et al.* because the uncertainty is not expected to increase with increasing length of the fibre link (assuming the dispersion is appropriately compensated for).

In order to achieve time transfer with an accuracy at the ps-level, it is of major practical importance that suitable, high accuracy measurement equipment is used to determine the time intervals of equation 6.5. Standard time interval counters such as the SR620 (Stanford Research Systems) are not suitable for this purpose as the uncertainty of the SR620 for a time interval measurement is approximately 0.5 ns [134]. For relative measurements, the uncertainty of the SR620 is approximately 50 ps [134]. In a relative measurement, the delay of interest is measured by making two time interval measurements, which yield the delay of interest when they are subtracted. In order to achieve ps-level accuracies, high-speed digital storage oscilloscopes can be used. In their experiments, Krehlik *et al.* use a 10 GHz Agilent DSO81004 oscilloscope which allows them to measure time intervals with an accuracy of 5 ps [126].

When this time transfer experiment was first carried out, only an SR620 was available, which meant that the overall accuracy was limited by the SR620 to approximately 0.08 ns. After the first measurements with an SR620, a 4 GHz digital storage oscilloscope (Tektronik TDS7404B [135]) was borrowed from another group within NPL in order to improve the accuracy to approximately 0.01 ns. In the following the total uncertainty of the time transfer is calculated for both devices.

Source	Uncertainty (ps)	Sensitivity coefficient	Uncertainty contribution (ps)
$\tau'_{\mathrm{Ref}\rightarrow\mathrm{Out}}$	50	2	100
$\tau'_{\mathrm{Ref}\rightarrow\mathrm{Ret}}$	50	1	50
Total uncertainty τ_{c}			**0.1 ns**

Table 6.1: Uncertainty in determining the calibration factor with an SR620 time interval counter. Every time interval measurement has an uncertainty of 50 ps and the sensitivity factors from equation 6.7 are taken into consideration. The value of the total uncertainty has been rounded.

Source	Uncertainty (ps)	Sensitivity coefficient	Uncertainty contribution (ps)
$\Delta\mathrm{T}_{\mathrm{In,Ref}}$	50	1	50
$\tau_{\mathrm{Ref}\rightarrow\mathrm{Ret}}$	50	0.5	25
PMD	0.3	0.5	0.2
τ_{c}	112	0.5	56
Total uncertainty $\tau_{\mathrm{In}\rightarrow\mathrm{Out}}$			**0.08 ns**

Table 6.2: Uncertainty in determining $\tau_{\mathrm{In}\rightarrow\mathrm{Out}}$ using an SR620 time interval counter. Every time interval measurement has an uncertainty of 50 ps and the sensitivity factors from equation 6.5 are taken into consideration. The value of the total uncertainty has been rounded. PMD: Polarisation mode dispersion.

Uncertainty budget using an SR620 time interval counter

In order to determine the total uncertainty for $\tau_{\mathrm{In}\rightarrow\mathrm{Out}}$, all uncertainty contributions of the terms on the right side of equation 6.5 have to be added in quadrature. The uncertainty of τ_{c} is obtained by adding the uncertainties on the right side of equation 6.7 in quadrature. Table 6.1 shows the uncertainty for determining τ_{c} and table 6.2 shows the total uncertainty for determining $\tau_{\mathrm{In}\rightarrow\mathrm{Out}}$ when an SR620 is used to measure the time intervals. The total uncertainty for the time transfer is approximately 0.08 ns.

Uncertainty budget using a TDS7404B digital storage oscilloscope

The delta time measurement accuracy given in the TDS7404B manual only relates to using a single channel. It also states that the delay between channels is less than 30 ps, but it does not state an accuracy for relative time interval measurements [135]. Assuming that any delay offsets between channels are constant they should in principle not contribute to relative time delay measurements. Therefore, here the assumption is made that the single channel time accuracy also applies for relative time delay measurements. There was not enough time in order to thoroughly test this assumption as part of this thesis. However, if the assumption was wrong and the uncertainty was larger, one would expect this to manifest itself in a larger uncertainty in the experimental verification of the time accuracy measurements, which was not the case. The time uncertainty of the TDS for single channel measurements is given by [135]:

$$0.06/\text{samplerate} + 2.5\,\text{ppm} \times |\text{reading}|\,. \tag{6.9}$$

For a sample rate of $10\,\text{GSs}^{-1}$ this becomes:

$$6\,\text{ps} + 2.5\,\text{ppm} \times |\text{reading}|\,. \tag{6.10}$$

Therefore, the TDS7404B is not suitable to measure time intervals above 2 µs with an accuracy below 10 ps. For a time interval of 568 µs, which corresponds to the round-trip delay of the 50 km fibre spool link, the uncertainty contribution of the oscilloscope would be larger than 1 ns. In order to overcome this limitation, a special measurement technique was devised in which the time marker period is reduced to 100 ns so that the oscilloscope only measures time intervals below 100 ns, and the total delay of the fibre link is calculated from the knowledge of the number of pulses that are in the link. This technique will be described in detail in the next section. For a time interval measurement of 100 ns, the uncertainty of the oscilloscope is below 7 ps. Using the same principle of adding the different uncertainty contributions in quadrature as in the case of the SR620, the uncertainty for

Source	Uncertainty (ps)	Sensitivity coefficient	Uncertainty contribution (ps)
$\tau'_{\mathrm{Ref}\rightarrow\mathrm{Out}}$	7	2	14
$\tau'_{\mathrm{Ref}\rightarrow\mathrm{Ret}}$	7	1	7
Total uncertainty τ_c			**0.02 ns**

Table 6.3: Uncertainty in determining the calibration factor with a TDS7404B digital storage oscilloscope. Every time interval measurement has an uncertainty of 7 ps and the sensitivity factors from equation 6.7 are taken into consideration. The value of the total uncertainty has been rounded.

Source	Uncertainty (ps)	Sensitivity coefficient	Uncertainty contribution (ps)
$\Delta\mathrm{T}_{\mathrm{In,Ref}}$	7	1	7
$\tau_{\mathrm{Ref}\rightarrow\mathrm{Ret}}$	7	0.5	4
PMD	0.3	0.5	0.2
τ_c	16	0.5	8
Total uncertainty $\tau_{\mathrm{In}\rightarrow\mathrm{Out}}$			**0.01 ns**

Table 6.4: Uncertainty in determining $\tau_{\mathrm{In}\rightarrow\mathrm{Out}}$ using a TDS7404B digital storage oscilloscope. Every time interval measurement has an uncertainty of 7 ps and the sensitivity factors from equation 6.5 are taken into consideration. The value of the total uncertainty has been rounded. PMD: Polarisation mode dispersion.

τ_c (see table 6.3) and the total uncertainty $\tau_{\mathrm{In}\rightarrow\mathrm{Out}}$ (see table 6.4) can be calculated. The total uncertainty of approximately 0.01 ns is significantly lower than that obtained with the SR620 time interval counter.

6.2.4 Results

Stability

The stability of the time transfer is measured by comparing the time marker pulses at the reference output and the user output. The time marker period is set to 800 µs, so that there is only one time marker pulse in the fibre at any one point (the one way delay of the link is approximately 284 µs). Hence, the same time marker pulse starts and stops the time interval measurement

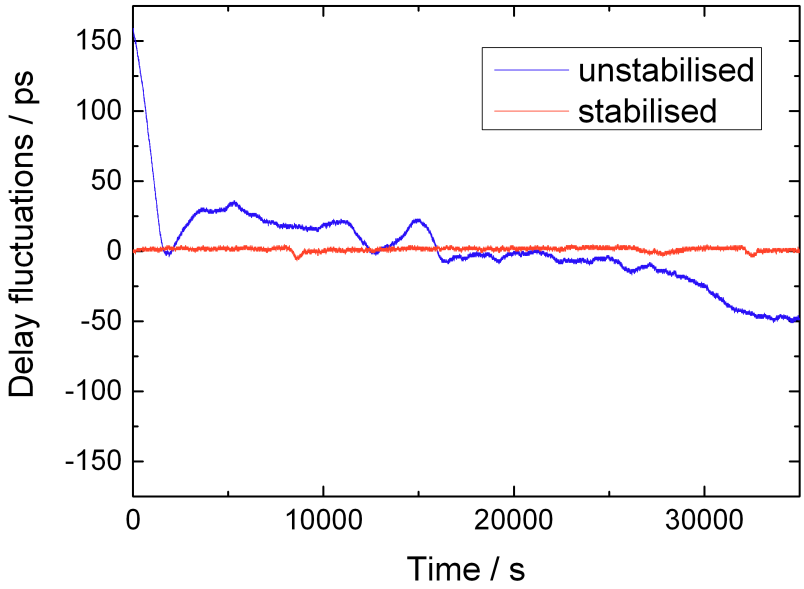

Figure 6.11: Residual delay fluctuations of the 50 km fibre link when it is free-running and when it is stabilised. The measurements were obtained using an SR620 time interval counter triggered by the time marker pulses (period 800 µs) and averaging over 1000 samples.

carried out by the SR620 time interval counter. The SR620 has a dead-time of 800 µs between individual measurements and the averaging was set to a sample size of 1000. In figure 6.11 the residual time fluctuations of the fibre link can be seen. The time delay fluctuations of the free running 50 km fibre spool caused by temperature fluctuations in the laboratory are approximately 210 ps peak-to-peak over 35 000 s. When the link is stabilised using the four fibre stretchers the time delay fluctuations are reduced to 15 ps peak-to-peak over the same time period. From the delay fluctuations the time deviation (equation 2.20) can be calculated. As can be seen in figure 6.12 the time deviations for the free-running and the locked fibre link are approximately the same for averaging times below 100 s, reaching 300 fs at 25 s. For longer averaging times, the time deviation of the free-running link increases to approximately 30 ps at 10 000 s. For the stabilised link the time deviation stays below 1 ps for all averaging times. Above 1000 s the locking of the link improves the time deviation by more than an order of

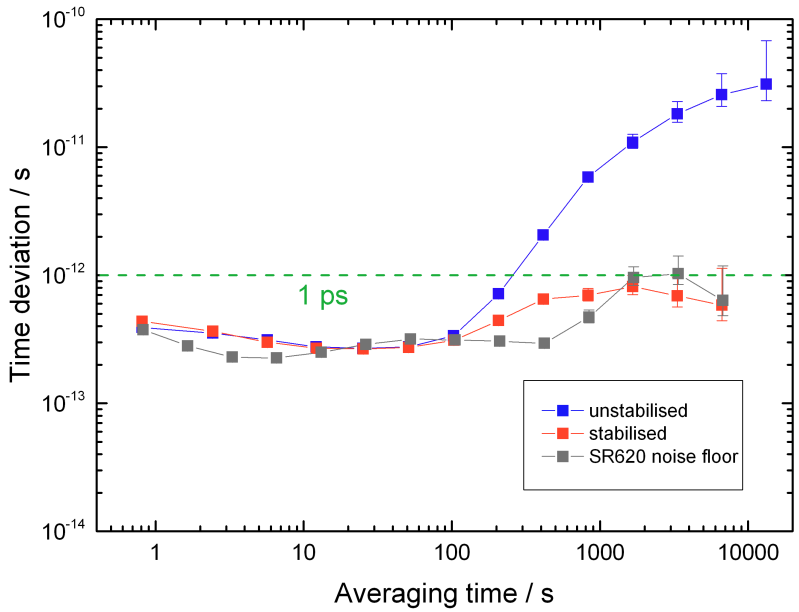

Figure 6.12: Time deviation of the 50 km fibre link when it is free-running and when it is stabilised. The noise floor of the SR620 is measured by triggering both its inputs with a common time marker signal from the reference output.

magnitude compared to the free-running link. At short averaging times the time deviations in the stabilised and free running case are limited by the resolution of the SR620—the least significant digit of the SR620 is 1 ps. At longer averaging times the time deviation of the stabilised link is limited by the long term fluctuations of the SR620. The noise floor of the SR620 was measured by splitting the reference output by a 50/50 rf coupler and feeding the two output signals to the two inputs of the SR620. One of the coupler outputs was connected via a longer rf cable in order to generate a detectable time interval of a couple of ns. The residual fluctuations of the SR620 at longer averaging times are attributed to temperature fluctuations. There was always an increase at longer averaging times but the exact shape and location varied slightly from measurement to measurement. The grey line in figure 6.12 shows a typical measurement. The time deviation of 300 fs reported here is at the same level as the best results over longer distances reported to date by Krehlik *et al.* [108] (see table 5.2).

Accuracy (SR620)

In the following the procedure to determine the time transfer accuracy with an SR620 time interval counter is described. The time marker period is set to 800 µs. In order to obtain relative time interval measurements—which are required in order to reach an accuracy of 50 ps with the SR620—channel A (which starts the time interval measurement) is always triggered by the same signal, namely output two of the PPS generator. Relative measurements are then obtained by sequentially connecting the signals of interest to channel B (stops the time interval measurement) and taking the difference between two measurements. The semi-rigid SMA cable used to connect the signal of interest to channel B is always the same. In that way, the delay of the cable does not have to be known as it cancels out when the difference between two measurements is taken. The rf amplitude of the time marker pulses at the defined outputs (Ref out, User out and Ret out) is adjusted to a level of approximately 1.2 V using variable optical attenuators before the user and return photodiodes. The trigger level on the SR620 is set to approximately 0.8 V and the averaging of is set to 10 samples.

At first, the time transfer set-up calibration constant τ_c is determined via equation 6.7. The value of $\tau'_{\mathrm{Ref}\to\mathrm{Out}}$ is obtained by sequentially connecting Ref out and User out to channel B and taking the difference between the two measurements. The value of $\tau'_{\mathrm{Ref}\to\mathrm{Ret}}$ is obtained using the same principle. In table 6.5 a calibration measurement can be seen. The actual values of the time interval measurements depend on the time delay between the 1 PPS signal that triggers channel A, and the arrival of the next time marker at the reference output. This delay will always be smaller than the period of the time marker pulses. The calibration measurement of table 6.5 results in a calibration constant τ_c of (131.7 ± 0.1) ns.

Once the set-up is calibrated, the next step is the verification of the calibration over the 50 km fibre spool. For this purpose the link is stabilised and the prediction of $\tau_{\mathrm{In}\to\mathrm{Out}}$ (right side of equation 6.5) is compared to the direct measurement of $\tau_{\mathrm{In}\to\mathrm{Out}}$. In table 6.6 a verification measurement is shown. The signals PPS in, Ref out, Ret out and User out are sequentially

Time interval measurements	
Signal	TI (ps)
Ref out	616 830 327
Ret out	617 010 223
User out	616 986 114
Calculated time delays	
Delay	TI (ps)
$\tau'_{\mathrm{Ref}\rightarrow\mathrm{Out}}$	155 787
$\tau'_{\mathrm{Ref}\rightarrow\mathrm{Ret}}$	179 896
$\boldsymbol{\tau_c \approx (131.7 \pm 0.1)\,\mathrm{ns}}$	

Table 6.5: Results of a time transfer calibration measurement using an SR620 time interval counter. The time delays of interest at the bottom of the table are calculated from the time interval measurements at the top of the table. The value of the calibration constant (calculated via equation 6.7) is rounded and the uncertainty is taken from table 6.1.

connected to channel B of the SR620, while channel A is triggered by the output 2 of the PPS generator. From these measurements $\Delta T_{\mathrm{In,Ref}}$, $\tau_{\mathrm{Ref}\rightarrow\mathrm{Out}}$ and $\tau_{\mathrm{Ref}\rightarrow\mathrm{Ret}}$ are calculated. Since the delay between the PPS reference output and the next timing pulse is approximately 616.8 µs and the delay of the fibre link is approximately 284 µs—which added together is larger than the time marker period of 800 µs—different time marker pulses start and stop the time interval measurement. The time marker that stops the measurement was released 800 µs before the time marker that starts the time interval measurement. This has to be accounted for in the calculation of the time delays of interest which are given by:

$$\tau_{\mathrm{Ref}\rightarrow\mathrm{Out}} = 100\,336\,462 + 800\,000\,000 - 616\,830\,299 = 283\,506\,163\,\mathrm{ps}, \quad (6.11)$$

$$\tau_{\mathrm{Ref}\rightarrow\mathrm{Ret}} = 383\,705\,419 + 800\,000\,000 - 616\,830\,299 = 566\,875\,120\,\mathrm{ps}. \quad (6.12)$$

The same principle is applied for the direct measurement of $\tau_{\mathrm{In}\rightarrow\mathrm{Out}}$. Since the link is stabilised, the forward and backward delays of the fibre are the same ($\tau_{\mathrm{Fib\_F}} = \tau_{\mathrm{Fib\_B}}$) within the uncertainty calculated in section 6.2.3,

Time interval measurements	
Signal	TI (ps)
PPS in	2 944
Ref out	616 830 299
Ret out	383 705 419
User out	100 336 462
Calculated time delays	
Delay	TI (ps)
$\Delta T_{\mathrm{In,Ref}}$	616 827 355
$\tau_{\mathrm{Ref}\to\mathrm{Out}}$	283 506 163
$\tau_{\mathrm{Ref}\to\mathrm{Ret}}$	566 875 120
$\boldsymbol{\tau_{\mathrm{In}\to\mathrm{Out}}}$ **(prediction)**	$(\mathbf{900\,333.45 \pm 0.08})$ **ns**
$\boldsymbol{\tau_{\mathrm{In}\to\mathrm{Out}}}$ **(measurement)**	$(\mathbf{900\,333.52 \pm 0.05})$ **ns**

Table 6.6: Results of a time transfer verification measurement using an SR620 time interval counter. The time delays of interest at the bottom of the table are calculated from the time interval measurements at the top of the table. For the verification of the calibration, the predicted value of the delay $\tau_{\mathrm{In}\to\mathrm{Out}}$ (right terms of equation 6.5; calculated using τ_{c} from table 6.5) is compared to the direct measurement of $\tau_{\mathrm{In}\to\mathrm{Out}}$. The uncertainty for the predicted value is taken from table 6.2 and the uncertainty of the direct measurement is the uncertainty of the SR620 for relative measurements. The values of both results have been rounded. The two measurements agree within their uncertainties.

and the delay between the local PPS reference signal and the user timing pulse is calculated as $\tau_{\mathrm{In}\to\mathrm{Out}} = \Delta T_{\mathrm{In,Ref}} + \frac{1}{2}\tau_{\mathrm{Ref}\to\mathrm{Ret}} + \frac{1}{2}\tau_{\mathrm{c}}$. This prediction is then compared to the direct measurement of $\tau_{\mathrm{In}\to\mathrm{Out}}$. As can be seen in table 6.6, the prediction and the direct measurement are in agreement within their associated uncertainties. Hence, the time transfer calibration method is successfully verified. Two verification measurements like the one presented in table 6.6 were carried out, in both measurement the predicted and the measured value for $\tau_{\mathrm{In}\to\mathrm{Out}}$ were in agreement within their associated uncertainties. The next aim was to improve the accuracy using the TDS7404B digital storage oscilloscope.

Accuracy (TDS7404B)

In order to reach an accuracy at the tens of ps level, it is first necessary to enhance the slew rate of the rf time marker pulses as well as the slew rate of the timing pulse from the PPS generator. For this purpose the 500 MHz rf amplifiers are replaced by 1500 MHz rf amplifiers (ZKL-1R5+, Mini-Circuits) which generate rf pulses with a rise time of approximately 200 ps (see figure 6.8), and a pulse generator (Model 4022, Picosecond Pulse Labs) is deployed to enhance the slew rate of both outputs of the PPS generator. The 4022 pulse generator is triggered by the 1 PPS generator and provides pulses with a rise time of approximately 10 ps [136]. In the experiment described here, the variable optical attenuators used in the previous section to match the amplitudes of the rf time marker pulses were not available. The rf amplitude of the time marker pulses could therefore only be coarsely adjusted by fixed attenuators and time interval measurements with a constant trigger level would therefore yield wrong results. This issue is overcome by measuring the amplitude of time marker pulses in every time interval measurement and measuring the delay corresponding to 50% of the amplitude.

As discussed in section 6.2.3, due to the dependence of the time accuracy of the TDS7404B on the duration of the measured time interval, it is furthermore necessary to employ a specially devised measurement technique. The time marker period is chosen to be 100 ns so that all time interval measurements are below 100 ns, corresponding to a 7 ps uncertainty of the TDS7404B. As a result, there are approximately 2840 (5680) time marker pulses on the one-way trip (round-trip) through the 50 km fibre link at any one time. The exact knowledge of the number of pulses in the fibre can be used to calculate the required delays of the fibre link even though only time intervals below 100 ns are measured. In order to calculate the number of pulses in the link, the delay is first measured with ns accuracy using a larger timing pulse interval (800 µs) and then divided by the smaller timing pulse interval (100 ns). This method can be used because the time interval between the optical pulses is kept constant by locking the repetition rate

Time interval measurements	
Signal	TI (ps)
Ref out	1 242
Ret out	73 579
User out	56 329
Calculated time delays	
Delay	TI (ps)
$\tau'_{\mathrm{Ref}\to\mathrm{Out}}$	155 087
$\tau'_{\mathrm{Ref}\to\mathrm{Ret}}$	172 337
$\boldsymbol{\tau_{\mathrm{c}} \approx (137.84 \pm 0.02)\,\mathrm{ns}}$	

Table 6.7: Results of a time transfer calibration measurement using a TDS7404B digital storage oscilloscope. In order to obtain the values of $\tau'_{\mathrm{Ref}\to\mathrm{Out}}$ and $\tau'_{\mathrm{Ref}\to\mathrm{Ret}}$, 100 ns have to be added to the measured values of Ret out and User out because the delays are larger than the period of the time marker pulses. The value of the calibration constant (calculated via equation 6.7) is rounded and the uncertainty is taken from table 6.3.

of the laser and the pulse generator to the hydrogen maser, and the delay fluctuations of the free running fibre link are small compared to the time marker period (100 ns).

Throughout all measurements the oscilloscope is triggered (channel 1) by the slew rate enhanced output 2 of the PPS generator and the averaging of the oscilloscope is set to 25 samples. At first, the time transfer set-up calibration constant τ_{c} is determined via equation 6.7. For this purpose, the signals of Ref out, Ret out and User out are sequentially connected to channel 2 of the oscilloscope via the same SMA cable and their delays with respect to the trigger signal of channel 1 are measured. In table 6.7 a calibration measurement can be seen. The calibration measurement was repeated on three different days. All three measurements ($\tau_{\mathrm{c1}} \approx (137.84 \pm 0.02)\,\mathrm{ns}$, $\tau_{\mathrm{c2}} \approx (137.84 \pm 0.02)\,\mathrm{ns}$, $\tau_{\mathrm{c2}} \approx (137.85 \pm 0.02)\,\mathrm{ns}$) were in agreement within their associated uncertainties. For the verification measurements the average of the three calibration values was used, i.e. $\tau_{\mathrm{c}} = (137.84 \pm 0.02)\,\mathrm{ns}$.

The results from a verification measurement over the 50 km fibre spool can be seen in table 6.8. In order to calculate the correct values for $\tau_{\mathrm{Ref}\to\mathrm{Out}}$

Time interval measurements	
Signal	TI (ps)
PPS in	4 534
Ref out	61 219
Ret out	70 555
User out	84 815
Calculated time delays	
Delay	TI (ps)
$\Delta T_{\mathrm{In,Ref}}$	56 685
$\tau_{\mathrm{Ref}\to\mathrm{Out}}$	283 523 596
$\tau_{\mathrm{Ref}\to\mathrm{Ret}}$	566 909 336
$\boldsymbol{\tau_{\mathrm{In}\to\mathrm{Out}}}$ **(prediction)**	$(\mathbf{283\,580.28 \pm 0.01})$ **ns**
$\boldsymbol{\tau_{\mathrm{In}\to\mathrm{Out}}}$ **(measurement)**	$(\mathbf{283\,580.281 \pm 0.007})$ **ns**

Table 6.8: Results of a time transfer verification measurement using the TDS7404B digital storage oscilloscope. The time delays of interest at the bottom of the table are calculated from the time interval measurements at the top of the table taking into account the number of pulses in the fibre link (equations 6.13–6.16). For the verification of the calibration, the predicted value of the delay $\tau_{\mathrm{In}\to\mathrm{Out}}$ (right terms of equation 6.5) is compared to the direct measurement of $\tau_{\mathrm{In}\to\mathrm{Out}}$. The value of the predicted value is rounded and the uncertainty is taken from table 6.4; the uncertainty of the direct measurement is the uncertainty of the TDS7404B for relative measurements (7 ps). The two measurements agree within their uncertainties.

and $\tau_{\mathrm{Ref}\to\mathrm{Ret}}$ from the measured time intervals, knowledge of the number of time marker pulses in the fibre link is required. For this purpose the SR620 time interval counter is used to measure the time delays of $\tau_{\mathrm{Ref}\to\mathrm{Out}}$ and $\tau_{\mathrm{Ref}\to\mathrm{Ret}}$ with an accuracy of 0.5 ns. The period of the time marker pulses is changed to 800 µs and Ref out is connected to channel A. Then User out and Ret out are sequentially connected to channel B of the TIC to yield $\tau_{\mathrm{Ref}\to\mathrm{Out}} = (283\,524.2 \pm 0.5)$ ns and $\tau_{\mathrm{Ref}\to\mathrm{Ret}} = (566\,909.4 \pm 0.5)$ ns. The number of pulses on the one-way trip N_{ow} and round-trip N_{rt} of the fibre link are then calculated as:

$$N_{\mathrm{ow}} = \frac{283\,524.2\,\mathrm{ns} + 61.219\,\mathrm{ns}}{100\,\mathrm{ns}} \approx 2835, \tag{6.13}$$

$$N_{\mathrm{rt}} = \frac{566\,909.5\,\mathrm{ns} + 61.219\,\mathrm{ns}}{100\,\mathrm{ns}} \approx 5669. \tag{6.14}$$

Those values are rounded down to the next integer. The remaining fraction of 100 ns is measured by the oscilloscope (table 6.8). The value of 61 219 ps is the delay between the output 2 of the PPS generator that triggers channel 1 of the oscilloscope and the moment when the next time marker pulse reaches Ref out at channel 2 of the oscilloscope. This value has to be added to the time intervals measured with the SR620 because in this measurements the time interval counter was triggered by the signal from Ref out rather than the output 2 of the PPS generator. Once the number of pulses in the link has been determined, the time delays $\tau_{\mathrm{Ref}\to\mathrm{Out}}$ and $\tau_{\mathrm{Ref}\to\mathrm{Out}}$ in table 6.8 can be calculated as:

$$\tau_{\mathrm{Ref}\to\mathrm{Out}} = 2835 \times 100\,\mathrm{ns} + 84\,815\,\mathrm{ps} - 61\,219\,\mathrm{ps} = 283\,523\,596\,\mathrm{ps}, \tag{6.15}$$

$$\tau_{\mathrm{Ref}\to\mathrm{Ret}} = 5669 \times 100\,\mathrm{ns} + 70\,555\,\mathrm{ps} - 61\,219\,\mathrm{ps} = 566\,909\,336\,\mathrm{ps}. \tag{6.16}$$

The same concept is applied to calculate the delay of the direct measurement of $\tau_{\mathrm{In}\to\mathrm{Out}}$. As can be seen in table 6.8, the prediction and the direct measurement of $\tau_{\mathrm{In}\to\mathrm{Out}}$ are in agreement within their associated uncertainties. A total of 12 verification measurements, like the one shown in table 6.8, have been carried out over a period of three days. In all measurements the predicted and the measured values of $\tau_{\mathrm{In}\to\mathrm{Out}}$ were in agreement. The average deviation between the prediction and the direct measurement was approximately 10 ps, the standard deviation was approximately 3 ps and the peak-to-peak deviation was 6 ps. Hence, by using the TDS7407B with a specially devised time interval measurement technique, time transfer with an accuracy of approximately 0.01 ns has been demonstrated. This is a significant improvement compared to the accuracy of 0.08 ns achieved with the SR620 and close to the state-of-the art performance by Krehlik *et al.* (accuracy of 9 ps over a 50 km fibre spool) [108].

6.2.5 Conclusions and summary

In this section, a new time transfer method based on superimposing timing information onto the optical pulse train of a mode-locked laser has been presented and experimentally verified over a 50 km long, delay-stabilised fibre spool. The time deviation of the stabilised link was 300 fs at 25 s which is at the same level as the best results over longer distances reported to date by Krehlik *et al.* [108] using amplitude modulated cw lasers (see table 5.2). The accuracy of the time transfer has been verified at the level of approximately 0.08 ns using an SR620 time interval counter and at a level of approximately 0.01 ps using a high speed digital storage oscilloscope (TDS7404B). This is close to the state-of-the-art performance by Krehlik *et al.* (accuracy of 9 ps over a 50 km fibre spool) [108].

One advantage compared to the technique by Krehlik *et al.* [108], in which the time transfer uncertainty is proportional to the fibre length, is that here the uncertainty is not expected to increase for longer fibre links due to the use of the same laser light in both directions and dispersion compensation. This method could therefore potentially yield lower uncertainties over fibre links of hundreds of km length.

In conclusion, in this chapter it has been shown for the first time that an ITU-channel-filtered frequency comb can be used for both microwave frequency transfer (section 6.1) and time transfer (section 6.2). Since the optical carrier transfer capability of optical frequency combs has also already been demonstrated (Marra *et al.* over a 7 km fibre spool [123]), this opens up the opportunity to simultaneously transfer time as well as optical and microwave frequencies using a frequency comb.

While currently National Measurements Institutes typically use three different set-ups for time, optical- and microwave frequency transfer (see chapter 5), the scheme proposed here could deliver all three transfer methods with a single, simple set-up. Furthermore, the filtering of the comb to a single ITU channel paves the way to employ this technique over long haul telecoms fibre networks. The aim of the following chapter is to implement this method on a 158 km long fibre link between NPL and Reading.

7 Comb-based time and frequency transfer over a 159 km long fibre network

In this chapter comb-based time and frequency transfer is demonstrated on a 159 km long installed fibre network. The aim is to characterise the performance levels for the time and frequency transfer technique, demonstrated in chapter 6 on a 50 km fibre spool, on a real fibre network. This is an important step towards a future implementation of this technique in a real application. New technical challenges arise due to the longer fibre link which introduces more noise and loss.

7.1 Experimental set-up

The working principle of the experimental set-up (figure 7.1) is the same as described in chapter 6. Therefore, the following discussion will only focus on aspects that are different from the previous experiment.

Fibre network

The dark fibre network used for this experiment consists of two parallel 79.6 km long fibre links between NPL and Reading. They are part of a longer dark fibre link which runs between NPL and Harwell. In order to operate in the typical configuration for testing time and frequency transfer methods, in

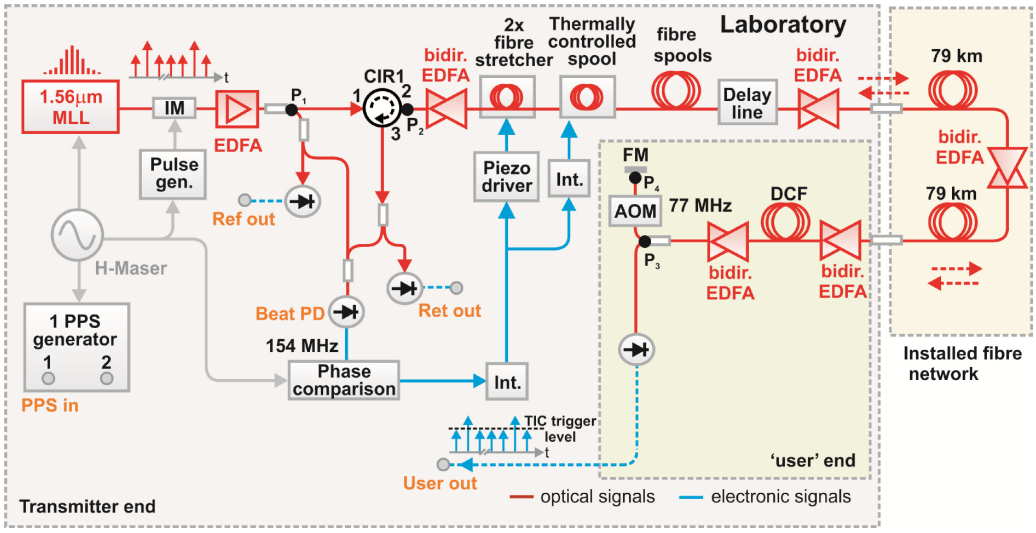

Figure 7.1: Schematic of the time and frequency transfer set-up using the NPL–Reading fibre link. Here the round-trip phase noise cancellation technique derives the error signal from an optical beat (154 MHz). Fibre-stretchers and a temperature-controlled fibre spool are used to compensate for the phase fluctuations of the fibre link. The performance of frequency transfer is characterised by measuring the phase fluctuations between the 4.4 GHz harmonic at the transmitter and user ends, and the time transfer performance is characterised by measuring the time intervals using the time marker pulses and an SR620 time interval counter. Fibre spools of the following lengths are added to the set-up in order to match the length to that compensated for by the DCF modules: 25 km, 12.5 km, 1 km and 0.4 km. PD: photodiode; IM: intensity modulator; Pulse gen.: pulse generator; Int.: integrator; EDFA: erbium-doped fibre amplifier; CIR: circulator; det.: photodetector; MLL: mode-locked laser; DCF: dispersion compensating fibre; FM: Faraday mirror; bidir.: bidirectional; PPS: pulse per second; TIC: time interval counter; AOM: acousto optical modulator.

which the user and transmitter end of the experiment are co-located in the same laboratory, the two parallel fibres are joined in Reading to form a loop. The one way link between the transmitter and user ends is approximately 159 km long and the round-trip link is 318 km long. Compared to the 50 km long fibre spool experiment in chapter 6, operation on this longer fibre link is significantly more difficult. The main challenges are to compensate for the higher loss and the larger delay fluctuations. In order to compensate for the higher loss, bidirectional EDFAs are employed, but their operation

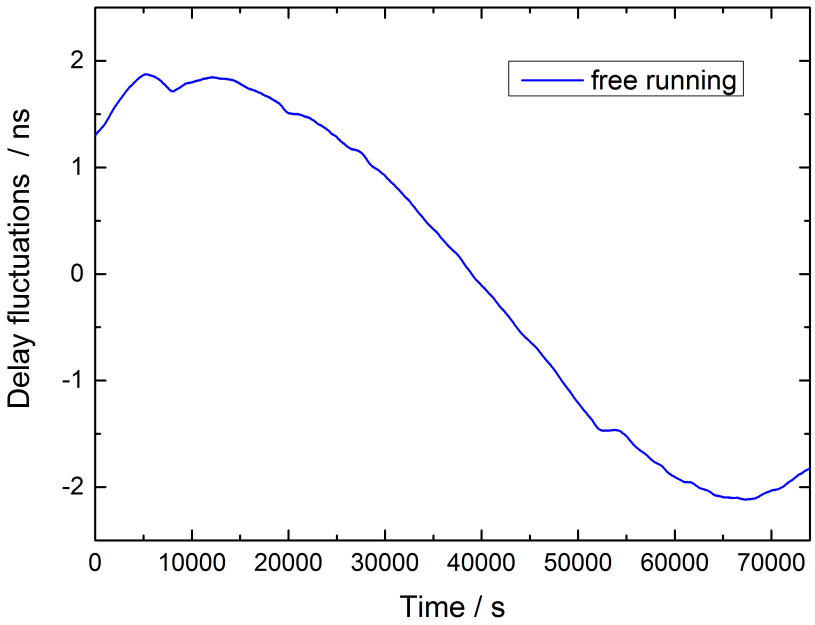

Figure 7.2: Residual delay fluctuations of the NPL–Reading fibre link when it is free-running. The measurement was obtained using an SR620 time interval counter triggered by the time marker pulses (period 800 µs) at the transmitter and user ends and averaging over 1000 samples.

is more difficult than that of unidirectional EDFAs because back-reflections can lead to lasing effects.

The temperature-induced optical path length fluctuations of the fibre link were measured to be up to around 4 ns (single pass) over the duration of 21 hours (see figure 7.2). Hence an actuator with a much larger dynamic range then the fibre stretchers is required. For this purpose an optical delay line and a temperature-controlled fibre spool were used.

Optical round-trip phase noise cancellation technique

While in the 50 km fibre spool experiment (section 6.1.1) the error signal was derived from a microwave signal, here it is derived from an optical beat signal. As described in section 5.2.3, this offers orders of magnitude higher phase sensitivity. The optical beat is generated from the optical modes of the local comb and the returned comb, which has been frequency-shifted by

154 MHz due to double-passing an AOM at the user end. As described in section 5.2.2, using an AOM has the advantage that reflections and scattered light can be distinguished from the frequency-shifted return signal. Three additional 50/50 fibre couplers and an additional photodiode (Beat PD in figure 7.1) are used in order to generate the beat signal at 154 MHz. In order to achieve temporal overlap between the two pulse trains, short fibre patch cords and an optical delay line are used. The 154 MHz beat signal is divided by a factor of 1044, and the resulting 148 kHz signal is phase compared to a signal of the same frequency (derived from a synthesiser) using a double-balanced mixer. The division is required in order to reduce the phase fluctuations to within the linear range of the mixer and avoid cycle slips. The error signal is sent to two integrators which drive two fibre stretchers (for fast feedback) and a temperature-controlled 12.5 km long fibre spool (for slow feedback) to stabilise the optical delay of the fibre link. In order to minimise delay drifts in non-common fibre components (only passed by either forward- or backward travelling light), all fibre components at the transmitter and user ends were put into separate plastic boxes filled with thermal insulation shields.

Dispersion compensation

The advantage of filtering the output of the comb for the dispersion management has already been discussed in section 6.1. Here, ITU channel 44 (centred around 1542.14 nm) is used instead of channel 43 since more channel 44 filters were available. For the dispersion management, three dispersion compensation modules are employed, one compensates for roughly 100 km of SMF-28 fibre and the other two compensate for roughly 50 km each. They have the following dispersions: 100 km DCF: $1637\,\mathrm{ps\,nm^{-1}}$, 50 km DCFs: $828\,\mathrm{ps\,nm^{-1}}$ and $824\,\mathrm{ps\,nm^{-1}}$. SMF-28 has a dispersion of approximately $16.6\,\mathrm{ps\,nm^{-1}\,km^{-1}}$ at 1542.14 nm, so the dispersion of the combined DCF modules corresponds to a SMF-28 fibre link of the following length:

$$\frac{(1637 + 828 + 824)\,\mathrm{ps\,nm^{-1}}}{16.6\,\mathrm{ps\,nm^{-1}\,km^{-1}}} = 198.1\,\mathrm{km} \tag{7.1}$$

Therefore, several fibre spools (lengths: 25 km, 12.5 km, 1 km and 0.4 km) are added to the Reading link (159.2 km) in order to match the dispersion of the DCF modules. The pulse broadening due to the dispersion mismatch is then estimated to be only a couple of ps and hence negligible compared to the case when a broad comb is employed.

Loss of the fibre link

The loss of this fibre link is significantly higher than that of the 50 km fibre spool used in the previous experiment (chapter 6) because the link is longer than the fibre spool and the loss in SMF-28 at 1550 nm is approximately $0.2\,\mathrm{dB\,km^{-1}}$. The losses of the two parallel installed 79.6 km fibre links between NPL and Reading are approximately 18 dB and 19 dB. The losses of the DCF modules are approximately 7 dB (100 km DCF) and 3.5 dB for each 50 km DCF module. The combined loss of the two fibre stretchers and the optical delay line is approximately 3.5 dB. The combined loss of the fibre spools is approximately 4 dB. Additional loss comes from three 50/50 couplers (approximately 3.5 dB each) and one ITU channel filter (approximately 0.7 dB) which are required for the coupling and decoupling of light into the NPL–Reading fibre links at NPL and in Reading. These are necessary because another group within NPL also uses the NPL–Harwell link (employing different ITU channel filters). For the decoupling of the light from the NPL-Reading link, a single ITU channel filter is used; for all other coupling and decoupling purposes 50/50 couplers are employed. Additional loss of approximately 7 dB is due to ten channel 44 filters along the link; one is placed on either side of every bidirectional EDFA in order to eliminate the spontaneous emission and avoid lasing effects. Light travelling to the user output experiences an additional 3.5 dB loss due to a 50/50 coupler at the user end. Light travelling back through the fibre experiences another 7 dB from the same coupler and approximately 18 dB loss due to the double pass of the AOM and another 3.5 dB from the 50/50 coupler before the return photodiode. The loss of the AOM is set to be relatively high by driving it with low rf power so that the input power of the return light is approx-

imately the same as the input power into the link at the transmitter end (−30 dBm).

This yields an overall loss of the one-way fibre link including all components listed above of approximately 80 dB which is significantly higher than the loss of 15 dB in the case of the 50 km fibre spool link (6.1). In order to compensate for this loss, a series of bidirectional erbium-doped fibre amplifiers is used.

Bidirectional EDFAs

Bidirectional erbium-doped fibre amplifiers only became commercially available approximately five years ago. In order to avoid unidirectional EDFAs in non-common paths of the set-up, here five bidirectional EDFAs (IDIL Fibres Optiques) are employed which produce gains of between 20 dB and 25 dB. The combined gain of the amplifiers is therefore above 100 dB which is significantly higher than the loss of the fibre link. This arrangement was selected since the input power into the first bidirectional EDFA was set to be only approximately −25 dBm by adding a fixed attenuator before the circulator. Hence the optical amplifiers along the link increase the power of the light to around 0 dBm at the output of the bidirectional EDFA at the user end. The input power was set to only −25 dBm to reduce SNR degradation due to reflections. This is not necessary for the error signal derived from the optical beat but if the 4.4 GHz harmonic is measured at the return output, reflection could degrade the performance.

The current of the amplifier in Reading was controlled via a GSM (Global System for Mobile Communications) protocol. Unfortunately, its pump diodes failed approximately one month after it was installed. This delayed the experiment by approximately two months, before the amplifier was returned from IDIL with a replaced pump diode.

Fibre stretchers

Here, only two commercial fibre stretchers (Opti-Phase) were employed (instead of four in the experiment from section 6.2) with a delay range of 100 ps.

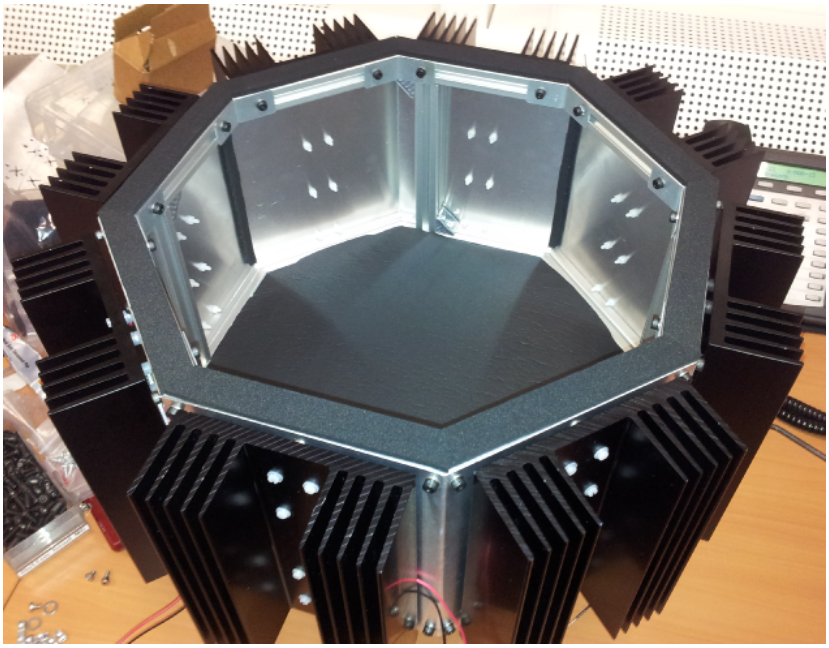

Figure 7.3: Photograph of the oven chamber used for the temperature-control of a 12.5 km fibre spool. The Peltier units at the bottom and top were not used here because the DC amplifier was not powerful enough to drive them. Insulation sheets were attached to the bottom and top of the oven chamber.

This range was sufficient since the thermally controlled fibre spool has a relatively fast response time and can compensate for delays up to 13 ns.

Temperature-controlled fibre spool

In order to compensate for the temperature-induced fibre link delay fluctuations of up to 4 ns per day and a maximum rate of change of approximately 200 ps in 30 minutes (see figure 7.2), an oven chamber for the temperature-control of a fibre spool was designed and built. The oven was designed by David Gozzard (PhD student from the University of Western Australia) during a placement at NPL. The oven can be seen in figure 7.3. It is based on an octagonal prism made out of aluminium. It has ten Peltier units (37.9 W) and ten heatsinks attached to it (eight on the sides and one on the top and one on the bottom). Here, a 12.5 km long fibre spool is placed inside the oven chamber and the eight Peltier units on the side of the oven chamber

are used for temperature-control. They are driven by a DC power amplifier based on a transistor in a push-pull configuration (built by Giuseppe Marra). The Peltier units achieve a temperature range of −3 °C to 46 °C for a room temperature of 20 °C. This performance was obtained by using a heatsink compound at the aluminium–Peltier interfaces and placing nylon washers between the aluminium sheets and the heatsinks in order to avoid bending of the aluminium sheets and therefore maximise the contact region between the heatsinks and the Peltier units. The response time of the temperature-controlled optical delay of the 12.5 km fibre spool has been investigated. Maximum heating of the Peltier units for 10 minutes resulted in an increase of the optical delay of approximately 1 ns. Maximum cooling of the Peltier units for 35 minutes resulted in a decrease of the optical delay of approximately 2 ns. The response time of the temperature-controlled spool was therefore fast enough to compensate for the delay fluctuations of the NPL–Reading link in combination with two commercial fibre stretchers. The largest measured delay change was approximately 6 ns but the full range is estimated to be around 13 ns.

Optical delay line

A manual variable optical delay line (Kylia) with a delay range of 600 ps is used to fine tune the overlap between the optical pulse trains in order to maximise the SNR of the 154 MHz optical beat signal. In the time transfer stability measurement presented in the next section (7.2.1), the delay line was also used to actively stabilise the optical delay of the fibre since the temperature spool had not yet been built. For this purpose the manual optical delay line was turned into a motorised delay line using a stepper motor and home-built electronics. In the time transfer accuracy measurement (also in section 7.2.1) and the microwave frequency transfer experiment (section 7.2.2), the delay line was just used for the fine adjustment of the pulse overlap, while the delay was stabilised using the temperature-controlled fibre spool.

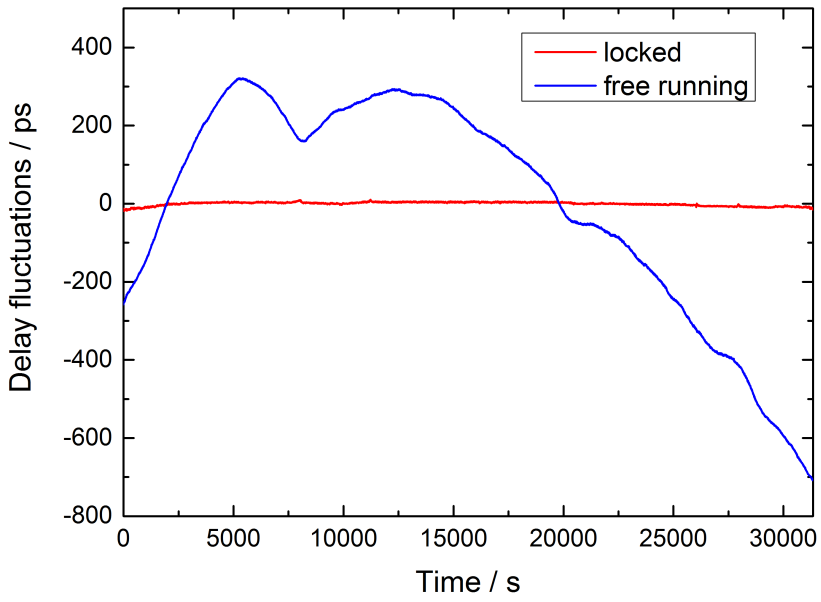

Figure 7.4: Residual delay fluctuations of the NPL–Reading fibre link when it is free-running and when it is stabilised (with feedback to two fibre stretchers and the optical delay line). The measurements were obtained using an SR620 time interval counter triggered by the time marker pulses (period 800 µs) at the transmitter and user ends and averaging over 1000 samples.

7.2 Results

7.2.1 Time transfer

Stability

The time transfer stability was measured in the same way as in the fibre spool experiment (see section 6.2.4). The residual delay fluctuations and the corresponding time deviation of the free running NPL–Reading link (blue traces) and the stabilised link (red traces) can be seen in figure 7.4 and figure 7.5 respectively. The link was stabilised using the optical round-trip phase noise cancellation technique with feedback to the two fibre stretchers and the optical delay line. The combined range of the fibre stretchers and the optical delay line of 700 ps typically enabled locking of the link for around 8 hours. In figure 7.4 the residual delay fluctuations are approxi-

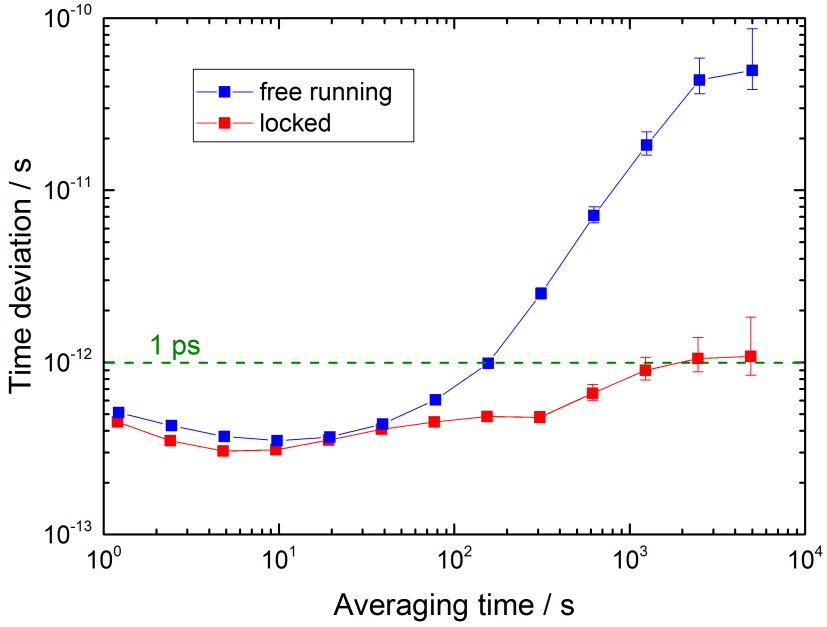

Figure 7.5: Time deviation of the NPL–Reading fibre link when it is free-running and when it is stabilised; calculated from the delay fluctuations of figure 7.4.

mately 1 ns peak-to-peak over the period of 8 hours. The magnitude of the delay fluctuations correlated with the magnitude of the temperature change outside and on many days the fluctuations were lower than those shown in figure 7.4. As can be seen in figure 7.5, the stabilisation of the fibre link results in a reduction of the time deviation by a factor of approximately 50 (at 5000 s) compared to the free running link. When the link is stabilised, the time deviation reaches a value of approximately 300 fs at 5 s. As in the 50 km spool experiment of section 6.2.4, the time deviation in the locked case is limited by the residual fluctuations of the SR620 time interval counter and stays below approximately 1 ps for all averaging times.

Accuracy

In this section the time transfer accuracy results will be presented. An SR620 time interval counter was used to measure the time intervals and the calibration and verification measurements were carried out using the same principle as in the previous experiment over the 50 km fibre spool

Time interval measurements	
Signal	TI (ps)
Ref out	163 266 631
Ret out	163 564 361
User out	163 395 623
Calculated time delays	
Delay	TI (ps)
$\tau'_{\mathrm{Ref}\to\mathrm{Out}}$	128 992
$\tau'_{\mathrm{Ref}\to\mathrm{Ret}}$	297 730
$\boldsymbol{\tau_{\mathrm{c}} = (-39.7 \pm 0.1)\,\mathrm{ns}}$	

Table 7.1: Results of a time transfer calibration measurement of the NPL–Reading set-up (with the fibre link replaced by a variable attenuator) using an SR620 time interval counter. The time delays of interest at the bottom of the table are calculated from the time interval measurements at the top of the table. The value of the calibration constant (calculated via equation 6.7) is rounded and the uncertainty is taken from table 6.1.

(see sections 6.2.2 and 6.2.4). When this experiment was carried out the digital storage oscilloscope was not available which is why the time interval counter was used instead. In the future this experiment could be repeated using the digital storage oscilloscope in order reach a higher accuracy. The uncertainty budget of the time transfer using an SR620 time interval counter was presented in section 6.2.3.

Here, a total of four calibration measurements (determination of τ_{c}) and six verification measurements (comparison between prediction and direct measurement of $\tau_{\mathrm{In}\to\mathrm{Out}}$) were carried out over the course of several days. The result from one such calibration measurement can be seen in table 7.1. The measured time intervals at the top of the table were obtained by measuring each time interval for approximately 5 minutes and subsequently calculating the average value; this is the case in the verification measurements as well. All four calibration measurements were in agreement within their uncertainty of approximately ± 0.1 ns; the average value was approximately $\tau_{\mathrm{c}} = -39.8$ ns, the standard deviation was 60 ps and the peak-to-peak deviation was 131 ps.

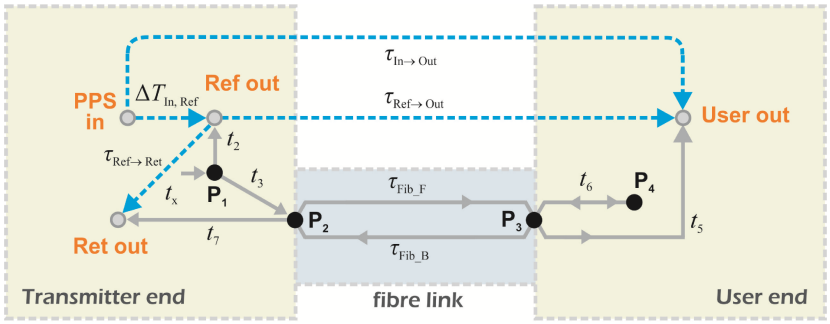

Figure 7.6: Schematic of the timing model of the NPL–Reading time transfer set-up. The concept of the time transfer is the same as described in section 6.2.2. The calibration constant is still obtained via equation 6.7, but the actual value of τ_c is different from that in table 6.10 because the non-common paths are different here. The points P_1, P_2, P_3, and P_4, which are also shown in the schematic in figure 7.1 are used to define the time delays: t_2, t_3, t_5, t_6 and t_7 (including both optical and electrical components).

In contrast to the result on the 50 km fibre spool where the average calibration constant was $\tau_c = (137.84 \pm 0.02)$ ns, here the calibration constant is negative and the absolute value is smaller. This is due to the fact that the time transfer set-up is slightly different and the lengths of the non-common paths have changed. However, the principle for obtaining τ_c remains the same (via equation 6.7). The timing model for the current set-up can be seen in figure 7.6. Here, the calibration constant contains the following non-common delays:

$$\tau_c = -t_2 + t_3 + 2t_5 - 2t_6 - t_7, \tag{7.2}$$

where the main difference to equation 6.6 in section 6.2.2 is that the delay corresponding to the unidirectional EDFA is not present and the delay $-2t_6$ is due to the double-passed AOM and fibre pigtails at the user end. The delay of the unidirectional EDFA caused the calibration factor in the fibre spool set-up to be positive and of larger magnitude.

In the verification measurements the fibre link was stabilised using the fibre stretchers and the temperature-controlled fibre spool. The time marker period was set to 800 µs. The results from one verification measurement can be seen in table 7.2. Since the one-way delay of the fibre link is approximately 1.1 ms and the time marker period is 800 µs, different time marker pulses

Time interval measurements	
Signal	TI (ps)
PPS in	4 152
Ref out	163 264 768
Ret out	788 384 111
User out	475 804 491
Calculated time delays	
Delay	TI (ps)
$\Delta T_{\mathrm{In,Ref}}$	163 260 616
$\tau_{\mathrm{Ref\to Out}}$	1 112 539 723
$\tau_{\mathrm{Ref\to Ret}}$	2 225 119 343
$\boldsymbol{\tau_{\mathrm{In\to Out}}}$ **(prediction)**	$(\mathbf{1\,275\,800.41 \pm 0.08})$ **ns**
$\boldsymbol{\tau_{\mathrm{In\to Out}}}$ **(measurement)**	$(\mathbf{1\,275\,800.34 \pm 0.05})$ **ns**

Table 7.2: Results of a time transfer verification measurement of the NPL–Reading link using an SR620 time interval counter. The time delays of interest at the bottom of the table are calculated from the time interval measurements at the top of the table. For the verification of the calibration, the predicted value of the delay $\tau_{\mathrm{In\to Out}}$ (right terms of equation 6.5) is compared to the direct measurement of $\tau_{\mathrm{In\to Out}}$. The uncertainty for the predicted value is taken from table 6.2 and the uncertainty of the direct measurement is the uncertainty of the SR620 for relative measurements. Both results have been rounded. The two measurements agree within their uncertainties.

start and stop the time interval measurement on the SR620. This has to be accounted for and the time delays of interest in table 7.2 are calculated as:

$$\tau_{\mathrm{Ref\to Out}} = (475\,804\,491 + 1 \times 800\,000\,000 - 163\,264\,768)\,\mathrm{ps} = 1\,112\,539\,723\,\mathrm{ps}, \tag{7.3}$$

$$\tau_{\mathrm{Ref\to Ret}} = (788\,384\,111 + 2 \times 800\,000\,000 - 163\,264\,768)\,\mathrm{ps} = 2\,225\,119\,343\,\mathrm{ps}. \tag{7.4}$$

In five of the six verification measurements the direct measurement and the predicted value of $\tau_{\mathrm{In\to Out}}$ were in agreement within their associated uncertainties. Only in one measurement was the difference (-144 ps) slightly larger than the combined one sigma uncertainties. The average deviation between the prediction and the direct measurement was -32 ps, the standard

deviation was 104 ps and the peak-to-peak deviation was 243 ps. Hence, the time transfer has been successfully verified on the NPL–Reading fibre link with an accuracy of approximately 0.08 ns limited by the SR620 time interval counter.

7.2.2 Microwave frequency transfer

In the microwave transfer experiment presented in this section several changes were made to the set-up shown in figure 7.1. As it is not strictly necessary to measure the stability of the microwave signal at the return output and unidirectional EDFAs have been previously employed in non-common paths of a microwave transfer experiment [122], two bidirectional EDFAs were replaced by two unidirectional EDFAs at the user end and at the return end, and the input power into the link was increased from −25 dBm to −15 dBm. This was done because the noise added by the bidirectional EDFAs was measured to be slightly higher than the noise of the unidirectional EDFAs. Furthermore one 50 km DCF module was replaced by a 25 km DCF module and the fibre spools were changed accordingly yielding a total fibre length of approximately 175 km.

In order to characterise the microwave frequency transfer, the $44th$ harmonic of the repetition rate at the transmitter end is compared to that at user end. The signals are both bandpass filtered and amplified by three rf amplifiers in order to saturate a mixer which is used for phase comparison. The output from the mixer is either sent to an FFT to measure the phase noise or recorded with a digital voltmeter in order to calculate the fractional frequency instability.

Phase noise

Phase noise measurements when the MLL described in section 6.2.1 was employed in the microwave transfer experiment produced unexpected results. In figure 7.7 the phase noise of the free running fibre link (blue trace), the stabilised fibre link when the repetition rate of the MLL is locked to the hydrogen maser (red trace) and the stabilised fibre link when the repetition

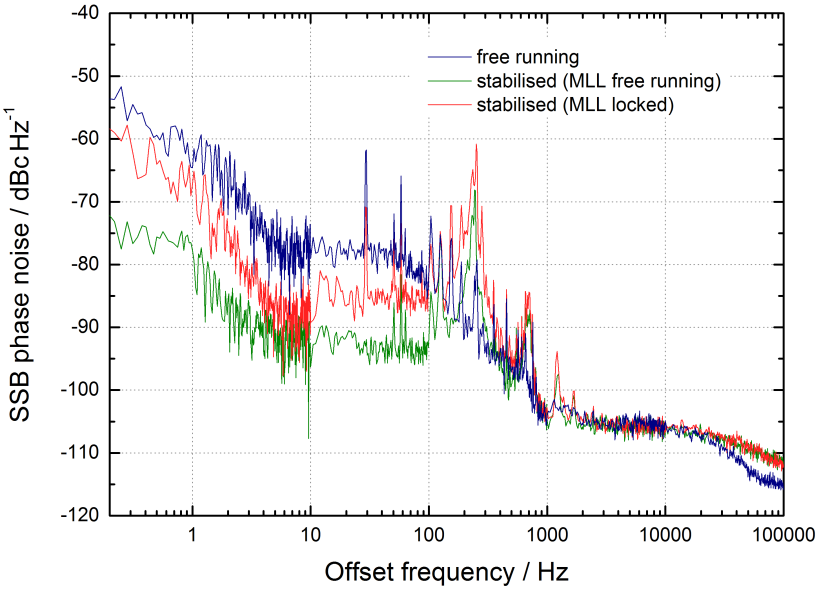

Figure 7.7: Phase noise of the microwave transfer on the NPL–Reading fibre link using a mode-locked laser. The phase noise is obtained by comparing the 4.4 GHz signal at the transmitter end with that at the user end using a double-balanced mixer. The additional noise above 100 Hz in the stabilised cases is due to self-heterodyne noise on the optical beat signal with characteristic nodes at multiples of 500 Hz (inverse of the round-trip delay). By optimising the loop filter parameters it should be possible to reduce this noise.

rate of the MLL is not stabilised (green trace) are shown. It can be seen that stabilisation of the fibre link results in a higher suppression of the phase noise of the free running link when the laser is free running (up to 20 dB) compared to the case when the laser is stabilised (up to 11 dB). In the latter case, the suppression at low offset frequencies (5 dB) is also lower than the maximum suppression, which occurs at approximately 10 Hz.

The cause of this effect is not fully understood and there was not enough time left to further investigate it as part of this thesis. One explanation could be that the repetition rate and the offset frequency in the MLL are coupled in a way that locking f_r increases the noise of f_0. However, since the offset frequency is common mode in the optical beat that produces the error signal, its noise is suppressed by approximately 20 dB per decade for offset frequencies below 500 Hz (inverse of the round-trip delay of the link)

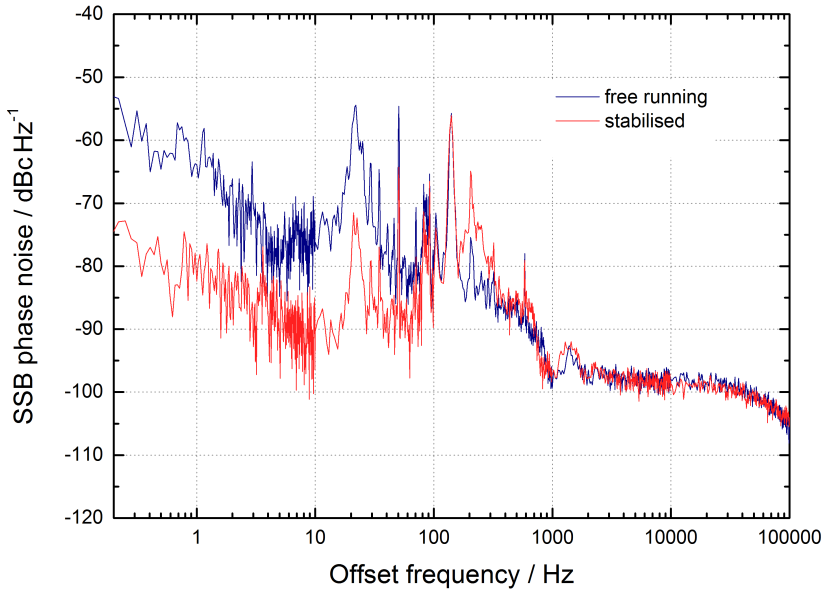

Figure 7.8: Phase noise of the microwave transfer on the NPL–Reading fibre link using a frequency comb. The phase noise is obtained by comparing the 4.4 GHz signal at the transmitter end with that at the user end using a double-balanced mixer. The frequency comb is locked in both measurements.

due to the self-heterodyne effect (see for example [137]). Therefore, the noise increase of f_0 would have to be very large in order to degrade the error signal. To gain more insight into this effect it would be useful to test whether or not it depends on the mode-locking state of the MLL.

In the next experiment the MLL was replaced by the frequency comb described in section 4.2. As can be seen in figure 7.8, in contrast to the results obtained with the MLL (figure 7.7) here the phase noise of the free running link is suppressed by up to 20 dB when the link is stabilised and the frequency comb is locked (f_r and f_0). The phase noise levels of approximately $-55\,\mathrm{dBc\,Hz^{-1}}$ at 0.2 Hz (free running) and $-75\,\mathrm{dBc\,Hz^{-1}}$ at 0.2 Hz (stabilised) are approximately the same as the corresponding phase noise levels when the free running MLL is used (from figure 7.7). Referring to the aforementioned possible explanation, this would mean that the noise of f_0 of the frequency comb is lower compared to that of the repetition-stabilised MLL which is expected since the offset frequency of the comb is stabilised.

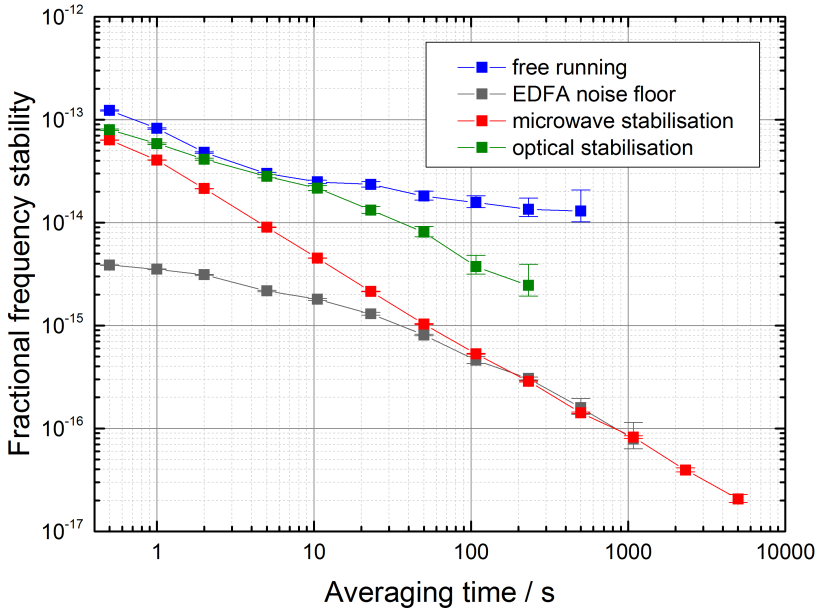

Figure 7.9: Fractional frequency instability of the microwave transfer on the NPL–Reading fibre link using a mode-locked laser. The instability is obtained by comparing the 4.4 GHz signal at the transmitter end with that at the user end using a double-balanced mixer and recording the voltage fluctuations with a digital voltmeter (measurement bandwidth of 7 Hz).

Fractional frequency instability

The fractional frequency instability of the microwave transfer was also measured using both the MLL and the frequency comb. In figure 7.9 the results obtained with the MLL (repetition rate stabilised) can be seen. When the link is stabilised using the 154 MHz optical beat signal (green trace), the fractional frequency instability is not significantly improved compared to that of the free running fibre link (blue trace) for averaging times below 10 s. At longer averaging times the fractional frequency instability is improved by a factor of approximately 6. The insufficient suppression of the free running link is attributed to the same effect that degrades the phase noise performance in figure 7.7 when the repetition rate of the MLL is locked. If the degradation is caused by an increase in the noise of f_0, one would expect to achieve a better stabilisation performance when the repetition rate is used to produce the error signal rather than the optical beat. This was tested

by locking the link using an error signal derived from the 4.4 GHz harmonic signals at the transmitter and return ends. This resulted in a fractional frequency instability of the microwave transfer of 4×10^{-14} at 1 s and 2×10^{-17} at 5000 s (red trace in figure 7.9) which is a significant improvement compared to the optical stabilisation technique. At longer averaging times the fractional frequency instability is limited by the noise contribution of the EDFAs (unidirectional and bidirectional; grey trace) which was measured by replacing the link and the fibre spools by attenuators with corresponding loss. The fractional frequency instability at longer averaging times is approximately at the same level as that of the microwave transfer reported by Marra *et al.* [122] (4×10^{-17} at 1600 s) over an 86 km long fibre link using a 30 nm wide frequency comb.

In order to achieve this performance the SNR ratio of the 4.4 GHz signal at the return end, which was initially only 26 dB, was increased to approximately 57 dB (both measured with a 1 kHz resolution bandwidth) by increasing the optical power of the returned light. This was done by increasing the rf power on the AOM by 6 dB and by increasing the current of the bidirectional EDFA in Reading from 160 mA to 220 mA. The fractional frequency instability when the SNR was 26 dB was 4×10^{-13} at 1 s, averaging down (as τ^{-1}) to 9×10^{-16} at 500 s. The increase in the SNR therefore resulted in an improvement of the fractional frequency instability by approximately one order of magnitude.

The results of the stability measurements using the optical frequency comb can be seen in figure 7.10. The performance of both locking schemes (optical and microwave) was investigated. The fractional frequency instability of the stabilised link with the microwave-based phase noise cancellation scheme (red trace in figure 7.10) gives approximately the same performance as the same technique using the MLL (red trace in figure 7.9). The averaging time of this measurement was limited to approximately 200 s because the frequency comb went out of lock. In contrast to the results obtained with the MLL (figure 7.9), here the fractional frequency instability of the optical-based stabilisation technique (green trace in figure 7.10) is 2×10^{-14} at 0.5 s which is approximately four times better than that of the microwave-based

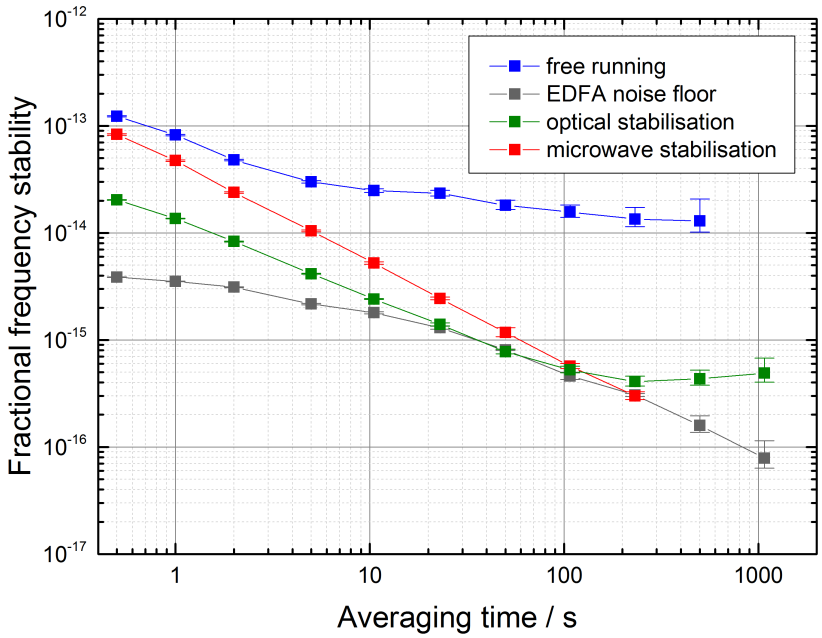

Figure 7.10: Fractional frequency instability of the microwave transfer on the NPL–Reading fibre link using a frequency comb. The instability is obtained by comparing the 4.4 GHz signal at the transmitter end with that at the user end using a double-balanced mixer and recording the voltage fluctuations with a digital voltmeter (measurement bandwidth of 7 Hz).

stabilisation technique. This improvement is expected due to the higher sensitivity offered by the optical locking technique if there is no excess noise introduced as in the case of MLL. However, at longer averaging times the stability degrades. This effect must be investigated in the future, but it might be caused by changes in the polarisation of the returned light. Such changes result in a change of the amplitude of the 154 MHz optical beat signal and subsequently introduce phase fluctuations due to AM-PM conversion in the microwave mixer. In order to mitigate this effect a polarisation scrambler could be employed.

7.3 Conclusions and summary

In this chapter the time transfer and the microwave transfer capability of an ITU-channel-filtered comb have been demonstrated over a 159 km long fibre link between NPL and Reading. The time transfer stability (approximately 300 fs at 5 s) was at a similar level as in the experiment of the 50 km fibre spool (section 6.2), limited by the residual fluctuations of the SR620 time interval counter. This is approximately at the same level as the state-of-the-art performance by Krehlik *et al.* [108, 126] using amplitude modulated cw lasers (see table 5.2). The time transfer accuracy has been been verified at a level of approximately 0.08 ns using an SR620 time interval counter. In the future, it should be investigated if, as in the previous fibre spool experiment (section 6.2), the accuracy of the time transfer can be reduced to approximately 0.01 ns by using a digital storage oscilloscope rather than a standard time interval counter.

The microwave transfer stability using the optical round-trip phase noise cancellation method and the mode-locked laser was degraded by excess noise introduced by the locking of the repetition rate. This effect might be caused by a coupling between the repetition rate and the offset frequency in the mode-locked laser, but future investigation is required in order to gain a better understanding. However, the microwave-based round-trip phase noise cancellation, which is not affected by noise of the offset frequency, produced a fractional frequency instability of approximately 2×10^{-17} at 5000 s. This is approximately at the same level as that reported by Marra *et al.* of 4×10^{-17} at 1600 s over a shorter fibre link (86 km) using a 30 nm wide optical comb.

In contrast to the MLL, there was no excess noise introduced in the locking of the optical frequency comb. The microwave-based round-trip phase noise cancellation technique using the comb produced similar results to that obtained when using the MLL. The optical-based round-trip phase noise cancellation technique reduced the fractional frequency instability to 2×10^{-14} at 0.5 s which is approximately four times better than that of the microwave-based stabilisation technique. At longer averaging times the

performance of the optical method degraded compared to the microwave method. This might be due to changes in the polarisation of the returned light which could be mitigated by using a polarisation scrambler, but future work is required in order to gain a better understanding of this effect. If it is possible to eliminate the long-term degradation of the optical round-trip phase noise cancellation technique, it would be preferable to the microwave-based technique because less averaging time would be required in order to reach the instability levels of state-of-the-art optical clocks (a few parts in 10^{18}).

In conclusion, a novel technique for simultaneous time and frequency transfer using an ITU-channel-filtered comb has successfully been demonstrated on a 158 km long fibre link. Future work will focus on the transfer stability of the optical carriers of the frequency comb. In addition, the full experiment (time transfer, microwave frequency transfer and optical frequency transfer) must be carried out simultaneously using an identical set-up.

8 Summary and conclusions

The two main research areas that have been presented in this thesis are ultra-low noise photonic microwave synthesis and fibre optic time and frequency transfer methods using optical frequency combs. In the first area, the work focussed on reducing the excess phase noise caused by amplitude-to-phase noise conversion in the optical-to-electrical conversion process, which is one of the main challenges in photonic microwave synthesis.

8.1 Low noise optical-to-electrical conversion

As described in chapter 4, balanced optical-microwave phase detectors should in principle suppress AM-PM conversion, but prior to the work carried out in this thesis the AM-PM conversion of BOM-PDs was reported to be not significantly better than that of saturated photodiodes. Two mainly free-space and two mainly fibre-based balanced optical-microwave phase detectors (BOM-PDs) were built and their optical-to-electrical conversion performance was characterised. As described in section 4.3, the phase noise of the optical-to-electrical conversion of the free-space BOM-PDs was measured to be $-119\,\mathrm{dBc\,Hz^{-1}}$ at 1 Hz and $-143\,\mathrm{dBc\,Hz^{-1}}$ at 20 kHz from an 8 GHz carrier, which is the best performance ever reported for a free-space BOM-PD. In section 4.4, two key changes to the mainly fibre BOM-PD set-up from Jung *et al.* [101] were presented. By using variable optical attenuators and a DC voltage (added to the error signal) for the fine-tuning of the balanced condition, an AM-PM conversion coefficient of 0.001 rad was obtained, which corresponds to an improvement by a factor of approximately 60–300

compared to the results from Jung *et al.* [97]. Such an AM-PM conversion coefficient corresponds to an AM-PM induced phase noise 60 dB below the relative intensity noise of a frequency comb. By using this improved BOM-PD set-up with a RIN-optimised frequency comb, this opens up a route to make the phase noise contribution of the RIN in the photonic microwave generation negligible. Despite using a commercial fibre comb with a relatively high RIN, the high AM-PM suppression demonstrated here enabled close to state-of-the-art optical-to-electrical conversion in fibre BOM-PDs with a phase noise of $-131\,\mathrm{dBc\,Hz^{-1}}$ at 1 Hz and -148 Hz at 20 kHz from an 8 GHz carrier. At low offset frequencies the performance is comparable to the best optical-to-electrical conversion reported to date (see figure 3.4) using any technique.

8.2 Comb-based time and frequency transfer via fibre links

In the area of fibre-based time and frequency transfer methods, this thesis focussed on the development of a novel time transfer technique using an ITU-channel-filtered frequency comb. As described in chapter 6, timing information is superimposed onto the optical pulse train from a mode-locked laser using an intensity modulation scheme. In section 6.2 time transfer results over a 50 km long fibre spool, which is simultaneously stabilised by the microwave-based round-trip phase noise cancellation technique (section 6.1), were presented. The time deviation of 300 fs at 25 s is at the same level as the state-of-the-art performance by Krehlik *et al.* (using amplitude modulated cw lasers) [108]. The time transfer accuracy has been verified at the level of approximately 0.08 ns using an SR620 time interval counter and at a level of approximately 0.01 ns using a high speed digital storage oscilloscope (TDS7404B). The latter is close to the state-of-the-art performance by Krehlik *et al.* (accuracy of 9 ps over a 50 km fibre spool) [108].

In contrast to earlier comb-based microwave frequency transfer experiments [130, 122], the time and microwave frequency transfer experiments

carried out in this thesis employ an ITU-channel-filtered frequency comb. This restriction of the optical bandwidth paves the way to employ this technique over long haul telecoms fibre networks. On fibre links of hundreds of km length the time transfer technique presented in this thesis could potentially yield lower uncertainties than that of Krehlik *et al.* [108] because in their method the uncertainty is proportional to the fibre length while this is not the case in the method presented here due to the use of the same laser light in both directions and dispersion compensation.

In chapter 7 the time transfer capability of an ITU-channel-filtered comb was demonstrated over a 159 km long installed fibre link between NPL and Reading. The time deviation was at a similar level as in the experiment performed on the 50 km long fibre spool (section 6.2). Using an SR620 time interval counter, the time transfer accuracy has been been verified at a level of 0.08 ns. Future work should focus on reducing the accuracy using a digital storage oscilloscope. The microwave frequency transfer capability of the ITU-channel-filtered comb over the NPL–Reading link was also investigated. As described in section 7.2.2, the frequency transfer performance using a mode-locked laser was degraded by excess noise in the locking of the repetition rate when an optical beat signal was used for the round-trip phase noise cancellation. This excess noise might be caused by a coupling between the offset frequency and the repetition rate of the mode-locked laser, but future work should investigate this effect in order to gain a better understanding. However, microwave-based round-trip phase noise cancellation produced a fractional frequency instability of 2×10^{-17} at 5000 s which is approximately at the same level as that reported by Marra *et al.* of 4×10^{-17} at 1600 s over a shorter fibre link (86 km) using a 30 nm wide optical comb. When a frequency comb was used instead of the MLL, no degradation in the microwave transfer performance was observed due to the locking of the comb. In this case, the optical round-trip phase noise stabilisation scheme produced a fractional frequency instability of 2×10^{-14} at 0.5 s which was approximately four times better than that of the microwave-based stabilisation technique. However, at longer averaging time the fractional frequency instability of the optical round-trip stabilisation technique degraded and

was worse than that of the microwave-based stabilisation. This degradation might be caused by polarisation changes of the returned light, in which case a polarisation scrambler could be employed to mitigate this problem but more investigation is required. Future work should also investigate the transfer performance of the optical carriers of the filtered frequency comb, and all three techniques, i.e. time-, microwave frequency-, and optical frequency transfer should be demonstrated at the same time using a single set-up.

The demonstration of time transfer and microwave frequency transfer using an ITU-channel-filtered frequency comb in this thesis paves the way for a novel frequency comb based transfer technique which could simultaneously transfer time, microwave frequencies and optical frequencies over long haul telecoms fibre networks. Compared to using three different transfer methods such a technique would clearly be preferable.

The time and microwave frequency transfer technique demonstrated in this thesis might be employed in the future at NPL for linking the ACES (Atomic Clock Ensemble in Space) MicroWave Link ground terminal to NPL's reference hydrogen maser using a fibre link (less than a km long). The ACES mission is due to launch in 2017 and aims to reach two-way time and frequency transfer with a time transfer accuracy of 100 ps and fractional frequency instability and inaccuracy at the 10^{-17} level [18]. The targeted performance of this ground-link at NPL is a time transfer accuracy of approximately 30 ps and a frequency transfer accuracy of 3×10^{-18}.

Bibliography

[1] A. D. Ludlow, M. M. Boyd, J. Ye, E. Peik, and P. O. Schmidt, "Optical atomic clocks", *Reviews of Modern Physics* **87**, 637–701 (2015).

[2] A. Bjerhammar, "On a relativistic geodesy", *Bulletin géodésique* **59**, 207–220 (1985).

[3] B. Bloom, T. Nicholson, J. Williams, S. Campbell, M. Bishof, X. Zhang, W. Zhang, S. Bromley, and J. Ye, "An optical lattice clock with accuracy and stability at the 10^{-18} level", *Nature* **506**, 71–75 (2014).

[4] T. Nicholson, S. Campbell, R. Hutson, G. Marti, B. Bloom, R. McNally, W. Zhang, M. Barrett, M. Safronova, and G. Strouse, "Systematic evaluation of an atomic clock at 2×10^{-18} total uncertainty", *Nature Communications* **6**, 6896 (2015).

[5] I. Ushijima, M. Takamoto, M. Das, T. Ohkubo, and H. Katori, "Cryogenic optical lattice clocks", *Nature Photonics* **9**, 185–189 (2015).

[6] C.-W. Chou, D. Hume, T. Rosenband, and D. Wineland, "Optical clocks and relativity", *Science* **329**, 1630–1633 (2010).

[7] R. M. Godun, P. B. R. Nisbet-Jones, J. M. Jones, S. A. King, L. A. M. Johnson, H. S. Margolis, K. Szymaniec, S. N. Lea, K. Bongs, and P. Gill, "Frequency ratio of two optical clock transitions in $^{171}Yb^{+}$ and constraints on the time variation of fundamental constants", *Physical Review Letters* **113**, 210801 (2014).

[8] N. Huntemann, B. Lipphardt, C. Tamm, V. Gerginov, S. Weyers, and E. Peik, "Improved limit on a temporal variation of m_p/m_e from comparisons of Yb^{+} and Cs atomic clocks", *Physical Review Letters* **113**, 210802 (2014).

[9] S. Schiller, G. Tino, P. Gill, C. Salomon, U. Sterr, E. Peik, A. Nevsky, A. Görlitz, D. Svehla, G. Ferrari, N. Poli, L. Lusanna, H. Klein, H. Margolis, P. Lemonde, P. Laurent, G. Santarelli, A. Clairon, W. Ertmer, E. Rasel, J. Müller, L. Iorio, C. Lämmerzahl, H. Dittus, E. Gill, M. Rothacher, F. Flechner, U. Schreiber, V. Flambaum, W.-T. Ni, L. Liu, X. Chen, J. Chen, K. Gao, L. Cacciapuoti, R. Holzwarth, M. Hess, and W. Schäfer, "Einstein Gravity Explorer–a medium-class fundamental physics mission", *Experimental Astronomy* **23**, 573–610 (2009).

[10] N. F. Ramsey, "A molecular beam resonance method with separated oscillating fields", *Physical Review* **78**, 695 (1950).

[11] L. Essen and J. V. L. Parry, "An atomic standard of frequency and time interval: a caesium resonator", *Nature* **176**, 280–285 (1955).

[12] T. P. Heavner, E. A. Donley, F. Levi, G. Costanzo, T. E. Parker, J. H. Shirley, N. Ashby, S. Barlow, and S. Jefferts, "First accuracy evaluation of NIST-F2", *Metrologia* **51**, 174 (2014).

[13] H. Margolis, "Timekeepers of the future", *Nature Physics* **10**, 82–83 (2014).

[14] P. Gill, "When should we change the definition of the second?", *Philosophical Transactions of the Royal Society A* **369**, 4109–4130 (2011).

[15] F. Riehle, "Towards a redefinition of the second based on optical atomic clocks", *Comptes Rendus Physique* **16**, 506–515 (2015).

[16] F. Nakagawa, J. Amagai, R. Tabuchi, Y. Takahashi, M. Nakamura, S. Tsuchiya, and S. Hama, "Carrier-phase TWSTFT experiments using the ETS-VIII satellite", *Metrologia* **50**, 200 (2013).

[17] H. Hachisu, M. Fujieda, S. Nagano, T. Gotoh, A. Nogami, T. Ido, S. Falke, N. Huntemann, C. Grebing, B. Lipphardt, C. Lisdat, and D. Piester, "Direct comparison of optical lattice clocks with an intercontinental baseline of 9000 km", *Optics Letters* **39**, 4072–4075 (2014).

[18] L. Cacciapuoti and C. Salomon, "Atomic clock ensemble in space", *Journal of Physics: Conference Series* **327**, 012049 (2011).

[19] K. Predehl, G. Grosche, S. Raupach, S. Droste, O. Terra, J. Alnis, T. Legero, T. W. Hänsch, T. Udem, R. Holzwarth, and H. Schnatz, "A 920-kilometer optical fiber link for frequency metrology at the 19th decimal place", *Science* **336**, 441–444 (2012).

[20] S. Droste, F. Ozimek, T. Udem, K. Predehl, T. W. Hänsch, H. Schnatz, G. Grosche, and R. Holzwarth, "Optical-frequency transfer over a single-span 1840 km fiber link", *Physical Review Letters* **111**, 110801 (2013).

[21] M. A. Lombardi, L. M. Nelson, A. N. Novick, and V. S. Zhang, "Time and frequency measurements using the global positioning system", *Cal Lab: International Journal of Metrology* **8**, 26–33 (2001).

[22] P. Gill, H. Margolis, A. Curtis, H. Klein, S. Lea, S. Webster, and P. Whibberley, "Optical atomic clocks for space", *Technical Supporting Document. ESTEC/Contract No. 21641/08/NL/PA.* pp. 1–145 (2008).

[23] J. R. Vig, "Quartz crystal resonators and oscillators", *US Army Communications-Electronics Command* (2001).

[24] E. Rubiola, "Short course on stable oscillators", Slides of a talk given at the Max-Planck-Institut of Quantum Optics, Theodor Hänsch group, December 2009; http://rubiola.org.

[25] D. A. Howe, D. W. Allan, and J. Barnes, "Properties of signal sources and measurement methods", in "Thirty Fifth Annual Frequency Control Symposium. 1981", pp. 669–716, IEEE (1981).

[26] D. Allan, H. Hellwig, P. Kartaschoff, J. Vanier, J. Vig, G. M. Winkler, and N. F. Yannoni, "Standard terminology for fundamental frequency and time metrology", in "Proceedings of the 42nd Annual Frequency Control Symposium", pp. 419–425, IEEE (1988).

[27] W. J. Riley, *Handbook of frequency stability analysis*, US Department of Commerce, National Institute of Standards and Technology Gaithersburg, MD (2008).

[28] E. Rubiola, *Phase noise and frequency stability in oscillators*, The Cambridge RF and microwave engineering series, Cambridge University Press (2008).

[29] C. W. Chou, D. B. Hume, J. C. J. Koelemeij, D. J. Wineland, and T. Rosenband, "Frequency comparison of two high-accuracy Al^+ optical clocks", *Physical Review Letters* **104**, 070802 (2010).

[30] Y. Y. Jiang, A. D. Ludlow, N. D. Lemke, R. W. Fox, J. A. Sherman, L. -S. Ma, and C. W. Oates, "Making optical atomic clocks more stable with 10^{-16}-level laser stabilization", *Nature Photonics* **5**, 158–161 (2011).

[31] R. W. P. Drever, J. L. Hall, F. V. Kowalski, J. Hough, G. M. Ford, A. J. Munley, and H. Ward, "Laser phase and frequency stabilization using an optical resonator", *Applied Physics B: Lasers and Optics* **31**, 97–105 (1983).

[32] D. R. Leibrandt, M. J. Thorpe, J. C. Bergquist, and T. Rosenband, "Field-test of a robust, portable, frequency-stable laser", *Optics Express* **19**, 10278–10286 (2011).

[33] S. Webster and P. Gill, "Force-insensitive optical cavity", *Optics Letters* **36**, 3572–3574 (2011).

[34] K. Numata, A. Kemery, and J. Camp, "Thermal-noise limit in the frequency stabilization of lasers with rigid cavities", *Physical Review Letters* **93**, 250602 (2004).

[35] G. D. Cole, W. Zhang, M. J. Martin, J. Ye, and M. Aspelmeyer, "Tenfold reduction of brownian noise in high-reflectivity optical coatings", *Nature Photonics* **7**, 644–650 (2013).

[36] T. Kessler, C. Hagemann, C. Grebing, T. Legero, U. Sterr, F. Riehle, M. Martin, L. Chen, and J. Ye, "A sub-40-mHz-linewidth laser based on a silicon single-crystal optical cavity", *Nature Photonics* **6**, 687–692 (2012).

[37] F. Kéfélian, H. Jiang, P. Lemonde, and G. Santarelli, "Ultralow-frequency-noise stabilization of a laser by locking to an optical fiber-delay line", *Optics Letters* **34**, 914–916 (2009).

[38] J. Dong, Y. Hu, J. Huang, M. Ye, Q. Qu, T. Li, and L. Liu, "Subhertz linewidth laser by locking to a fiber delay line", *Applied Optics* **54**, 1152–1156 (2015).

[39] M. J. Thorpe, L. Rippe, T. M. Fortier, M. S. Kirchner, and T. Rosenband, "Frequency stabilization to 6×10^{-16} via spectral-hole burning", *Nature Photonics* **5**, 688–693 (2011).

[40] J. G. Bohnet, Z. Chen, J. M. Weiner, D. Meiser, M. J. Holland, and J. K. Thompson, "A steady-state superradiant laser with less than one intracavity photon", *Nature* **484**, 78–81 (2012).

[41] J. Ye and S. T. Cundiff, *Femtosecond optical frequency comb: Principle, operation and applications*, Springer Science & Business Media (2005).

[42] J. N. Eckstein, A. I. Ferguson, and T. W. Hänsch, "High-resolution two-photon spectroscopy with picosecond light pulses", *Physical Review Letters* **40**, 847–850 (1978).

[43] D. Jones, S. Diddams, J. Ranka, A. Stentz, R. Windeler, J. Hall, and S. Cundiff, "Carrier-envelope phase control of femtosecond mode-locked lasers and direct optical frequency synthesis", *Science* **288**, 635 (2000).

[44] S. Diddams, D. Jones, J. Ye, S. Cundiff, J. Hall, J. Ranka, R. Windeler, R. Holzwarth, T. Udem, and T. W. Hänsch, "Direct link between microwave and optical frequencies with a 300 THz femtosecond laser comb", *Physical Review Letters* **84**, 5102–5105 (2000).

[45] T. W. Hänsch, "Nobel lecture: passion for precision", *Reviews of Modern Physics* **78**, 1297–1309 (2006).

[46] J. L. Hall, "Nobel lecture: Defining and measuring optical frequencies", *Reviews of Modern Physics* **78**, 1279–1295 (2006).

[47] T. Udem, R. Holzwarth, and T. W. Hänsch, "Optical frequency metrology", *Nature* **416**, 233–237 (2002).

[48] D. E. Spence, P. N. Kean, and W. Sibbett, "60-fsec pulse generation from a self-mode-locked Ti:sapphire laser", *Optics Letters* **16**, 42–44 (1991).

[49] R. Ell, U. Morgner, F. X. Kärtner, J. G. Fujimoto, E. P. Ippen, V. Scheuer, G. Angelow, T. Tschudi, M. J. Lederer, and A. Boiko, "Generation of 5-fs pulses and octave-spanning spectra directly from a Ti: sapphire laser", *Optics Letters* **26**, 373–375 (2001).

[50] R. Holzwarth, T. Udem, T. W. Hänsch, J. Knight, W. Wadsworth, and P. S. J. Russell, "Optical frequency synthesizer for precision spectroscopy", *Physical Review Letters* **85**, 2264 (2000).

[51] P. Ghelfi, F. Laghezza, F. Scotti, G. Serafino, A. Capria, S. Pinna, D. Onori, C. Porzi, M. Scaffardi, A. Malacarne, V. Vercesi, E. Lazzeri, F. Berizzi, and A. Bogoni, "A fully photonics-based coherent radar system", *Nature* **507**, 341–345 (2014).

[52] J. Capmany and D. Novak, "Microwave photonics combines two worlds", *Nature Photonics* **1**, 319–330 (2007).

[53] R. Cesarone, D. Abraham, S. Shambayati, and J. Rush, "Deep-space optical communications", in "Space Optical Systems and Applications (ICSOS), 2011 International Conference on", pp. 410–423, IEEE (2011).

[54] J.-F. Cliche and B. Shillue, "Precision timing control for radioastronomy: maintaining femtosecond synchronization in the Atacama Large Millimeter Array", *IEEE Control Systems* **26**, 19–26 (2006).

[55] J. Kim, J. Cox, J. Chen, and F. Kärtner, "Drift-free femtosecond timing synchronization of remote optical and microwave sources", *Nature Photonics* **2**, 733–736 (2008).

[56] G. Santarelli, P. Laurent, P. Lemonde, A. Clairon, A. G. Mann, S. Chang, A. N. Luiten, and C. Salomon, "Quantum projection noise in an atomic fountain: A high stability cesium frequency standard", *Physical Review Letters* **82**, 4619 (1999).

[57] J. Millo, M. Abgrall, M. Lours, E. English, H. Jiang, J. Guéna, A. Clairon, M. Tobar, S. Bize, Y. Le Coq, and G. Santarelli, "Ultralow noise microwave generation with fiber-based optical frequency comb and application to atomic fountain clock", *Applied Physics Letters* **94**, 141105 (2009).

[58] `http://www.oscilloquartz.com/files/1363164953-Br_%20OCXO%208607.pdf`, [Online; accessed 5 September 2015].

[59] J. Hartnett, D. Creedon, D. Chambon, and G. Santarelli, "Stability measurements of frequency synthesis with cryogenic sapphire oscillators", *IEEE International Frequency Control Symposium, Joint with the 22nd European Frequency and Time Forum.* pp. 372–375 (2009).

[60] `http://www.quartzlock.com/userfiles/downloads/datasheets/Active_Hydrogen_Maser_CH1-75A.pdf` (2011), [Online; accessed 5 September 2015].

[61] T. M. Fortier, M. S. Kirchner, F. Quinlan, J. Taylor, J. C. Bergquist, T. Rosenband, N. Lemke, A. Ludlow, Y. Jiang, C. W. Oates, and S. A. Diddams, "Generation of ultrastable microwaves via optical frequency division", *Nature Photonics* **5**, 425–429 (2011).

[62] A. Bartels, S. A. Diddams, C. W. Oates, G. Wilpers, J. C. Bergquist, W. H. Oskay, and L. Hollberg, "Femtosecond-laser-based synthesis of ultrastable microwave signals from optical frequency references", *Optics Letters* **30**, 667–669 (2005).

[63] F. Quinlan, T. M. Fortier, M. S. Kirchner, J. A. Taylor, M. J. Thorpe, N. Lemke, A. D. Ludlow, Y. Jiang, and S. A. Diddams, "Ultralow phase noise microwave generation with an Er:fiber-based optical frequency divider", *Optics Letters* **36**, 3260–3262 (2011).

[64] D. Nicolodi, B. Argence, W. Zhang, R. Le Targat, G. Santarelli, and Y. Le Coq, "Spectral purity transfer between optical wavelengths at the 10^{-18} level", *Nature Photonics* **8**, 219–223 (2014).

[65] S. A. Diddams, T. Udem, J. C. Bergquist, E. A. Curtis, R. E. Drullinger, L. Hollberg, W. M. Itano, W. D. Lee, C. W. Oates, K. R. Vogel, and D. J. Wineland, "An optical clock based on a single trapped $^{199}Hg^{+}$ ion", *Science* **293**, 825–828 (2001).

[66] E. N. Ivanov, S. A. Diddams, and L. Hollberg, "Analysis of noise mechanisms limiting the frequency stability of microwave signals generated with a femtosecond laser", *IEEE Journal of Selected Topics in Quantum Electronics* **9**, 1059–1065 (2003).

[67] S. A. Diddams, L. Hollberg, L.-S. Ma, and L. Robertsson, "Femtosecond-laser-based optical clockwork with instability $\leq 6.3 \times 10^{-16}$ in 1 s", *Optics Letters* **27**, 58–60 (2002).

[68] E. Ivanov, J. McFerran, S. Diddams, and L. Hollberg, "Noise properties of microwave signals synthesized with femtosecond lasers", *IEEE Transactions on Ultrasonics, Ferroelectrics and Frequency Control* **54**, 736–745 (2007).

[69] D. Hudson, K. Holman, R. Jones, S. Cundiff, J. Ye, and D. Jones, "Mode-locked fiber laser frequency-controlled with an intracavity electro-optic modulator", *Optics Letters* **30**, 2948–2950 (2005).

[70] Y. Le Coq, W. Zhang, G. Santarelli, M. Fischer, and R. Holzwarth, "Investigation of an optical frequency comb with intracavity EOM and optimization of microwave generation", in "Proceedings of the European Frequency and Time Forum (EFTF), 2012", pp. 238–241, IEEE (2012).

[71] W. C. Swann, E. Baumann, F. R. Giorgetta, and N. R. Newbury, "Microwave generation with low residual phase noise from a femtosecond fiber laser with an intracavity electro-optic modulator", *Optics Express* **19**, 24387–24395 (2011).

[72] H. Telle, B. Lipphardt, and J. Stenger, "Kerr-lens, mode-locked lasers as transfer oscillators for optical frequency measurements", *Applied Physics B: Lasers and Optics* **74**, 1–6 (2002).

[73] J. Stenger, H. Schnatz, C. Tamm, and H. R. Telle, "Ultraprecise measurement of optical frequency ratios", *Physical Review Letters* **88**, 073601 (2002).

[74] L.-S. Ma, Z. Bi, A. Bartels, L. Robertsson, M. Zucco, R. S. Windeler, G. Wilpers, C. Oates, L. Hollberg, and S. A. Diddams, "Optical frequency synthesis and comparison with uncertainty at the 10^{-19} level", *Science* **303**, 1843–1845 (2004).

[75] H. Jiang, J. Taylor, F. Quinlan, T. Fortier, and S. Diddams, "Noise floor reduction of an Er:fiber laser-based photonic microwave generator", *IEEE Photonics Journal* **3**, 1004–1012 (2011).

[76] A. Bartels, D. Heinecke, and S. A. Diddams, "10-GHz self-referenced optical frequency comb", *Science* **326**, 681–681 (2009).

[77] A. Haboucha, W. Zhang, T. Li, M. Lours, A. N. Luiten, Y. Le Coq, and G. Santarelli, "Optical-fiber pulse rate multiplier for ultralow phase-noise signal generation", *Optics Letters* **36**, 3654–3656 (2011).

[78] S. A. Diddams, M. Kirchner, T. Fortier, D. Braje, A. M. Weiner, and L. Hollberg, "Improved signal-to-noise ratio of 10 GHz microwave signals generated with a mode-filtered femtosecond laser frequency comb", *Optics Express* **17**, 3331–3340 (2009).

[79] T. M. Fortier, F. Quinlan, A. Hati, C. Nelson, J. A. Taylor, Y. Fu, J. Campbell, and S. A. Diddams, "Photonic microwave generation with high-power photodiodes", *Optics Letters* **38**, 1712–1714 (2013).

[80] F. Quinlan, T. Fortier, H. Jiang, A. Hati, C. Nelson, Y. Fu, J. Campbell, and S. Diddams, "Exploiting shot noise correlations in the photodetection of ultrashort optical pulse trains", *Nature Photonics* **7**, 290–293 (2013).

[81] Z. Li, H. Pan, H. Chen, A. Beling, and J. C. Campbell, "High-saturation-current modified uni-traveling-carrier photodiode with cliff layer", *IEEE Journal of Quantum Electronics* **46**, 626–632 (2010).

[82] E. Rouvalis, F. N. Baynes, X. Xie, K. Li, Q. Zhou, F. Quinlan, T. M. Fortier, S. A. Diddams, A. G. Steffan, A. Beling, and J. C. Campbell, "High-power and high-linearity photodetector modules for microwave photonic applications", *J. Lightwave Technol.* **32**, 3810–3816 (2014).

[83] X. Xie, Q. Zhou, K. Li, Y. Shen, Q. Li, Z. Yang, A. Beling, and J. C. Campbell, "Improved power conversion efficiency in high-performance photodiodes by flip-chip bonding on diamond", *Optica* **1**, 429–435 (2014).

[84] E. N. Ivanov, S. A. Diddams, and L. Hollberg, "Study of the excess noise associated with demodulation of ultra-short infrared pulses", *IEEE Transactions on Ultrasonics, Ferroelectrics and Frequency Control* **52**, 1068–1074 (2005).

[85] J. J. McFerran, E. N. Ivanov, A. Bartels, G. Wilpers, C. W. Oates, S. A. Diddams, and L. Hollberg, "Low-noise synthesis of microwave signals from an optical source", *Electronics Letters* **41**, 650–651 (2005).

[86] K. Wu, P. P. Shum, S. Aditya, C. Ouyang, J. H. Wong, H. Q. Lam, and K. E. K. Lee, "Characterization of the excess noise conversion from optical relative intensity noise in the photodetection of mode-locked lasers for microwave signal synthesis", *Journal of Lightwave Technology* **29**, 3622–3631 (2011).

[87] A. Bartels, S. A. Diddams, T. M. Ramond, and L. Hollberg, "Mode-locked laser pulse trains with subfemtosecond timing jitter synchronized to an optical reference oscillator", *Optics Letters* **28**, 663–665 (2003).

[88] P. Liu, K. Williams, M. Frankel, and R. Esman, "Saturation characteristics of fast photodetectors", *IEEE Transactions on Microwave Theory and Techniques* **47**, 1297–1303 (1999).

[89] W. Zhang, T. Li, M. Lours, S. Seidelin, G. Santarelli, and Y. Le Coq, "Amplitude to phase conversion of InGaAs pin photo-diodes for femtosecond lasers microwave signal generation", *Applied Physics B: Lasers and Optics* pp. 1–8 (2011).

[90] J. Taylor, S. Datta, A. Hati, C. Nelson, F. Quinlan, A. Joshi, and S. Diddams, "Characterization of power-to-phase conversion in high-speed p-i-n photodiodes", *IEEE Photonics Journal* **3**, 140–151 (2011).

[91] W. Zhang, S. Seidelin, A. Joshi, S. Datta, G. Santarelli, and Y. L. Coq, "Dual photo-detector system for low phase noise microwave generation with femtosecond lasers", *Optics Letters* **39**, 1204–1207 (2014).

[92] W. Zhang, Z. Xu, M. Lours, R. Boudot, Y. Kersalé, A. N. Luiten, Y. L. Coq, and G. Santarelli, "Advanced noise reduction techniques for ultra-low phase noise optical-to-microwave division with femtosecond fiber combs", *IEEE Transactions on Ultrasonics, Ferroelectrics, and Frequency Control* **58**, 900–908 (2011).

[93] J. Millo, R. Boudot, M. Lours, P. Y. Bourgeois, A. N. Luiten, Y. Le Coq, Y. Kersalé, and G. Santarelli, "Ultra-low-noise microwave extraction from fiber-based optical frequency comb", *Optics Letters* **34**, 3707–3709 (2009).

[94] W. Zhang, Z. Xu, M. Lours, R. Boudot, Y. Kersale, G. Santarelli, and Y. Le Coq, "Sub-100 attoseconds stability optics-to-microwave synchronization", *Applied Physics Letters* **96**, 211105–3 (2010).

[95] F. Quinlan, F. N. Baynes, T. M. Fortier, Q. Zhou, A. Cross, J. C. Campbell, and S. A. Diddams, "Optical amplification and pulse interleaving for low-noise photonic microwave generation", *Optics Letters* **39**, 1581–1584 (2014).

[96] J. Kim, F. X. Kärtner, and M. H. Perrott, "Femtosecond synchronization of radio frequency signals with optical pulse trains", *Optics Letters* **29**, 2076–2078 (2004).

[97] K. Jung and J. Kim, "Long-term stable sub-femtosecond synchronization of microwave signals with mode-locked Er-fiber lasers", in "IEEE International Frequency Control Symposium (IFCS)", pp. 1–4 (2012).

[98] M. Lessing, H. S. Margolis, C. T. A. Brown, P. Gill, and G. Marra, "Suppression of amplitude-to-phase noise conversion in balanced optical-microwave phase detectors", *Optics Express* **21**, 27057–27062 (2013).

[99] J. Kim, "High-precision optical and microwave signal synthesis and distribution", *PhD thesis, Massachusetts Institute of Technology* (2007).

[100] P. Kubina, P. Adel, F. Adler, G. Grosche, T. Hänsch, R. Holzwarth, A. Leitenstorfer, B. Lipphardt, and H. Schnatz, "Long term comparison of two fiber based frequency comb systems", *Optics Express* **13**, 904–909 (2005).

[101] K. Jung and J. Kim, "Subfemtosecond synchronization of microwave oscillators with mode-locked Er-fiber lasers", *Optics Letters* **37**, 2958–2960 (2012).

[102] T. K. Kim, Y. Song, K. Jung, C. Kim, H. Kim, C. H. Nam, and J. Kim, "Sub-100-as timing jitter optical pulse trains from mode-locked Er-fiber lasers", *Optics Letters* **36**, 4443–4445 (2011).

[103] K. Jung and J. Kim, personal communication (2013).

[104] E. Rubiola, E. Salik, N. Yu, and L. Maleki, "Flicker noise in high-speed p-i-n photodiodes", *IEEE Transactions on Microwave Theory and Techniques* **54**, 816–820 (2006).

[105] E. Ivanov, M. Tobar, and R. Woode, "Microwave interferometry: application to precision measurements and noise reduction techniques", *IEEE Transactions on Ultrasonics, Ferroelectrics, and Frequency Control* **45**, 1526–1536 (1998).

[106] D. Piester and H. Schnatz, "Novel techniques for remote time and frequency comparisons", *PTB-Mitteilungen Special Issue* **119**, 33–44 (2009).

[107] D. Piester, A. Bauch, L. Breakiron, D. Matsakis, B. Blanzano, and O. Koudelka, "Time transfer with nanosecond accuracy for the realization of International Atomic Time", *Metrologia* **45**, 185 (2008).

[108] P. Krehlik, Ł. Śliwczyński, Ł. Buczek, and M. Lipiński, "Fiber-optic joint time and frequency transfer with active stabilization of the propagation delay", *IEEE Transactions on Instrumentation and Measurement* **61**, 2844–2851 (2012).

[109] Ł. Śliwczyński, P. Krehlik, A. Czubla, Ł. Buczek, and M. Lipiński, "Dissemination of time and rf frequency via a stabilized fibre optic link over a distance of 420 km", *Metrologia* **50**, 133 (2013).

[110] S. M. Foreman, K. W. Holman, D. D. Hudson, D. J. Jones, and J. Ye, "Remote transfer of ultrastable frequency references via fiber networks", *Review of Scientific Instruments* **78**, 021101 (2007).

[111] O. Lopez, A. Kanj, P.-E. Pottie, D. Rovera, J. Achkar, C. Chardonnet, A. Amy-Klein, and G. Santarelli, "Simultaneous remote transfer of accurate timing and optical frequency over a public fiber network", *Applied Physics B* **110**, 3–6 (2013).

[112] O. Lopez, A. Amy-Klein, M. Lours, C. Chardonnet, and G. Santarelli, "High-resolution microwave frequency dissemination on an 86-km urban optical link", *Applied Physics B* **98**, 723–727 (2010).

[113] B. Wang, C. Gao, W. Chen, J. Miao, X. Zhu, Y. Bai, J. Zhang, Y. Feng, T. Li, and L. Wang, "Precise and continuous time and frequency synchronisation at the 5×10^{-19} accuracy level", *Scientific Reports* **2** (2012).

[114] H. Jiang, F. Kéfélian, S. Crane, O. Lopez, M. Lours, J. Millo, D. Holleville, P. Lemonde, C. Chardonnet, A. Amy-Klein, and G. Santarelli, "Long-distance frequency transfer over an urban fiber link using optical phase stabilization", *JOSA B* **25**, 2029–2035 (2008).

[115] P. Williams, W. Swann, and N. Newbury, "High-stability transfer of an optical frequency over long fiber-optic links", *JOSA B* **25**, 1284–1293 (2008).

[116] D. Calonico, E. Bertacco, C. Calosso, C. Clivati, G. Costanzo, M. Frittelli, A. Godone, A. Mura, N. Poli, D. Sutyrin, G. Tino, M. E. Zucco, and F. Levi, "High-accuracy coherent optical frequency transfer over a doubled 642-km fiber link", *Applied Physics B* **117**, 979–986 (2014).

[117] S. Raupach, A. Koczwara, and G. Grosche, "Optical frequency transfer via a 660 km underground fiber link using a remote brillouin amplifier", *Optics Express* **22**, 26537–26547 (2014).

[118] S. M. Raupach, A. Koczwara, and G. Grosche, "Brillouin amplification supports 1×10^{-20} accuracy in optical frequency transfer over 1400 km of underground fibre", *arXiv:1504.01567* (2015).

[119] C. Calosso, E. Bertacco, D. Calonico, C. Clivati, G. A. Costanzo, M. Frittelli, F. Levi, S. Micalizio, A. Mura, and A. Godone, "Doppler-stabilized fiber link with 6 dB noise improvement below the classical limit", *Optics Letters* **40**, 131–134 (2015).

[120] M. Musha, F.-L. Hong, K. Nakagawa, and K.-i. Ueda, "Coherent optical frequency transfer over 50-km physical distance using a 120-km-long installed telecom fiber network", *Optics Express* **16**, 16459–16466 (2008).

[121] K. W. Holman, D. D. Hudson, J. Ye, and D. J. Jones, "Remote transfer of a high-stability and ultralow-jitter timing signal", *Optics Letters* **30**, 1225–1227 (2005).

[122] G. Marra, R. Slavík, H. S. Margolis, S. N. Lea, P. Petropoulos, D. J. Richardson, and P. Gill, "High-resolution microwave frequency transfer over an 86-km-long optical fiber network using a mode-locked laser", *Optics Letters* **36**, 511–513 (2011).

[123] G. Marra, H. S. Margolis, and D. J. Richardson, "Dissemination of an optical frequency comb over fiber with 3×10^{-18} fractional accuracy", *Optics Express* **20**, 1775–1782 (2012).

[124] S. Zhang and J. Zhao, "Frequency comb-based multiple-access ultra-stable frequency dissemination with 7×10^{-17} instability", *Optics Letters* **40**, 37–40 (2015).

[125] M. Rost, D. Piester, W. Yang, T. Feldmann, T. Wübbena, and A. Bauch, "Time transfer through optical fibres over a distance of 73 km with an uncertainty below 100 ps", *Metrologia* **49**, 772 (2012).

[126] P. Krehlik, Ł. Śliwczyński, Ł. Buczek, J. Kołodziej, and M. Lipiński, "Ultrastable long-distance fibre-optic time transfer active compensation over a wide range of delays", *Metrologia* **52**, 82 (2015).

[127] T. Schibli, J. Kim, O. Kuzucu, J. Gopinath, S. Tandon, G. Petrich, L. Kolodziejski, J. Fujimoto, E. Ippen, and F. Kaertner, "Attosecond active synchronization of passively mode-locked lasers by balanced cross correlation", *Optics Letters* **28**, 947–949 (2003).

[128] F. R. Giorgetta, W. C. Swann, L. C. Sinclair, E. Baumann, I. Coddington, and N. R. Newbury, "Optical two-way time and frequency transfer over free space", *Nature Photonics* **7**, 434–438 (2013).

[129] K. Shafak, M. Xin, M. Y. Peng, and F. X. Kärtner, "Ultra-low jitter timing transfer over a multi-km fiber network with 10^{-21} relative stability", in "CLEO: Science and Innovations", pp. STh3N–1, Optical Society of America (2015).

[130] G. Marra, H. S. Margolis, S. N. Lea, and P. Gill, "High-stability microwave frequency transfer by propagation of an optical frequency comb over 50 km of optical fiber", *Optics Letters* **35**, 1025–1027 (2010).

[131] `https://www.corning.com/media/worldwide/coc/documents/Fiber/SMF-28%20Ultra.pdf` (2002), [Online; accessed 31 August 2015].

[132] `http://www.thorlabs.co.uk/thorcat/23000/DCF38-SpecSheet.pdf` (2013), [Online; accessed 22 September 2015].

[133] Y. Longqiang, L. Lin, W. Rong, J. Jisong, W. Chuanxin, Z. Yong, and Z. Baofu, "Analysis of the Sagnac effect on the accuracy of the long haul optical fiber time transfer system", in "Joint European Frequency and Time Forum & International Frequency Control Symposium (EFTF/IFCS)", pp. 303–305 (2013).

[134] `http://www.thinksrs.com/downloads/PDFs/Manuals/SR620m.pdf` (2006), [Online; accessed 22 September 2015].

[135] `http://www.tek.com/oscilloscope/tds7254-manual/tds7404-tds7254-tds7154-user-manual`, [Online; accessed 10 September 2015].

[136] `http://picosecond.surtos.com/objects/4022%20SPEC-4040089.pdf`, [Online; accessed 10 September 2015].

[137] G. Marra, *Transfer of optical frequency combs over optical fibre links*, Ph.D. thesis, University of Southampton (2013).

Appendix

Research outputs & awards

- Maurice Lessing, Helen S. Margolis, C. Tom A. Brown, and Giuseppe Marra: "Comb-based time transfer over a 159-km long fiber network", to be submitted to Optics Letters

- Maurice Lessing, Helen S. Margolis, C. Tom A. Brown, and Giuseppe Marra: "Simultaneous time and frequency transfer over a 158-km-long fiber network using a mode-locked laser", oral presentation at CLEO, abstract STh3N.2, San Jose, May 2015

- Shemar S, Gill P, Kronjaeger J, Lessing M, Marra G & Whibberley P: "Preparations for the ACES mission at the National Physical Laboratory", poster presentation at the European Frequency and Time Forum, abstract 5284, Denver, Colorado, April 2015

- Maurice Lessing, Helen S. Margolis, C. Tom A. Brown, Patrick Gill, and Giuseppe Marra: "Suppression of amplitude-to-phase noise conversion in balanced optical-microwave phase detectors", poster presentation at EMRP Satellite Workshop on "Atomic clocks for industry", June 2014, Neuchâtel

- Student Paper Competition finalist & student travel grant recipient, 28th European Frequency and Time Forum, June 23-26 2014, Neuchâtel

- Maurice Lessing, Giuseppe Marra: "Time transfer over delay-stabilized fibre links using an optical pulse train", poster presentation at the Eu-

ropean Frequency and Time Forum, abstract 7150, June 2014, Neuchâtel

- M. Lessing, H. Margolis, C. Brown, P. Gill, and G. Marra, "Suppression of amplitude-to-phase noise conversion in balanced optical-microwave phase detectors," Opt. Express 21, 27057– 27062 (2013)

- Maurice Lessing, Giuseppe Marra, Helen Margolis, Tom Brown and Patrick Gill: "An optical-microwave phase detector for generation of low-noise microwave signals from a frequency comb", oral presentation at the European Frequency and Time Forum, abstract IFCSEFTF6-H1-1, July 2013, Prague

- Maurice Lessing and Giuseppe Marra: "Develop novel techniques for accurate time transfer over fibre", Workshop on Optical Networks for Accurate Time and Frequency Transfer, 20-21 November 2012, Hoofddorp, the Netherlands

The presenting author is underlined.